Coherence properties of single self-assembled quantum dots

DISSERTATION

zur Erlangung des akademischen Grades
doctor rerum naturalium
(Dr. rer. nat.)
im Fach Physik

eingereicht an der
Mathematisch-Naturwissenschaftlichen Fakultät I
der Humboldt-Universität zu Berlin

von
Dipl.-Phys. Timur Flissikowski
geb. 13. August 1972 in Berlin

Präsident der Humboldt-Universität zu Berlin:
Prof. Dr. Mlynek

Dekan der Mathematisch-Naturwissenschaftlichen Fakultät I:
Prof. Buckhout, PhD

Gutachter:

1. Prof. Dr. F. Henneberger (HU Berlin)
2. Prof. Dr. O. Benson (HU Berlin)
3. Priv.-Doz. Dr. A. Hoffmann (TU Berlin)

eingereicht am:	14. Mai 2004
Tag der mündlichen Prüfung:	16. November 2004

Abstract

Semiconductor quantum dots (QD) have attracted considerable interest during the past years as possible candidates for quantum information processing. Due to the confinement potential in such structures, the density of states in a single QD is discrete. If the states are well separated in energy the coupling to the environment is expected to be smaller, implying that coherence is maintained during the exciton lifetime. In the present work CdSe in ZnSe QDs are used.

In this thesis, two kinds of coherence phenomena, reflecting the time evolution of such a quantum system, are studied by use of optical methods. The first phenomena is *optical coherence.* In this case, an excited state which is radiatively coupled to a ground state interacts with an external electro-magnetic field. By application of two phase locked light pulses, the optical coherence time of this state can be measured by analyzing the interference signal resulting from the subwave functions created by the first and the second excitation pulse. This experimental technique of temporal coherent control is applied via a two photon process on the biexciton state and also by a single photon process on the excited state in a single QD. As a result optical coherence times below 10 ps are found for the excited state, while for the biexciton only a lower limit on a 10 ps timescale was elaborated.

The second phenomena is *quantum coherence* and describes the phase memory between two states in the same QD. It is studied in this work by the analysis of the observed quantum beats in the time resolved photoluminescence emission (PL) of the ground state exciton in a single QD. As a result it was found that there is no measurable decoherence between the two substates of the ground state exciton during the exciton lifetime of about 300 ps.

The ground state exciton consist of two different spin states and so the decoherence time extracted from the quantum beat experiment describes a transverse spin relaxation. In contrast, in a third group of experiments the *longitudinal spin relaxation time* is investigated on a single carrier level. This kind of spin relaxation is directly connected with a transfer of occupation from one spin state to the other. The used QD sample contains charged QDs with resident electrons, which provide direct access to the separate spin dynamic of the holes. On this basis experiments in the spectral as well as in the time domain were carried out, yielding a longitudinal spin relaxation time for a single hole on a 10 ns timescale.

Keywords:
quantum dots, coherence properties, spin relaxation, II-VI semiconductor

Zusammenfassung

Halbleiter Quantenpunkte (QP) standen in den letzten Jahren im Mittelpunkt vieler Forschungsaktivitäten im Bezug auf mögliche Anwendungen im Bereich der Quanteninformationsverarbeitung. Durch das dreidimensional Confinement sind nur diskrete, energetisch stark separierte Zustände in einem QP möglich. Damit sind phasenzerstörende Streuprozesse unwahrscheinlicher und man kann Dekohärenzzeiten erwarten, die nur durch die Lebensdauer der Zustände limitiert sind. Materialbasis dieser Arbeit sind CdSe QP in einer ZnSe Barriere.

In dieser Arbeit werden zwei Arten von Kohärenzphenomänen, die das zeitliche Verhalten solcher Quantensysteme beschreiben, mittels optischer Methoden untersucht. Die eine ist die *optische Kohärenz*. In diesem Fall wechselwirkt ein angeregter Zustand, der strahlend mit einem Grundzustand verbunden ist, mit einem externen elektro-magnetischen Feld. Die optische Dephasierungszeit kann durch Anregung mit zwei optischen Impulsen, die zeitlich zueinander verzögert sind, gemessen werden. Die Auswertung des Interferenzsignals zu den Verzögerungszeiten, bei denen sich die beiden Impulse nicht mehr selbst zeitlich überlappen, liefert dann eine Aussage über das Phasengedächtnis des entsprechenden Zustandes. Diese experimentelle Technik, genannt 'phase-locked temporal coherent control', wird in der vorliegenden Arbeit im Sinne von zwei Photonen kohährenter Kontrolle auf biexzitonische Zustände sowie auf erste angeregte Zustände in einem einzelnen QP angewendet. Im Fall des angeregten Zustandes findet man optische Dephasierungszeiten unterhalb von 10 ps. Für das Biexziton kann nur eine untere Grenze bestimmt werden, die auf einer 10 ps Zeitskala liegt.

Das zweite Phenomän ist die *Quantenkohärenz*, die das Phasengedächtnis zweier Zustände im selben QP vergleicht. In dieser Arbeit wird die Quantenkohärenz durch die Analyse von Quantenschwebungen in der Emission des Grundzustandsexzitons in einem einzelnen QP untersucht. Als Ergebnis wurde gefunden, das es keine messbare Dekohärenz der beiden Unterzustände des Grundzustandsexzitons im Rahmen der strahlenden Lebensdauer von circa 300 ps gibt.

Da die beiden besagten Unterzustände zwei verschiedene Spinzustände sind, liefert das Quantenschwebungsexperiment eine Aussage über die transversale Spinrelaxationszeit. Im Gegensatz dazu beschäftigt sich die dritte Gruppe von Experimenten in dieser Arbeit mit der longitudinalen Spinrelaxationszeit einzelner Ladungsträger. Die longitudinale Spinrelaxation ist direkt verbunden mit der Umverteilung der Besetzung von dem einem in den anderen Spinzustand. Die verwendeten Quantenpunktproben enthalten auch geladene QP mit einem residenten Elektron. Diese ermöglichen den direkten Zugang zur Spindynamik einzelner Löcher. Auf dieser Basis wurden Experimente in der Spektral- als auch in der Zeitdomäne durchgeführt, die longitudinale Spinrelaxationszeiten für Löcher von knapp 10 ns lieferten.

Schlagwörter:
Quantenpunkte, Kohärenzeigenschaften, Spinrelaxation, II-VI Halbleiter

Contents

Chapter 1

Introduction

Nowadays, we are living in the information age, where the inquiry, processing and transport of information plays a key role in all levels of our community. The volume of information, e.g. voice, pictures, data ..., which is processed, transmitted, stored and retrieved is growing day by day. The connection of broad inquiry and processing of information with the possibility of wide and easy transmission of them by wireless or wire based network systems raises the need for more computing speed in order to achieve higher efficiency. But furthermore, the question of privacy and safety of the transmitted information arises.

In recent decades the demand for more computing power has always been growing. Since the introduction of the Intel 8086 microprocessor in 1978 the computational speed for a single processor has grown by about three orders of magnitude, while the typical structure size was reduced from 800 nm down to 170 nm. Following Moore's law, every 18 months microprocessors double their speed and it seems the only efficient way to make them faster is to reduce their structure size. Extrapolating this time trace to the future suggests that the physical limit for classical electronic structures will be reached soon.

For several years the scientific community has been looking for alternative concepts for computing systems that can break the limitations of the pure electronic based ones now used. One very promising concept is the use of quantum mechanics to implement computing logic. This has been strongly in the focus of several research groups since the early work of *Benioff* and later *Feynman* [1, 2] who first described in 1982 how a useful quantum computer might be constructed. Paramount for the implementation is a physical system which undergoes a unitary time evolution. This field in general promises several innovations. Quantum computation and quantum cryptography are only two of them [3]. Recently, several theoretical results have shown that quantum effects may be usable to provide qualitatively new methods of communication and computation which are in some cases more powerful and efficient than their classical counterparts [3, 4].

The qubit One main question which is in the focus of the international efforts in this field is the search for material systems which provide adequate quantum mechanical systems or so called *qubits*. The qubit is the quantum analogue to the classical *bit* in information science which carries two possible values '0' and '1'. Therefore, the qubit has to be also a two state system where the two states are called $|0\rangle$ and $|1\rangle$. There are several advantages and also demands on such a system. A very important advantage is given by the main difference between classical bit and quantum qubit. While the classical bit can be only in one of the two states 0 and 1, its quantum mechanical counterpart has the essential property of coherence and superposition. In general the state of the qubit is given by the superposition $|\Psi\rangle = \alpha|0\rangle + \beta|1\rangle$ with $|\alpha|^2 + |\beta|^2 = 1$. Measuring the qubit one will find it with a probability of $|\alpha|^2$ in the state $|0\rangle$ and with $|\beta|^2$ in the state $|1\rangle$. The important point is that $|\Psi\rangle$ describes a coherent superposition in accordance to the well defined basis $|0\rangle$ and $|1\rangle$. This means that α and β are directly correlated with each other. In principle, any two level quantum system can be used as a qubit. But for applications which are addressed to quantum mechanical properties, as e.g. it is the case in quantum computation, only such systems are interesting which show almost no decoherence or other transitions to classical behavior, so that several well defined transformation on this quantum system can be processed. Therefore, one important demand on such a system is a weak coupling to their environment.

A second demand is paramount for practical application, like gates for conditional quantum operations, that there are possibilities to network different qubits with each other in order to implement an extensive logic in quantum gates and circuits.

Systems for implementation Different physical implementations are currently in the focus of research like trapped ions and nuclear magnetic resonances (NMR). A central criterion for such a system is that the quantum mechanical states of the system are separated from the environment, so that a once created quantum state (or a superposition of two substates) remains stable in its phase relation. Semiconductors are of special interest, since in contrast to trapped ions and NMR, they can be easily implemented with currently well developed technologies into state of the art information processing systems.

Unfortunately, in a bulk semiconductor, the scattering for free carriers (quasi particles) is very efficient due to the continuous energy spectrum. This coupling to external degrees of freedom destroys the unitary time evolution of the quantum system, giving rise to decoherence times on the fs-time scale.

One possible solution is the use of semiconductor nanostructures. Such structures consist of semiconductor materials with different energy gaps, so that the semiconductor with the larger gap V_O is surrounding the one with the smaller gap V_I. If the shape of the potential localizes the electron and the hole in the same region a type I quantum structure is formed. The extension of the inner part should be so small that quantization effects become important, and so for both carriers only specific energy levels are available.

Depending on the dimensionality of the confinement potential the density of states (DOS) for the carriers changes from a continues distribution (in 3D) to

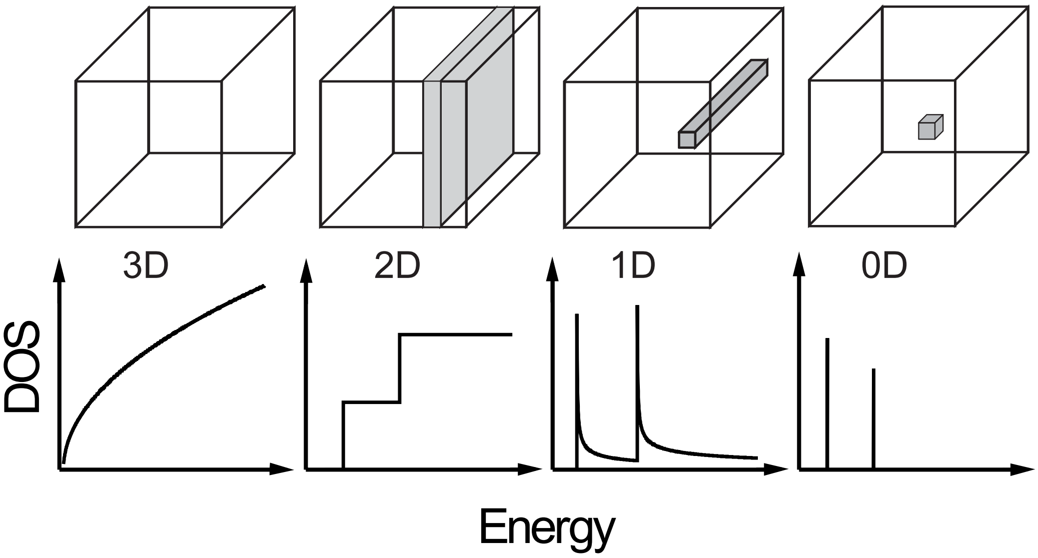

Figure 1.1: Scheme of the density of states of the conduction band for bulk (3D), quantum well (2D), quantum wire (1D), and quantum dot (0D).

well separated single states in a quantum dot (in 0D) indicated in figure 1.1. Due to the atomic like energy structure of an ideal and isolated semiconductor quantum dot (QD), scattering processes should be less probable. This implies that coherence is maintained during a longer lifetime. Due to this reason, a lot of attention has been attracted during past years by self-assembled semiconductor QDs as possible candidates for quantum information processing [5].

Optical manifestation of coherence in quantum systems Optical manipulation of the quantum mechanical system is very attractive for practical applications. Furthermore, also the time evolution of the quantum system can be studied using time resolved optical methods.

In general, one can optically study two different types of coherence phenomena, which reflect the time evolution of a quantum system. One is the *optical coherence* between a specific exciton state and the crystal ground state, where this exciton state is coupled to the phase of an external electromagnetic field. Here the coherence is measured on an external timescale, e.g. the delay time between two excitation pulses applied to the state under observation. The second one is more internal, between two excited states with a small energy separation in between, which is called *quantum coherence*. Quantum coherence compares the phase memory of two states with each other and can be different from optical coherence if there are dephasing processes which are acting with the same phase change on both states. While the optical coherence can be investigated by nonlinear experiments like four wave mixing [6, 7, 8], photon echo [9], pump-induced reflectivity change [10] and also by coherently controlling the photoluminescence (PL) emission, the quantum coherence can be observed through quantum beats in PL or polarization transients [11, 7, 12, 13].

Recent achievements in coherence in quantum structures In what follows, a short overview about experiments and results is given which are due to coherence properties of quantum structures. In recent years several different types of quantum structures have been investigated. Most of the work has been done on bulk semiconductors and quantum wells, but also zero dimensional structures like chemically synthesized nanocrystals and self-assembled QDs are under investigation. In the following paragraphs a review of papers in correspondence to the main experiments presented later in this work will be discussed. Of special interest are results based on zero dimensional structures, as far as available.

One manifestation of **quantum coherence** is given by the interference between the two non-degenerated excitonic quantum states and the corresponding oscillation in the PL emission, known as quantum beats.

The separation between the two states can be given by Zeeman splitting in an external magnetic field. Such quantum beats in the PL emission of free excitons in semiconductors were first observed by *V. Langer et al.* [11] in crystalline AgBr. Coherent excitation of the two substates leads to quantum beats in the resonant fluorescence. From the beats the authors extracted a quantum dephasing time of 400 ps. *Bar-Ad et al.* [13] also observed quantum beats in the absorption of excitons in GaAs/GaAlAs quantum wells in external magnetic fields. In a standard pump-probe experiment the evolution of the time-resolved absorption uncovers a beating between the two excitonic spin states with a damping time constant of the oscillation of about 20 ps.

Magnetic field is only one solution to get two states different in energy. The group of *Göbel et al.* [7] was the first which observed quantum beats in the coherent polarization of intrinsic excitonic states in quantum wells using the two pulse self-diffracted transient-grating technique [12]. The GaAs/GaAlAs quantum wells contain excitonic states in different islands interacting with each other, resulting in a V-type system and leading to the observed quantum beats with a decay in the ps-range. *Bonadeo et al.* observed a beating in the time integrated coherent control signal between two excited states in elliptical disk like QDs. No damping of the oscillation was observed during the excited state lifetime of 40 ps [14].

If the two states correspond to different spin states, then quantum coherence is equivalent to spin coherence, which is described by the transverse spin relaxation time. The phase between the two spin states can be monitored by analyzing the polarization of the emission. For this method the two states under observation can also be degenerated.

Paillard et al. [15] studied an ensemble of self-organized InAs/GaAs QDs while *Scheibner et al.* [16] used an ensemble of self-organized CdSe/ZnSe QDs, both under strictly resonant excitation. In both cases polarization and time-resolved PL measurements were performed. As a result for zero magnetic field, the authors found a strictly constant polarization during the exciton emission of about 2.5 ns (Paillard) and 500 ps (Scheibner) at low temperatures. This implies that no transverse spin relaxation takes place during the exciton lifetime.

Since spin states are easy to manipulate by choosing a proper polarization of the excitation they are also interesting objects for storing information. This can be done directly by the occupation of a state if phase is not important for further processing. For practical applications a sufficient long **spin memory** is important, defined by the longitudinal spin relaxation time, which describes the change of the occupation between two spin states. This time is also the upper limit for spin coherence and is widely studied.

The group of *Awschalom et al.* [17] used the time-resolved Faraday rotation technique to study both transverse and longitudinal spin relaxation in chemically synthesized CdSe nanocrystals. For the longitudinal spin relaxation they found several distinct timescales from 100 ps to 10 μs for the different crystals. The transverse spin lifetime is dominated by inhomogeneous dephasing and was not accessible.

For a single carrier in QDs only results for electrons are available. *Cortez et al.* [18] deduced from ensemble data on n-doped InAs/GaAs QDs an electron-spin memory time of 15 ns. For holes due to the extensive valence band substructure, which raises the possibilities for various scattering processes the spin memory times should be in general faster [19, 20]. In connection with this work, experimental data for single holes in QDs become available for the first time.

Since the **optical dephasing time** of a quantum system can be measured in different ways, the experimental results of several groups are important in order to classify the results of this thesis. The technique of time-integrated and time-resolved four wave mixing (TI- and TR-FWM) has been used for nearly 20 years to reveal coherence properties of excitations in semiconductors. In a series of experiments by *Schultheis et al.* using two beam degenerated FWM the dephasing time of excitons in bulk GaAs [21, 22] and GaAs quantum wells [23, 8, 24] was investigated. They found that in both cases the exciton dephasing time was in the picosecond range for a low excitation density at low temperatures. Later *Steel* and coworkers found in a series of experiments in the time domain on localized excitons in samples with GaAs/AlGaAs quantum wells dephasing times of 68 ps longer than times on free excitons [25, 26]. Finally, resent results of *Woggon et al.* [27] and *Birkedal et al.* [28] on an ensemble of strongly confined InGaAs QDs uncover by use of TR-FWM ultra long dephasing times of several hundreds of picoseconds for excitons at low temperatures, which is close to the radiative lifetime limit.

A second powerful concept to measure optical dephasing times is temporal coherent control. Here two optical pulses - well separated in time - interact with the quantum system. This method developed mostly at the beginning of the eighties in the last century in order to measure dephasing in atoms or control photo-chemical reactions in molecules [29, 30, 31, 32, 33], will be introduced in detail in section 3.2.3. Here so far only some recent results will be discussed, making expectations clearer and the interpretation of results in this work easier.

After temporal coherent control technique had entered the sector of semiconductor quantum structures at the beginning of the nineties to control THz transients emitted from GaAs quantum wells [34, 35] it was used first by *Heberle* and *Baumberg* to control the population of excitonic states in GaAs quantum wells. Since the end of the nineties, several groups have used this concept on a single quantum dot level. Such experiments are based on optical manipulation of 'hot', i.e. excited, excitonic states with short dephasing times, while the intensity of the corresponding exciton ground state is used as a monitor for the controlled excited state population. *Bonadeo et al.* [14] probed the excited state of an exciton in a QD naturally formed by width fluctuations in a GaAs QW, using an aluminium aperture to select a single dot. They found dephasing times of 40 ps [14]. The group of *Arakawa* carried out coherent excitation spectroscopy based on a low temperature near-field scanning optical microscope (NSOM) to select a single self-assembled InGaAs QD [36]. They found a dephasing time of 15 ps for the excited state. Very recently, *Besombes et al.* compared dephasing times for charged and uncharged single InGaAs QD measured by coherent control. They found that the times for the charged QD are longer (13 ps) than for the uncharged one (3 ps) [37]. So the optical dephasing time for excited states on a single QD level has been well examined.

If a single exciton state is used to implement a qubit, it is necessary to exploit a few exciton effects in order to construct more complex and conditional logic in form of the above discussed quantum gates [38, 39]. In general the biexciton in a single quantum dot represents two entangled qubits [40]. By this reason such biexcitonic states become interesting objects for experiments like coherent control, also addressed in this work.

This Thesis The present thesis is devoted to coherence properties on self-assembled CdSe QDs. The aim is to give information about the typical timescales for different kinds of coherence for carrier complexes and spin memory of single carriers in single QDs. After this introduction the work is organized as follows:

In the **second chapter** theoretical foundations will be presented. As discussed below, the used quantum dot structures contain different kinds of QDs. In the first part of this chapter the properties of these different dots will be discussed theoretically in order to extract possible, easy-to-handle characterization experiments to uncover the kind of QD optically. In this context symmetry properties as well as the influence of an external magnetic field will be discussed. The second part deals with a classification of the different manifestations of coherence and in addition spin relaxation ('transverse' and 'longitudinal') in order to clarify the terminology for the discussion in the following chapters.

The **third chapter** is devoted to the experimental objects and methods used in this work. In the first part the used CdSe/ZnSe QD sample structure is introduced including some structural information which was acquired outside of this work. The spatial QD density is rather high. Therefore, it is justified that special methods for high spatial resolution are necessary in order to carry out single dot spectroscopy experiments. These methods will be discussed in detail. After introducing the micro-optical setup, taking special care on polarization control, two different laser arrangements, both able to generate tunable ps pulses, will be described, followed by the discussion of the used time resolved photoluminescence (PL) detection scheme. For the temporal coherent control experiments on single QDs an actively stabilized Michelson interferometer is indispensable and is addressed then. Finally, the setup for experiments in external magnetic fields will be discussed.

In the **fourth chapter** a careful characterization of charged and neutral QDs with standard spectroscopic methods is done. The aim here is to make a clear distinction between both kinds of QDs and their excitonic complexes possible, paramount for the further experiments.

Then the different main experiments of this work will be discussed in the **fifth chapter**. Starting with the discussion of quantum coherence by the observation of quantum beats between the doublet of the ground state exciton. This gives information about the transverse spin relaxation time for the exciton. This is followed by the two experiments dealing with the longitudinal spin relaxation time of a single hole in a charged QD. Finally different coherent control experiments will be considered giving information about the optical coherence of different quantum mechanical states in uncharged quantum dots. Here single photon transitions as well as two photon transitions will be discussed.

Chapter 2

Fundamental optical properties of QDs

The quantum dot samples used during this work contain QDs with different in-plane anisotropy and in addition they can be neutral or charged with a resident electron (see section 3.1).

As will be discussed in section 3.1 the in-plane extension of the dot ($x-y$ plane) is typically larger than the height of the QD (z direction). This is symbolized by the disk like shape in figure 2.1 (a). The z direction corresponds to the main quantization axis which is for most of the experiments the observation axis.

In a neutral QD an external electro-magnetic wave excites an electron-hole pair (exciton). In a charged QD the additional resident electron forms together with the electron-hole pair a three particle complex (trion) with different properties than the exciton.

Since the main part of this thesis deals with coherent properties and spin memory of different states in excitons and trions, it is paramount to know how these different states are defined and which basic properties (e.g. polarization of the emission, fine structure ...) can be derived from this definition.

In what follows, some of these fundamental optical properties of excitons in uncharged QDs and trions in charged QDs, which are basic for the later discussion and the identification of the kind of QD, are summarized. In a second part, common expressions about different manifestations of coherence in nanostructures will be discussed. Theoretical foundations of experiments dealing with coherence or spin memory in a single QD will be considered and terms in this field will be clarified.

2.1 Excitons in isotropic and anisotropic, uncharged QDs

The exciton is a two particle complex which is formed by one hole and one electron which are bound together by their mutual Coulomb interaction and travelling

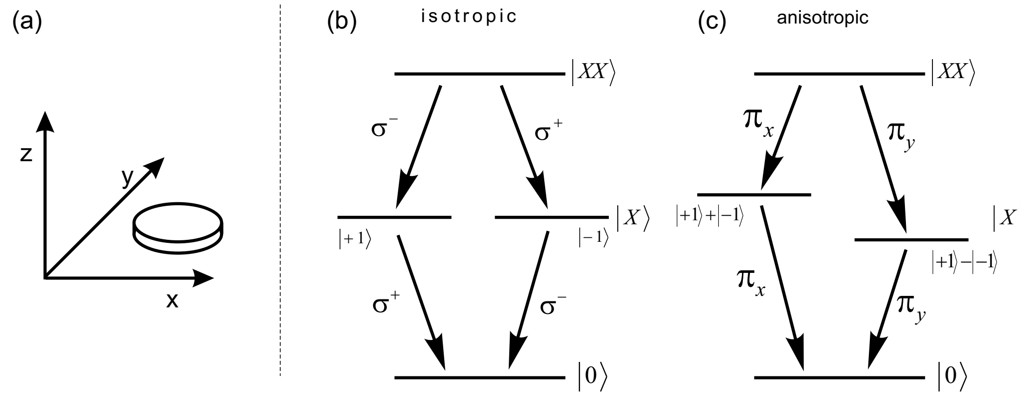

Figure 2.1: Definition of the coordination system (a). Scheme of the energy structure of an exciton and bi-exciton in an isotropic (b) and an anisotropic (c) QD.

through the bulk semiconductor (3D dimensional case). Like a hydrogen atom this complex has different energy levels. These levels scale like $E_{\mathrm{n}}^{\mathrm{3D}} = E_{\mathrm{g}} - E_0^{\mathrm{3D}}/n^2$, where E_0^{3D} is the three dimensional Rydberg energy of the exciton and E_{g} the band gap energy of the semiconductor. In analogy to the hydrogen atom the extension of the exciton can be described by the exciton Bohr radius.

As already partly discussed in the introduction, the situation changes if the electron-hole pair is confined in a potential of lower dimensionality. In this case, both of the carriers need additionally to fulfill the Schrödinger equation in respect to the confinement potential:

$$\mathcal{H}_\nu \Psi(\mathbf{r}_\nu) = \left\{ \frac{\hbar^2}{2m_{\nu,\iota}} \nabla^2 + V_{\nu,\iota} \right\} \Psi(\mathbf{r}_\nu) = E_\nu \Psi(\mathbf{r}_\nu) \tag{2.1}$$

where $\nu = \{e, h\}$ distinguishes between electron and hole, $\iota = \{i, o\}$ selects between inside and outside the quantum structure, $m_{\nu,\iota}$ is the effective mass for the respective carrier inside or outside the quantum structure, and $V_{\nu,\iota}$ is the confinement potential created by the quantum structure. From the solution of equation 2.1 it follows that both carriers can have only a number of discrete energies $E_{\nu,\mathrm{n}} < V_{\nu,o}$ if they are confined in the structure. The value and number of the energies $E_{\nu,\mathrm{n}}$ is strongly dependent on $V_{\nu,\iota}$ in its extension and dimension. For the here discussed Stranski-Krastanov QDs the confinement in z-direction (see figure 2.1 (a)) is the strongest since the extension in z-direction is smaller than in the $x - y$ plane. The z-axis is the main quantization axis. The extension of the potential, i.e. the QD, is of the order of the exciton Bohr radius. In this case, the eigenenergies of the confinement hamiltonians for the electron and for the hole $\mathcal{H}_{\mathrm{e}}$ and $\mathcal{H}_{\mathrm{h}}$ are larger than the exciton binding energy given by the Coulomb interaction. The relative coordinate between electron and hole is mostly given by the confinement. This situation is usually called 'strong confinement' approximation. The total hamiltonian for an electron-hole pair in a quantum structure can be written as:

$$\mathcal{H} = \mathcal{H}_{\mathrm{e}} + \mathcal{H}_{\mathrm{h}} + \mathcal{H}_{\mathrm{coulomb}} + \mathcal{H}_{\mathrm{e-h}} + \mathcal{H}_{\mathrm{Zeeman}} \tag{2.2}$$

In the strong confinement the main contribution of $\mathcal{H}$ arises from the confinement parts $\mathcal{H}_{\mathrm{e}}$ and $\mathcal{H}_{\mathrm{h}}$. The confinement contribution for electron and hole can be calculated independently from each other and separate from the other terms, which can be treated as a perturbation. The other terms are the direct Coulomb interaction $\mathcal{H}_{\mathrm{coulomb}}$, the electron-hole exchange interaction $\mathcal{H}_{\mathrm{e-h}}$, and the Zeeman interaction $\mathcal{H}_{\mathrm{Zeeman}}$ if an external[1] magnetic field is present.

The two contributions $\mathcal{H}_{\mathrm{e-h}}$ and $\mathcal{H}_{\mathrm{Zeeman}}$ in the total hamiltonian 2.2 are sensitive to the different combinations of the single particle spins and lead to a fine structure splitting of the originally degenerated energy levels given by the confinement and Coulomb parts of the hamiltonian 2.2. The dependence of the electron-hole exchange interaction, which couples the spins of the electron and the hole from the symmetry of the confinement potential will be discussed in more detail after the possible spin configurations of the exciton are introduced.

Due to the complex valence band structure it is necessary to distinguish between light (lh) and heavy holes (hh) with an angular momentum projection of $J_{\mathrm{lh,z}} = \pm 1/2$ and $J_{\mathrm{hh,z}} = \pm 3/2$ respectively (the main quantization axis z is also the observation axis). The confinement leads to an energy separation between the heavy and light hole state, where the lowest energy state is given by the heavy hole state. Together with the electron where the spin projection is $S_{\mathrm{e,z}} = \pm 1/2$ one can build up heavy hole excitons with a total angular momentum projection $M = S_{\mathrm{e,z}} + J_{\mathrm{hh,z}}$, of always integer spin. The excitons with $M = \pm 1$ are optically active since they can couple to the light field, while the optical inactive ones with $M = \pm 2$ can not.

The electron-hole exchange energy is given in its general form by the integral:

$$E_{\mathrm{eh}} \propto \int\int d^3r_1 d^3r_2 \; \Psi_{\mathrm{X}}^{*}\left(\mathbf{r}_{\mathrm{e}} = \mathbf{r}_1, \mathbf{r}_{\mathrm{h}} = \mathbf{r}_2\right) \cdot \frac{1}{|\mathbf{r}_1 - \mathbf{r}_2|} \cdot \Psi_{\mathrm{X}}\left(\mathbf{r}_{\mathrm{e}} = \mathbf{r}_2, \mathbf{r}_{\mathrm{h}} = \mathbf{r}_1\right) \tag{2.3}$$

where $\Psi_{\mathrm{X}}\left(\mathbf{r}_{\mathrm{e}}, \mathbf{r}_{\mathrm{h}}\right)$ is the exciton wave function and $\mathbf{r}_{\mathrm{e}}, \mathbf{r}_{\mathrm{h}}$ are the electron and hole coordinates.

Since the hh- and lh-states are split in energy by several tens of meV, the light hole excitons will be neglected for the moment. The electron-hole exchange hamiltonian can be written in matrix form in accordance to the basis of the bright and dark states of $(|+1\rangle, |-1\rangle, |+2\rangle, |-2\rangle)$ and reads as: [41]:

$$H_{\mathrm{eh}} = \frac{1}{2}\begin{pmatrix} +\Delta_0 & +\Delta_1 & 0 & 0 \\ +\Delta_1 & +\Delta_0 & 0 & 0 \\ 0 & 0 & -\Delta_0 & +\Delta_2 \\ 0 & 0 & +\Delta_2 & -\Delta_0 \end{pmatrix} \tag{2.4}$$

---

[1] Also an internal magnetic field causes Zeeman splitting, but the samples used in this work do not contain magnetic elements.

$D_{2\mathrm{d}}$			$< D_{2\mathrm{d}}$	
Eigenenergy	Eigenfunction		Eigenenergy	Eigenfunction
$+\frac{1}{2}\Delta_0$	$\|-1\rangle$		$\frac{1}{2}\Delta_0+\frac{1}{2}\Delta_1$	$\frac{1}{\sqrt{2}}(\|+1\rangle+\|-1\rangle)$
$+\frac{1}{2}\Delta_0$	$\|+1\rangle$		$\frac{1}{2}\Delta_0-\frac{1}{2}\Delta_1$	$\frac{1}{\sqrt{2}}(\|+1\rangle-\|-1\rangle)$
$-\frac{1}{2}\Delta_0+\frac{1}{2}\Delta_2$	$\frac{1}{\sqrt{2}}(\|+2\rangle+\|-2\rangle)$		$-\frac{1}{2}\Delta_0+\frac{1}{2}\Delta_2$	$\frac{1}{\sqrt{2}}(\|+2\rangle+\|-2\rangle)$
$-\frac{1}{2}\Delta_0-\frac{1}{2}\Delta_2$	$\frac{1}{\sqrt{2}}(\|+2\rangle-\|-2\rangle)$		$-\frac{1}{2}\Delta_0-\frac{1}{2}\Delta_2$	$\frac{1}{\sqrt{2}}(\|+2\rangle-\|-2\rangle)$

Table 2.1: Eigenfunctions and eigenenergies of the e-h-exchange interaction hamiltonian 2.4 for $D_{2\mathrm{d}}$ and below $D_{2\mathrm{d}}$ symmetry

The constant Δ_0 is equal to the energy separation between the two doublets arising from the bright and dark states, respectively. The constants Δ_1 and Δ_2 are the separation of the two components inside the bright and the dark doublet.

As is reported in the literature [42, 43, 44] and as will be later shown by measurements on samples which are used in this work, the symmetry of the QDs differs from dot to dot and can be close to isotropic (i.e. of symmetry belonging to the $D_{2\mathrm{d}}$ point group) or measurable anisotropic (below $D_{2\mathrm{d}}$, e.g. $C_{2\mathrm{v}}$ or C_2). This has a qualitative influence on the eigenvalues and eigenfunctions of the hamiltonian 2.4 which are plotted in table 2.1. For an isotropic QD it is $\Delta_1 = 0$. The bright exciton states are degenerated with the wave functions $|+1\rangle$ and $|-1\rangle$. As it is sketched in figure 2.1, the transitions $|+1\rangle \rightarrow |0\rangle$ and $|-1\rangle \rightarrow |0\rangle$ are σ^+ and σ^- polarized. In a QD with in-plane anisotropy Δ_1 is non zero. Consequently, the hamiltonian 2.4 needs to be diagonalized, which leads to more complex eigenfunctions which are given in table 2.1. In case of the bright exciton the antisymmetric eigenfunctions lead to linear polarized transitions like $|X\rangle = \frac{1}{\sqrt{2}}(|+1\rangle + |-1\rangle) \rightarrow |0\rangle$ and $|Y\rangle = \frac{1}{\sqrt{2}}(|+1\rangle - |-1\rangle) \rightarrow |0\rangle$ which are cross polarized to each other (see figure 2.1).

2.1.1 Exciton in longitudinal and transverse magnetic field

The hamiltonian for the interaction of an electron and a hole with an external arbitrary magnetic field can be written as [41]:

$$\mathcal{H}_{\mathrm{Zeeman}} = \mu_{\mathrm{B}}\left[g_{\mathrm{e},\|}S_{\mathrm{e,z}}B_{\mathrm{z}} + g_{\mathrm{e},\perp}\left(\mathbf{S}_{\mathrm{e},\perp}\mathbf{B}_{\perp}\right)\right] - 2\mu_{\mathrm{B}}\sum_{\mathrm{i}}\left[\kappa_{\mathrm{i}}J_{\mathrm{i}}B_{\mathrm{i}} + q_{\mathrm{i}}J_{\mathrm{i}}^3B_{\mathrm{i}}\right] \qquad (2.5)$$

where μ_{B} is the Bohr magneton, $g_{\mathrm{e},\perp}$ and $g_{\mathrm{e},\|}$ are the electron g-factors in-plane and in the z direction. κ and q are the Zeeman splitting constants for the hole. For a **longitudinal magnetic field** $\mathbf{B} = (0,0,B_{\mathrm{z}})$ (Faraday geometry) and restricting as before on heavy holes only, one can rewrite the hamiltonian as:

$$\mathcal{H}^{\mathrm{long}}_{\mathrm{Zeeman}} = \left[g_{\mathrm{e},\|}S_{\mathrm{e,z}} - 2\left(\kappa_{\mathrm{z}} + \frac{9}{4}q_{\mathrm{z}}\right)J_{\mathrm{h,z}}\right]\mu_{\mathrm{B}}B_{\mathrm{z}}. \qquad (2.6)$$

Eigenenergy		Eigenfunction
symmetry $D_{2\mathrm{d}}$		
$\frac{1}{2}\left(\Delta_0+\beta_1\right)$		$\|-1\rangle$
$\frac{1}{2}\left(\Delta_0-\beta_1\right)$		$\|+1\rangle$
symmetry below $D_{2\mathrm{d}}$		
$\frac{1}{2}\left(\Delta_0+\sqrt{\Delta_1^2+\beta_1^2}\right)$		$C_1\left[\|+1\rangle+\left(\frac{\beta_1}{\Delta_1}+\sqrt{1+\frac{\beta_1^2}{\Delta_1^2}}\right)\|-1\rangle\right]$
$\frac{1}{2}\left(\Delta_0-\sqrt{\Delta_1^2+\beta_1^2}\right)$		$C_2\left[\|+1\rangle+\left(\frac{\beta_1}{\Delta_1}-\sqrt{1+\frac{\beta_1^2}{\Delta_1^2}}\right)\|-1\rangle\right]$

Table 2.2: Eigenfunctions and eigenenergies of the exciton in an longitudinal magnetic field for the symmetries $D_{2\mathrm{d}}$ and below $D_{2\mathrm{d}}$ after hamiltonian 2.8. The normalization constants C_1 and C_2 depend on the applied field B_z. Note: only the states with a total angular momentum equal to one which are optically allowed are given in the table.

In equation 2.6 it is used that for z direction the matrices of the angular momentum operator J_z and J_z^3 have the same diagonal shape. Especially the submatrices for the heavy-hole have the property $J_{\mathrm{h,z}}^3 = 9/4 J_{\mathrm{h,z}}$. Introducing the effective hole g-factor $g_{\mathrm{h,z}} = 6\left(\kappa_\mathrm{z}+\frac{9}{4}q_\mathrm{z}\right)$ one can write the hamiltonian 2.6 by using again the basis of the exciton states in matrix form :

$$H_{\mathrm{Zeeman}}^{\mathrm{long}} = \frac{\mu_\mathrm{B} B_\mathrm{z}}{2}\begin{pmatrix} \left(g_{\mathrm{e,z}}+g_{\mathrm{h,z}}\right) & 0 & 0 & 0 \\ 0 & -\left(g_{\mathrm{e,z}}+g_{\mathrm{h,z}}\right) & 0 & 0 \\ 0 & 0 & -\left(g_{\mathrm{e,z}}-g_{\mathrm{h,z}}\right) & 0 \\ 0 & 0 & 0 & \left(g_{\mathrm{e,z}}-g_{\mathrm{h,z}}\right) \end{pmatrix}. \tag{2.7}$$

Defining the new constants $\beta_1 = \mu_\mathrm{B}\left(g_{\mathrm{e,z}}+g_{\mathrm{h,z}}\right)B_\mathrm{z}$ and $\beta_2 = -\mu_\mathrm{B}\left(g_{\mathrm{e,z}}-g_{\mathrm{h,z}}\right)B_\mathrm{z}$ this yields for the total hamiltonian for symmetry $D_{2\mathrm{d}}$ and below:

$$H = H_{\mathrm{eh}} + H_{\mathrm{Zeeman}}^{\mathrm{long}} = \frac{1}{2}\begin{pmatrix} +\Delta_0+\beta_1 & +\Delta_1 & 0 & 0 \\ +\Delta_1 & +\Delta_0-\beta_1 & 0 & 0 \\ 0 & 0 & -\Delta_0+\beta_2 & +\Delta_2 \\ 0 & 0 & +\Delta_2 & -\Delta_0-\beta_2 \end{pmatrix} \tag{2.8}$$

The corresponding eigenenergies and eigenfunctions of this hamiltonian for symmetries $D_{2\mathrm{d}}$ and $< D_{2\mathrm{d}}$ are summarized in table 2.2.

Inspecting the construction of the eigenfunctions in table 2.2 leads to the following conclusion for the polarization of the transition from one of the eigenfunctions to the crystal ground state: For symmetry $D_{2\mathrm{d}}$ both optically allowed transitions are oppositely circular polarized and separated by the energy $\beta_1 = \beta_1(B_\mathrm{z})$. For symmetry below $D_{2\mathrm{d}}$ the polarization situation is more complicated, since $|+1\rangle$ and $|-1\rangle$ are no longer eigenfunctions of the system. For low magnetic fields, where $\beta_1 \ll \Delta_1$ two linearly cross polarized components separated by the electron-hole exchange energy Δ_1 can be observed. If the magnetic field is increased so that $\beta_1 \approx \Delta_1$ the emission is elliptically polarized and finally at stronger fields with $\beta_1 \gg \Delta_1$ the two components are opposite to each other circular polarized.

In **transverse magnetic fields** the situation is more complicated. The Zeeman interaction mixes bright and dark states, since the in-plane rotational symmetry is lifted by the in-plane magnetic field let say $\mathbf{B} = (B_\mathrm{x}, 0, 0)$. Consequently, the spectrum shows in addition to the two emission lines from the bright states two more emission lines from the dark states if the field is switched on. The Zeeman interaction hamiltonian for this case can be written in matrix form as:

$$H^{\mathrm{trans}}_{\mathrm{Zeeman}} = \frac{\mu_\mathrm{B} B_\mathrm{x}}{2} \begin{pmatrix} 0 & 0 & g_{\mathrm{e,x}} & g_{\mathrm{h,x}} \\ 0 & 0 & g_{\mathrm{h,x}} & g_{\mathrm{e,x}} \\ g_{\mathrm{e,x}} & g_{\mathrm{h,x}} & 0 & 0 \\ g_{\mathrm{h,x}} & g_{\mathrm{e,x}} & 0 & 0 \end{pmatrix}. \tag{2.9}$$

Where the effective hole g-factor for x-direction $g_{\mathrm{h,x}}$ is defined in accordance with the hamiltonian 2.5. It is taken into account that for the heavy-hole part the term around κ in 2.5 vanishes since $J_{\mathrm{h,x}} = 0$ and in addition $J^3_{\mathrm{h,x}}$ has only off-diagonal elements of 3/4, so this yields $g_{\mathrm{h,x}} = 3q_\mathrm{x}$.

The off-diagonal elements in the hamiltonian 2.9 causes that after diagonalizing the hamiltonian in the new eigenfunctions for non-zero B-field both bright states $|\pm 1\rangle$ as well as both dark states $|\pm 2\rangle$ are present. Consequently all four transitions become optically allowed and the energy structure is more complex. In the limit that $\Delta_1, \Delta_2 < \Delta_0$ which is applicable for the symmetry of the QDs discussed here, the energy separation between the four different components (P_i) can be written as [44]:

$$\begin{array}{|c|c|}
\hline
P_1: & +\frac{1}{4}\left[+(\Delta_1+\Delta_2)+\sqrt{(2\Delta_0+\Delta_1-\Delta_2)^2+4\left(g_{\mathrm{e,x}}-g_{\mathrm{h,x}}\right)^2\mu_\mathrm{B}^2B^2}\right] \\
P_2: & +\frac{1}{4}\left[-(\Delta_1+\Delta_2)+\sqrt{(2\Delta_0-\Delta_1+\Delta_2)^2+4\left(g_{\mathrm{e,x}}+g_{\mathrm{h,x}}\right)^2\mu_\mathrm{B}^2B^2}\right] \\
P_3: & -\frac{1}{4}\left[-(\Delta_1+\Delta_2)+\sqrt{(2\Delta_0+\Delta_1-\Delta_2)^2+4\left(g_{\mathrm{e,x}}-g_{\mathrm{h,x}}\right)^2\mu_\mathrm{B}^2B^2}\right] \\
P_4: & -\frac{1}{4}\left[+(\Delta_1+\Delta_2)+\sqrt{(2\Delta_0-\Delta_1+\Delta_2)^2+4\left(g_{\mathrm{e,x}}+g_{\mathrm{h,x}}\right)^2\mu_\mathrm{B}^2B^2}\right] \\
\hline
\end{array} \tag{2.10}$$

2.2 Spin configuration of complexes in charged QDs

Charged QDs are characterized by an additional single resident carrier. Excitation of an electron-hole pair in such a QD creates a trion [45, 46, 47]. For the further discussion it is assumed that the QD is negatively charged. Contrary to the exciton discussed above, the trion is a complex with half-integer spin. The

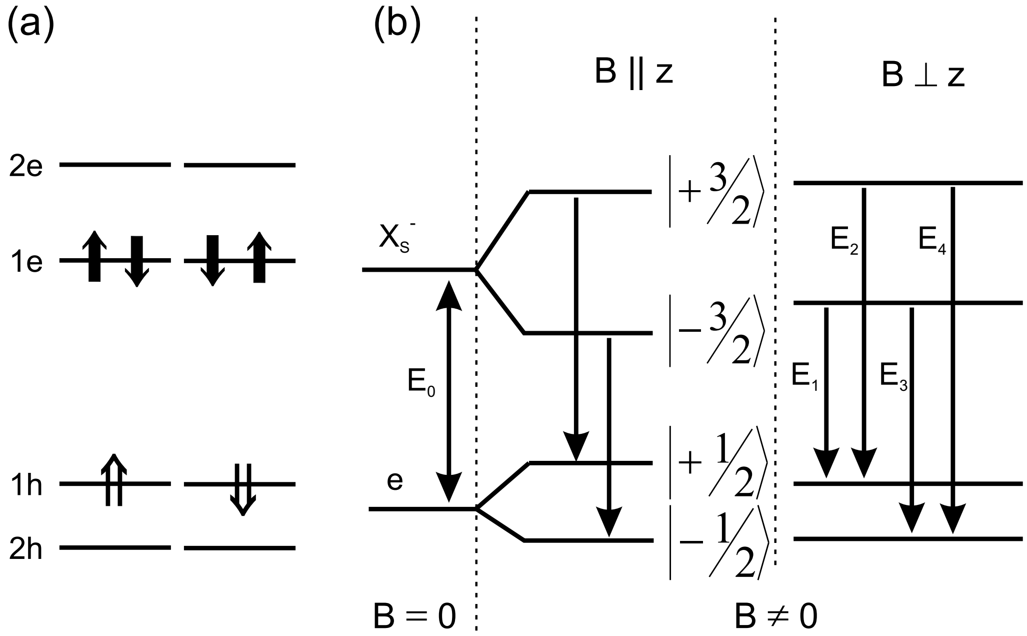

Figure 2.2: (a) Scheme of the possible spin configurations for a trion in the lowest singlet state. Each of the solid or open wide arrows represent an electron or a hole, respectively. The direction of the arrow indicates the sign of the spin. (b) Energy structure for the lowest trion singlet state for zero and for non-zero longitudinal ($B \parallel z$) and transverse ($B \perp z$) magnetic field. The solid arrows indicate the dipole allowed transitions.

eigenstates are Kramers doublets, which are degenerated in the absence of a magnetic field. In figure 2.2 the schematized energy structure of a trion is given. The empty QD is characterized by a single electron in the lowest electronic shell. The lowest trionic state is a singlet state, consisting of two electrons with antiparallel spins in the lowest electron shell and one hole in the lowest hole shell. Due to the Pauli exclusion principle the two electrons have opposite spins and the net electron spin is zero. Two important points are a result of this. First, in opposition to the exciton, there is no electron-hole exchange splitting for the lowest singlet state [44, 48]. And secondly, the total spin for the lowest singlet state is given by the spin of the hole of $J_z = \pm\frac{3}{2}$. As one will see below this makes the trion interesting for the determination of single particle properties.

The trion also has higher states, which are not directly under discussion in this work and are more focused by *Akimov* [49]. The relevant electronic states will be noted only shortly in what follows. In figure 2.2 (a) the next shells for the electron (2e) and for the hole (2h) are sketched. The first excited state is given by the hole in the second hole shell and both electrons in the lowest electron shell, where the total spin of the complex is still given by the hole spin. This is different at the next upper state, the so called trion triplet state. Here the electrons are in different shells. As a result this state has an extensive fine structure, since the electron spin configuration is more complex, which enables the presence of the electron-hole and electron-electron exchange interaction.

2.2.1 Trion in longitudinal and transverse magnetic fields

In the following subsection only the lowest trion singlet state is considered. Recombination from this state let one resident electron behind. In figure 2.2 (b) the energy structure of the lowest trion state including the dipole allowed transitions in presence of longitudinal and transverse magnetic fields is summarized. This external magnetic field acts on the heavy hole with a spin projection of $J_\mathrm{z} = \pm 3/2$ of the singlet state (initial state) in the same way like on the state of the resident electron (final state) with spin projection $S_\mathrm{e,z} = \pm 1/2$. The general form of the Zeeman interaction hamiltonian for these two cases is:

$$\mathcal{H}^\mathrm{hh}_\mathrm{Zeeman} = 2\mu_\mathrm{B}\sum_\mathrm{i}\left[\kappa_\mathrm{i} J_\mathrm{i} B_\mathrm{i} + q_\mathrm{i} J_\mathrm{i}^3 B_\mathrm{i}\right] \tag{2.11}$$

$$\mathcal{H}^\mathrm{e}_\mathrm{Zeeman} = \mu_\mathrm{B}\sum_\mathrm{i} g_\mathrm{e,i} B_\mathrm{i}\ \mathbf{S}_{e,\mathrm{i}} \tag{2.12}$$

where $i = \{x, y, z\}$ denotes the cartesian coordinates, $g_\mathrm{e,i}$ the components of the electron g-factors, and κ, q are the Zeeman splitting constants as already used in the previous section, respectively.

In case of a **longitudinal magnetic field** with $\mathbf{B} = \{0, 0, B_\mathrm{z}\}$, the J_z and $S_\mathrm{e,z}$ are still good quantum numbers and the hamiltonians for the trion heavy hole and the resident electron can be written in matrix form with the basis $|\pm 3/2\rangle$ and $|\pm 1/2\rangle$ respectively, as:

$$H^{\alpha,\mathrm{long}}_\mathrm{Zeeman} = \frac{\mu_\mathrm{B}}{2} g_{\alpha,\mathrm{z}} B_\mathrm{z} \begin{pmatrix} 1 & 0 \\ 0 & -1 \end{pmatrix} \tag{2.13}$$

with $\alpha = \{h, e\}$ and with $g_\mathrm{h,z}$ the heavy hole g-factor as defined in the last section. Here, the total splitting of the initial and final state is given by $\Delta_\alpha = \mu_\mathrm{B} g_{\alpha,\mathrm{z}} B_\mathrm{z}$, as indicated in Fig. 2.2. So the total magnetic field dependent energy splitting of the two PL components resulting from the two optically allowed transitions $|\pm 3/2\rangle \rightarrow |\pm 1/2\rangle$ is

$$\Delta E = \mu_\mathrm{B}\left(g_\mathrm{h,z} - g_\mathrm{e,z}\right) B_\mathrm{z}. \tag{2.14}$$

For a **transverse magnetic field** the situation looks different. The field lifts the in-plane symmetry and couples both substates of the hole as of the resident electron so that J_z and $S_\mathrm{e,z}$ are no longer good quantum numbers. Consequently, all four possible transitions become optically allowed. The Zeeman hamiltonian written in the same basis as above for a magnetic field along x direction reads as:

$$H^{\alpha,\mathrm{trans}}_\mathrm{Zeeman} = \frac{\mu_\mathrm{B}}{2} g_{\alpha,\mathrm{x}} B_\mathrm{x} \begin{pmatrix} 0 & 1 \\ 1 & 0 \end{pmatrix}. \tag{2.15}$$

Diagonalization of this hamiltonian leads to the eigenfunctions for the lowest trion singlet state and for the final resident electron of $1/\sqrt{2}\left(|+3/2\rangle \pm |-3/2\rangle\right)$

and $1/\sqrt{2}\,(|+1/2\rangle \pm |-1/2\rangle)$, respectively. The separation between the four different components is given by:

$$\begin{array}{|r|l|}\hline E_1: & -\frac{\mu_\mathrm{B}}{2}\left(g_{\mathrm{h,x}}+g_{\mathrm{e,x}}\right)B_x \\ E_2: & +\frac{\mu_\mathrm{B}}{2}\left(g_{\mathrm{h,x}}-g_{\mathrm{e,x}}\right)B_x \\ E_3: & -\frac{\mu_\mathrm{B}}{2}\left(g_{\mathrm{h,x}}-g_{\mathrm{e,x}}\right)B_x \\ E_4: & +\frac{\mu_\mathrm{B}}{2}\left(g_{\mathrm{h,x}}+g_{\mathrm{e,x}}\right)B_x \\ \hline\end{array} \tag{2.16}$$

where E_i with $i = 1..4$ indicates the transitions as labelled in Fig. 2.2 (b). As seen in equation 2.16 the energy position of the four components is a function of the magnetic field strength. This enables the possibility to calculate the heavy-hole- and the electron- g-factor:

$$\begin{aligned} g_{\mathrm{h,x}} &= \frac{1}{2\mu_\mathrm{B}}\left(E_4 - E_3 + E_2 - E_1\right)\cdot B_x \\ g_{\mathrm{e,x}} &= \frac{1}{2\mu_\mathrm{B}}\left(E_4 + E_3 - E_2 - E_1\right)\cdot B_x \end{aligned} \tag{2.17}$$

where E_i denotes the energetically position of the four PL components.

2.3 Relaxation in QDs

The two terms relaxation and recombination describe interactions which change the state of an excitation in a semiconductor. Two types of relaxation can be distinguished. One is phase relaxation where the phase of the state is changed but the occupation can remain and the other is energy relaxation, where both phase and occupation are changed.

The phase relaxation can be described by the phenomenological introduction of a characteristic time T_2. This *phase relaxation time* describes the decay of the macroscopic polarization. It is connected with the homogeneous broadening of the emission line for a transition by

$$\gamma = \frac{1}{T_2}. \tag{2.18}$$

Since the phase relaxation is limited by the energy relaxation it is useful to introduce an additional time constant T_2' describing pure phase relaxation which does not change the occupation of the state:

$$\frac{1}{T_2} = \frac{1}{2T_1} + \frac{1}{T_2'} \tag{2.19}$$

where T_1 is the life time of the specific state. The incoherent part of the intensity decays exponentially with $I_{\mathrm{incoh}}(t) \propto \exp\left(-t/T_1\right)$, while the coherent part of the intensity has a quadratic dependence on the polarization $I_{coh} \propto |P(t)|^2 \propto$

$|\exp(-t/T_2)|^2 = \exp(-2t/T_2)$. This yields in case of purely radiative damping ($I_{incoh} = I_{coh}$): $2T_1 = T_2$.

While the occupation of a state remains unchanged during the pure phase relaxation, for *energy relaxation* this is not the case. Two groups of processes can be distinguished, both fulfilling energy conservation. The radiative recombination is always connected with the emission of an electromagnetic wave. In contrast, the non-radiative recombination is connected with the transfer of energy to the lattice by the emission of phonons, population of other states lower in energy or other non-radiative processes. The total life time T_1 can be split in two terms in accordance to the two processes in the form:

$$\frac{1}{T_1} = \frac{1}{\tau_{\mathrm{rad}}} + \frac{1}{\tau_{\mathrm{non-rad}}}. \tag{2.20}$$

2.4 Homogeneous versus inhomogeneous broadening

A central tool in spectroscopy is the measurement of a time-integrated spectrum of an emission, which uncovers information about the energy structure of the sample. But there is more information in it. As it will be demonstrated later the emission from the ground state exciton in a single QD is a narrow line. Its width can carry information about the timescale for dephasing if it can be resolved by the experimental setup. How and what is fundamental for this will be discussed in what follows.

Homogeneous broadening: If there is a set of states, which undergo a radiative recombination to lower laying states, all with the same transition energy $\hbar\omega_x$, the total emitted electric field can be described by a decaying wave with a central frequency corresponding to the transition energy. As discussed above the time evolution of this emission is damped by the time constant $T_2 = 1/\gamma$ defined by equation 2.19 combining phase and energy relaxation. The electric field reads: [50]:

$$E(t) = \frac{1}{2}\, E_0\, e^{-\gamma t} \cdot e^{i\omega_x t} + \text{c.c.} \tag{2.21}$$

In the spectral domain this damping yields a spectral broadening. It can be calculated taking the Fourier transformation of 2.21 which yields:

$$\begin{aligned} E(\omega) &= \frac{1}{\sqrt{2\pi}} \int_{-\infty}^{\infty} E(t) \cdot e^{i\omega t} dt \\ &= \frac{E_0}{2\sqrt{2\pi}} \left[\frac{\gamma}{i(\omega-\omega_0)+\gamma} + \frac{\gamma}{i(\omega+\omega_0)+\gamma} \right]. \end{aligned} \tag{2.22}$$

Since the measured spectrum corresponds to the intensity $I(\omega) = E(\omega)\, E^*(\omega)$, this yields with the assumption $(\omega-\omega_0)^2 \ll \omega_0^2$:

$$I_{\omega_0}(\omega) \propto \frac{\gamma}{(\omega-\omega_0)^2 + \gamma^2}, \tag{2.23}$$

which is a Lorentzian line profile. Its full width at half maximum $\Delta\omega_{\mathrm{FWHM}} = \gamma$ is called *natural line width* and given only by the finite lifetime of the upper state and the loss of phase memory by elastic scattering processes.

Inhomogeneous broadening: This kind of broadening is given if the transition energy $\hbar\omega_x$ is not well defined. As an example, the emission from an ensemble of QDs is inhomogeneously broadened since every dot has a slightly different ground state energy. Or if the ground state energy of an exciton in a single QD is jittering in time, the time integrated PL will be also inhomogeneously broadened. The line profile in this case will be strongly dependent on the distribution function $g(\omega_x, \omega_0, \Gamma)$ for ω_x centered at ω_0 with the characteristic width Γ. The resulting spectral line profile is defined by the convolution between the Lorentzian profile from the homogeneous broadening and $g(\omega_x, \omega_0, \Gamma)$ and can be written as:

$$I_{\mathrm{inhom}} = \int_{-\infty}^{\infty} \frac{\gamma}{(\omega - \omega')^2 + \gamma^2}\, g(\omega', \omega_0, \Gamma)\, d\omega'. \tag{2.24}$$

Often $g(\omega_x, \omega_0, \Gamma)$ is a Gaussian distribution, but as will be demonstrated in section 5.3.3 it can be non-Gaussian. Which of both distributions dominates the final line profile depends on the relation between γ and Γ and can be Lorentzian ($\gamma > \Gamma$), Gaussian ($\gamma > \Gamma$) or even the Voigt profile ($\gamma \approx \Gamma$).

In general, while the lifetime T_1 of a state can be easily measured by time resolved spectroscopical methods, the dephasing time T_2 can be extracted from the homogeneous line width if the Lorentzian shaped line profile can be resolved. If the resolution is not enough (see section 4.1) or the line is inhomogeneously broadened (see section 5.3.3) then the extracted width gives only a lower boundary.

2.5 Basic considerations about coherence in QDs

Coherence is the central term in this thesis. It is often used in a lot of different domains of physics with slightly different meanings. The general definition is that two processes are coherent if they are characterized by a well defined phase relationship. In the present case these processes are quantum mechanical states in semiconductor quantum structures. In this context *coherence* describes the ability of the states $|X_1(t)\rangle$ and $|X_2(t)\rangle$ to maintain a coherent superposition of the form $|X(t)\rangle = \alpha|X_1(t)\rangle + \beta|X_2(t)\rangle$ already mentioned in the introductory chapter. Independent of the real nature of these two states two cases can be qualitatively distinguished [11, 51]. On one hand, both states can be identical but $|X_1(t_1)\rangle$ and $|X_2(t_2)\rangle$ are excited at different time points t_1 and t_2. This case is called *optical coherence*. On the other hand, $|X_1(t)\rangle$ and $|X_2(t)\rangle$ can represent two states which are different in their physical meaning, e.g. different spin states, may also be with different energies. In this case, one speaks about *quantum coherence*.

In the following two sections a clear distinction between optical coherence and quantum coherence will be worked out. Furthermore, in the later discussion of

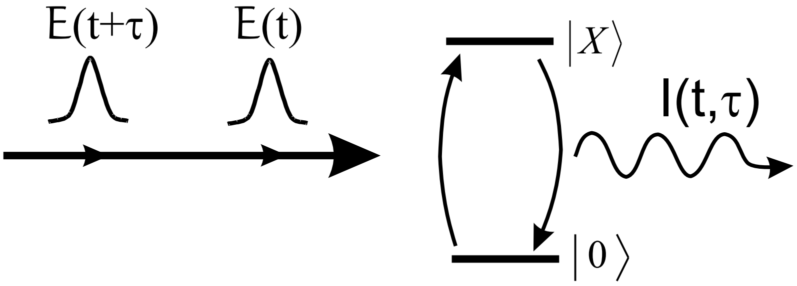

Figure 2.3: Optical coherence: the state $|X\rangle$ is coupled to an external electromagnetic wave consisting of two pulses separated by the total delay time τ.

the experimental results it will be demonstrated that spin relaxation processes can be divided in two qualitatively different groups. But at first the physical background of this division will be explained.

2.5.1 Optical coherence in semiconductors

In this work the term *optical coherence* is used to describe the coherence properties of a state on an 'external' time scale, see Fig. 2.3. The term 'optical' does not mean that this discussion is going on optical interferences of two electromagnetic waves. On the contrary, the discussion here is on the quantum interference of two wave functions created at two different points in time by two separate excitation pulses in the same state. In fact, if there exists an excited state $|X\rangle$ which is radiatively coupled to the crystal ground state $|0\rangle$, the wave functions after excitation with a short pulse $\varepsilon_1(t)$ resonant to the transition energy E_x is given by $|X^{(1)}(t)\rangle = \exp(-i\omega_x t)\,|E_x\rangle$ with $\omega_x = E_x/\hbar$. In case of two identical excitation pulses separated by the delay time τ the total wave function reads as:

$$\begin{aligned} |X(t,\tau)\rangle &= |X^{(1)}(t)\rangle + |X^{(2)}(t+\tau)\rangle \\ &= e^{-i\omega_x t}|E_x\rangle + e^{-i\omega_x (t+\tau)}|E_x\rangle. \end{aligned} \tag{2.25}$$

Here the low excitation limit is considered. Equation 2.25 represents the sum of two quantum mechanical paths connecting the initial and final states. The quantum interference between these two paths can be observed by monitoring the occupation of the excited state created by these two pulses in dependence on the delay time τ. The occupation reads as:

$$\begin{aligned} N_x &= \int_{-\infty}^{\infty} \langle X(t,\tau)\,|X(t,\tau)\rangle dt \qquad (2.26) \\ &= \int_{-\infty}^{\infty} \left[\langle X^{(1)}|X^{(1)}\rangle + \langle X^{(2)}|X^{(2)}\rangle + 2\Re e\left(\langle X^{(1)}(t)\,|X^{(2)}(t+\tau)\rangle\right)\right] dt. \end{aligned}$$

While the two first terms in 2.26 are constant if the delay is changed, the third one carries the ability for interference and changes from constructive to destructive interference. Using 2.25 this component reads:

$$\int_{-\infty}^{\infty} \Re e\langle X^{(1)}(t)|X^{(2)}(t+\tau)\rangle dt = \cos(\omega_x\tau)\int_{-\infty}^{\infty}\langle E_x|E_x\rangle dt \tag{2.27}$$

So, by varying the delay time τ, oscillations in the occupation of N_x with a period of $T = h/E_x$ can be observed.

The interference here discussed is somehow analogous to Young's double slit experiment. There the interference takes place as long as it can not be distinguished, which of the different paths the photon has used if it reaches the detector. Any successful attempts to identify the used path yield a disappearing of the interference. Here, the situation is equivalent, because it is not clear which of the two excitation pulses has generated the occupation in the upper state.

The last term in equation 2.27 carries a complete characterization of the wave function $|X\rangle$ generated by both pulses, accessible if their shape is known [52]. In general, if both pulses are the same (see coherent control experiments in section 5.3) this term contains the autocorrelation function of the wave functions of $|X\rangle$. This autocorrelation function is in total analogy to the autocorrelation arising from the interference between two equal light fields.

The undamped oscillation 2.27 is only valid for infinite long dephasing times. In order to include dephasing, an additional phenomenological phase term has to be added in 2.25 so that $i\omega_x \rightarrow i\omega_x + \gamma_x/\hbar$. This term leads to an exponential decay of the oscillation in the occupation N_x of the form:

$$N_x \propto \cos(\omega_x\tau)\, e^{-\gamma_x t/\hbar} \tag{2.28}$$

and manifests a loss of the optically induced coherence.

2.5.2 Quantum coherence in semiconductors

The term *quantum coherence* is used in this work to describe the coherence properties of states on an 'internal' time scale. Here the time evolution of the phase of two states is compared with each other. In contrast to the optical coherence

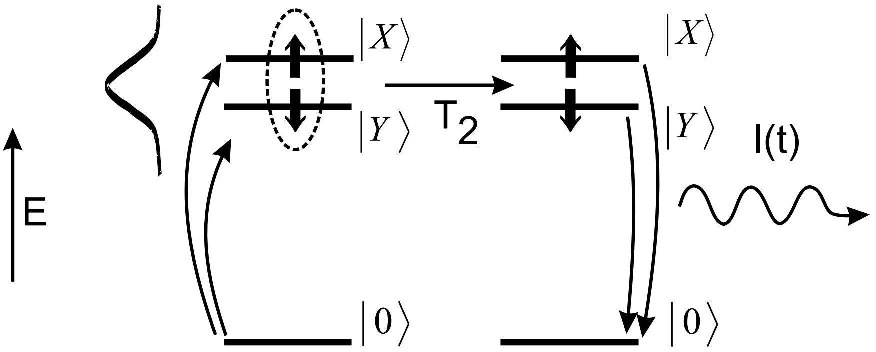

Figure 2.4: Quantum coherence: Three level system consisting of the crystal ground state $|0\rangle$ and two excited states $|X\rangle$ and $|Y\rangle$ closely adjacent in energy.

discussed in the preceding section, scattering processes which are acting on both states in the same way and leading to the same phase shift in both states have no effect on the observed evolution. The situation is summarized in figure 2.4. Let's assume there are two states $|X\rangle$ and $|Y\rangle$, both of excitonic nature, which are coupled to a common crystal ground state, but with different transition energies. In what follows, it will be shown that this energy difference leads to a beating in the population of the exciton system if the two states $|X\rangle$ and $|Y\rangle$ have a fixed phase relation to each other. By tracing the temporal evolution of this beating one can directly monitor how the exciton system evolves from an initially coherent state to finally a incoherent one.

Principle of quantum beat spectroscopy

The quantum beats are based on the concept of coherent superposition of quantum mechanical states. It can only be directly applied between two states closely adjacent in energy. These states can result from two excitonic states with a different spin configuration, where the degeneracy is perhaps lifted by magnetic field or electron-hole exchange interaction. A single excitation pulse with a spectral distribution larger than the energy separation $\Delta E = E_{\mathrm{x}} - E_{\mathrm{y}}$ of the two states can excite both states simultaneously with a well defined phase relation. The resulting total wave function of the exciton system is given by a coherent superposition of the subwave functions in the form:

$$|\Psi\left(t=0\right)\rangle \;=\; c_{\mathrm{x}}|X\left(t=0\right)\rangle \;+\; c_{\mathrm{y}}|Y\left(t=0\right)\rangle. \tag{2.29}$$

Here, the coefficients c_{x} and c_{y} are probability amplitudes that represent the transition dipole moments for absorption into each of the substates, depending also on the spectral distribution of the laser with respect to the transition energies.

As in the previous section, it is useful for discussing the time evolution to separate the time dependent part in the wave functions from the remaining one. One can write equation 2.29 in the form:

$$\begin{aligned} |\Psi\left(t\right)\rangle \;=\;& c_{\mathrm{x}}\exp\left(-i\omega_{\mathrm{x}}t-\frac{t}{2T_1}-i\phi_{\mathrm{x}}(t)\right)|X\rangle + \\ &+ c_{\mathrm{y}}\exp\left(-i\omega_{\mathrm{y}}t-\frac{t}{2T_1}-i\phi_{\mathrm{y}}(t)\right)|Y\rangle, \end{aligned} \tag{2.30}$$

where $\omega_{\mathrm{x,y}} = E_{\mathrm{x,y}}/\hbar$ and $\phi_{\mathrm{x,y}}(t)$ represents the phase evolution for the two states. In addition, the finite lifetime of the population is taken into account by the phenomenological time T_1. So far - for simplicity - it is assumed that this lifetime is the same for both states $|X\rangle$ and $|Y\rangle$.

The population of the exciton system is given by the expectation value $\langle\Psi\left(t\right)|\Psi\left(t\right)\rangle$ of the total wave function. It can be monitored by the emission resulting from the transition to the crystal ground state ($|\Psi\left(t\right)\rangle \rightarrow |0\rangle$). Considering only dipole allowed transitions with respect to the dipole operator D, the emitted intensity can be calculated from the dipole matrix element between crystal ground state and the exciton substates in accordance to:

$$\begin{aligned} I\left(t\right) &\propto \mid \langle 0|D|\Psi\left(t\right)\rangle \mid^2 \qquad (2.31)\\ &= \left(c_{\mathrm{x}}^2|M_{\mathrm{x}\to 0}|^2 + c_{\mathrm{y}}^2|M_{\mathrm{y}\to 0}|^2\right)\exp\left(-\frac{t}{T_1}\right) + \\ &\quad +2c_{\mathrm{x}}c_{\mathrm{y}}\cdot \Re e\left(M_{\mathrm{x}\to 0}M_{\mathrm{y}\to 0}\cdot \exp\left[-i\omega_{\mathrm{x-y}}t + i\phi_{\mathrm{x-y}}\left(t\right)\right]\right)\cdot \exp\left(-\frac{t}{T_1}\right) \end{aligned}$$

with $\omega_{\mathrm{x-y}} = |\omega_{\mathrm{x}} - \omega_{\mathrm{y}}|$ and $\phi_{\mathrm{x-y}}\left(t\right) = \phi_{\mathrm{x}}\left(t\right) - \phi_{\mathrm{y}}\left(t\right)$. The $M_{\mathrm{x}\to 0}$ and $M_{\mathrm{y}\to 0}$ represent the dipole matrix elements for the separate substates into the crystal ground state. Assuming that the probability for dephasing between the two states can be described by an exponential decay with the pure dephasing time $T_2^{'}$ the equation 2.31 can be cast into the form

$$I\left(t\right) \propto A\cdot \exp\left(-\frac{t}{T_1}\right) + B\cdot \exp\left(-\frac{t}{T_2}\right)\cdot \cos\left(\omega_{\mathrm{x-y}}t\right) \qquad (2.32)$$

where equation 2.19 was used. The final equation 2.32 is separated in two qualitatively different terms. The first term represents a background independent from the phase of the two states or its energy separation. It decays with the lifetime of the exciton states. The second term monitors the quantum coherence between the two states $|X\rangle$ and $|Y\rangle$ of the exciton system. It oscillates with the angular frequency $\omega_{\mathrm{x-y}} = \Delta E/\hbar$ given by the energy separation ΔE of the two states and decays with phase relaxation time T_2.

Density matrix formulation

Above it was assumed that the lifetime for the two substates is equal. This is not necessarily the case, there can be redistributions of the occupation from one substate to the other. For this reason and also in order to make averaging in time (e.g. for several excitation events) easier one can introduce a more convenient form. As stated above, the population of the exciton system is described by the expectation value $\langle\Psi\left(t\right)|\Psi\left(t\right)\rangle$. The density operator, defined by

$$\rho = |X\rangle\langle X| + |Y\rangle\langle Y| \qquad (2.33)$$

can be written in matrix form. With use of equation 2.30 it reveals the different components of the population. The matrix is written in the basis of the subwavefunctions $|X\rangle$ and $|Y\rangle$ and reads as

$$\rho = \left[\begin{array}{cc} c_{\mathrm{x}}c_{\mathrm{x}}^*\cdot e^{(-t/T_{1,\mathrm{x}})} & c_{\mathrm{x}}c_{\mathrm{y}}^*\; e^{-i\omega_{\mathrm{x-y}}t}\; e^{i\phi_{\mathrm{x-y}}(t)}\; e^{(-t/T_1)} \\ c_{\mathrm{x}}^*c_{\mathrm{y}}e^{i\omega_{\mathrm{x-y}}t}\; e^{i\phi_{\mathrm{x-y}}(t)}\; e^{(-t/T_1)} & c_{\mathrm{y}}c_{\mathrm{y}}^*\cdot e^{(-t/T_{1,\mathrm{y}})} \end{array}\right]. \qquad (2.34)$$

The times $T_{1,\mathrm{x}}$ and $T_{1,\mathrm{y}}$ represent the population lifetimes for the two substates.

The off-diagonal elements in 2.34 carrying the interference between the two substates $|X\rangle$ and $|Y\rangle$. They are equivalent to the second term in equation 2.32. If the off-diagonal elements are non-zero then the state $|\Psi\left(t\right)\rangle$ is called a coherent superposition. The time evaluation of the off-diagonal elements is given by the

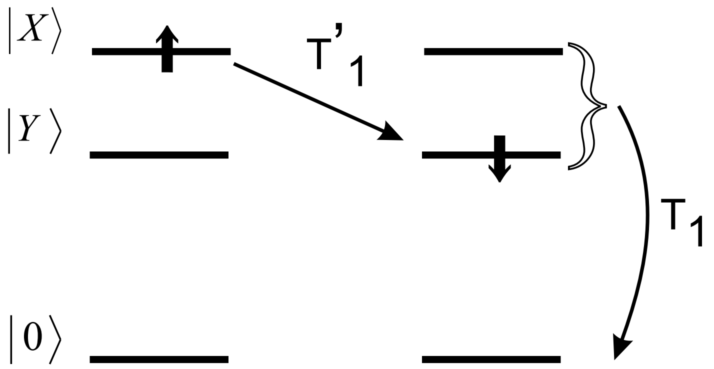

Figure 2.5: Longitudinal relaxation times: Three level system demonstrating the population difference decay time $T_1^{'}$ and the average level decay time T_1.

behavior of the phase $\phi_{\mathrm{x-y}}(t)$ and by the life-time decay with the characteristic time $1/T_1 = 1/T_{1,\mathrm{x}} + 1/T_{1,\mathrm{y}}$. Assuming as above an exponential decay for the phase relation $\exp(\phi_{\mathrm{x-y}}(t)) \rightarrow \exp\left(-t/T_2^{'}\right)$ one can express the decay of the off-diagonal elements in 2.34 by a single characteristic time. In accordance to equation 2.19 one can introduce the *transverse relaxation time* T_2:

$$\frac{1}{T_2} = \frac{1}{2T_1} + \frac{1}{T_2^{'}}. \tag{2.35}$$

The off-diagonal elements read then $c_{\mathrm{x}} c_{\mathrm{y}}^{*} \exp(-i\omega_{\mathrm{x-y}} t - t/T_2)$. Since the phase $\phi_{\mathrm{x-y}}(t)$ describes only the phase relation between the two states $|X\rangle$ and $|Y\rangle$, the transverse relaxation time T_2 describes the quantum coherence of the two states. Since the phase relation is lost if the exciton lifetime is over the average lifetime T_1 is limiting T_2.

2.5.3 Longitudinal relaxation times

The diagonal elements of the density matrix 2.34 for a total state $|\Psi(t)\rangle$ represent the population of the substates $|X\rangle$ and $|Y\rangle$. This is independent from a possibly existing phase relation between the states ($\phi_{\mathrm{x-y}}(t)$ does not enter the diagonal elements) and so the state $|\Psi(t)\rangle$ is called an incoherent superposition if the corresponding density matrix ρ has a diagonal shape.

The diagonal elements of 2.34 ρ_{xx} and ρ_{yy} describe the occupation of the states $|X\rangle$ and $|Y\rangle$ respectively. Since we are in a three level system, the system is only completed taking the occupation of the third state, the crystal ground state $|0\rangle$, into account, only the sum of all occupations is constant, $\rho_{\mathrm{xx}} + \rho_{\mathrm{yy}} + \rho_0 = 1$. Consequently, as sketched in figure 2.5, two relaxation times for the occupations are possible:

$$\begin{aligned} T_1^{'} &: \rho_{\mathrm{xx}} - \rho_{\mathrm{yy}} \\ T_1 &: \rho_{\mathrm{xx}} + \rho_{\mathrm{yy}}. \end{aligned} \tag{2.36}$$

The $T_1^{'}$ time describes the reorganization of occupation inside the exciton state consisting of the $|X\rangle$ and $|Y\rangle$ substates, while T_1 is the general lifetime in the excited state and describes the recombination into the crystal ground state $|0\rangle$. Both times are called *longitudinal relaxation times* since they influence real occupations. While the average level decay time T_1 is always connected with energy relaxation, for the population difference decay time $T_1^{'}$ this is only the case if the $|X\rangle$ and $|Y\rangle$ substates are not degenerated.

Chapter 3

Experimental basics

In this chapter an overview about the used sample structure will be given followed by a short description of the sample preparation technologies. Then the experimental methods applied for single dot spectroscopy are discussed. In a second part the methods used for the different experiments in the time-, polarization- and/or magnetic-field domain are introduced.

3.1 The sample structure

The investigated samples are self-assembled quantum dots from the group of II-VI semiconductors, provided by the MBE laboratory of the Institute of Physics of the Humboldt-Universität zu Berlin.

The group of II-VI compounds has several advantages in comparison to the III-V semiconductors which are intensively under investigation. The Coulomb interaction energies are here one order of magnitude larger [55, 43]. This yields a larger separation between exciton- and biexciton- states making their emissions more easily separable by spectroscopic methods. The large biexciton binding energy also enables excitation scenarios as pulsed two photon excitation of the single biexciton as will be discussed later. Furthermore, the fine structure split-

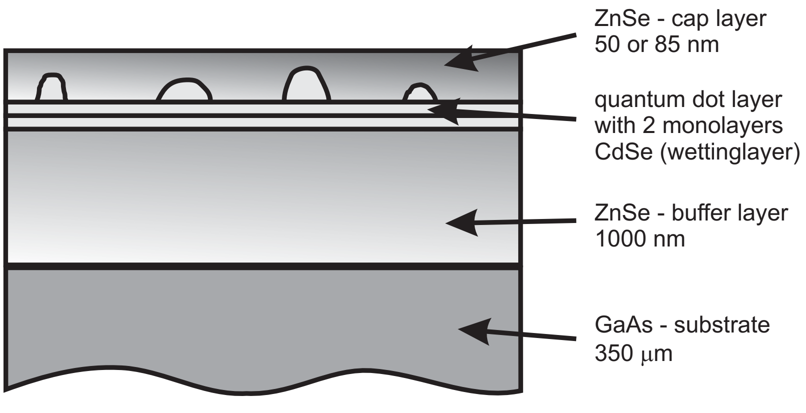

Figure 3.1: Scheme of the used CdSe/ZnSe quantum dot structures

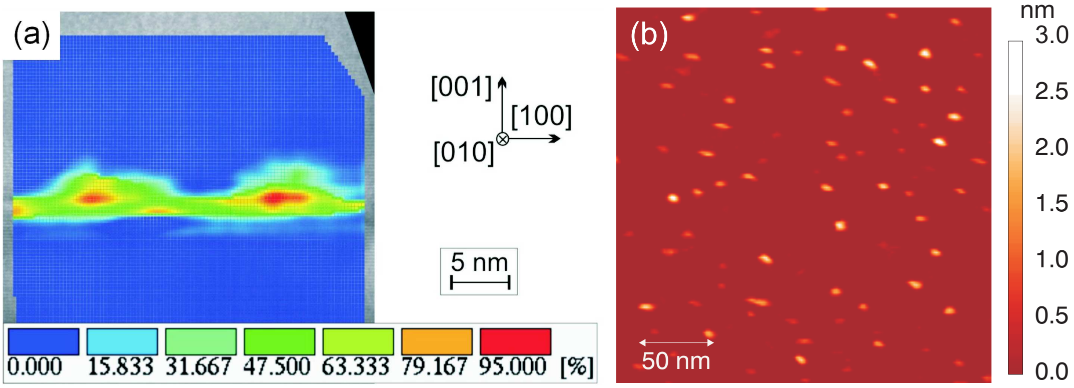

Figure 3.2: (a) Cadmium concentration in the QD-sample evaluated from a cross section HRTEM image using the CELFA method [53]. (b) AFM image of the uncapped quantum dot layer demonstrating its typical distribution [54].

ting of the exciton states is much larger here compared with III-V compounds. This leads to a clearer manifestation of the QD symmetry by well resolved fine structure components [56, 57, 58].

The CdSe/ZnSe QD structures are grown by molecular-beam-epitaxy (MBE) in the phase locked epitaxy mode. There the growing process (mainly the opening times of the material sources) is controlled by the phase of the RHEED oscillations (reflection of high energy electron diffraction). This allows the growth of single monolayers. The formation of the QDs is achieved by a thermal activation procedure [59], enabling maximum control and reproducibility of the formation process.

The structure of the samples is sketched in figure 3.1 including the typical thicknesses. The CdSe quantum dots are on the top of a two monolayers thick CdSe wetting layer surrounded by the ZnSe buffer- and cap-layer. One of the advantages of these samples is that in contrast to other CdSe quantum structures [60], [61] these dots consist of an ultrapure CdSe core. This is revealed by examinations using high resolution transmission electron microscopy (HRTEM) connected with a special data analysis method CELFA[1] (see figure 3.2(a)). Furthermore in this examination the dimension of the pure CdSe core is found to be about 2 nm in height with a lateral extension below 10 nm. The samples are naturally weakly n-doped [63].

The density of the QDs was found to be $\rho_{\mathrm{QD}} \approx 10^{10}\ \mathrm{cm}^{-2}$ from atomic force microscopy (AFM, see figure 3.2 (b)) which was done *in-situ* directly after growth, before the sample was covered by the ZnSe cap layer. This ensemble of QDs has a size distribution. The energy position of the states in a single QD is strongly correlated with the size of the specific dot [64, 65]. In figure 3.3 (a) it is demonstrated by ensemble data that this size distribution yields an inhomogeneous broadening of the PL emission. It is clearly seen that the contributions of the different QDs

---

[1] CELFA = composition evaluation by lattice fringe analysis, which was done on the samples used here in the group of D. Gerthsen, Karlsruhe (for details see [62]).

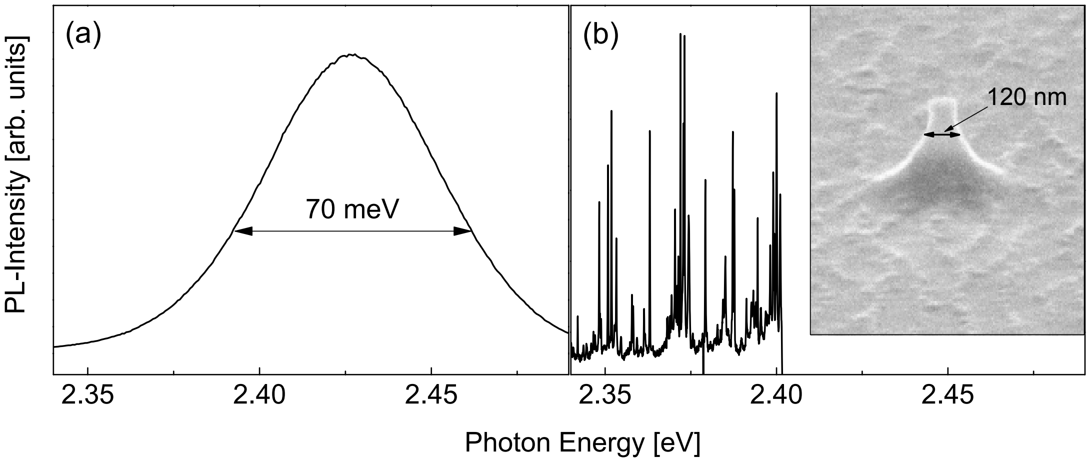

Figure 3.3: Emission from CdSe QDs: (a) Ensemble of 10^6 QDs and (b) single QD emission lines from a small mesa structure containing less than 15 QDs. Inset: Scanning electron microscopy (SEM) picture of a typical (small) mesa.

can not be spectrally separated. So, in order to perform single dot spectroscopy a higher spacial resolution is necessary, which reduces the number of QDs. As it will be discussed in the next section the maximum spatial resolution of the used micro optical setup is in the range of 1 μm^2. This leads with the above given QD density to nearly 1000 dots which are still too many in order to perform single dot spectroscopy.

Structuring of the sample surface for higher spacial resolution

In this work the appropriate spatial resolution is provided by mesa structures on the sample surface. These mesas are produced on the ready grown samples by creating a mask by electron beam lithography, and wet chemical etching. The resulting mesas have intentionally different sizes. In the inset of figure 3.3 (b) a scanning electron microscopy image of a typical small mesa is shown. The diameter of the smallest mesas is smaller than 120 nm, which leads to approximately 10 to 15 QDs on this mesa which will contribute to the signal. The height of the mesa is between 250 and 300 nm so that the quantum dot layer is surely removed in the vicinity of the mesa. Due to the fact that the number of QDs in a mesa is much smaller, the PL emission is clearly different in comparison to the emission from an ensemble. In figure 3.3 (b) the emission from a small mesa is plotted, where the single emission lines from the different QDs are spectrally well separated. An additional advantage of the mesa structures is the high reproducibility. With use of a micro PL setup (see next section) one can address a single mesa which always contains the same QDs, so that experiments can be easily reproduced and a once selected QD is available over long measuring periods.

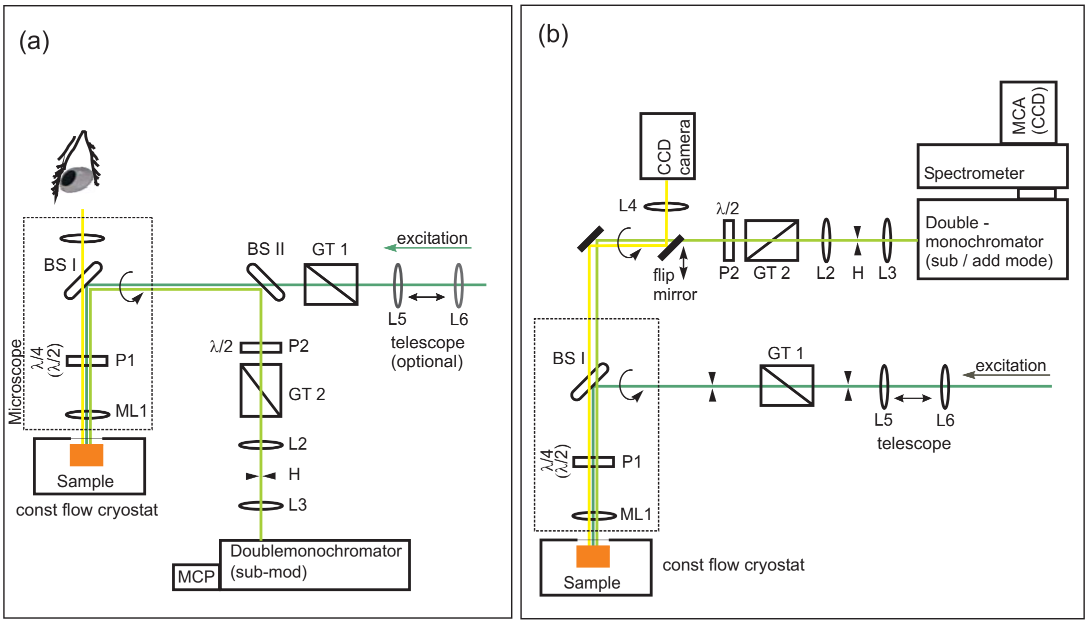

Figure 3.4: Microoptical setup: a.) optimized for polarization control (as used in sections 5.1 and 5.2.2) and b.) optimized for better signal transmission, including a three stage spectrometer (as used for interferometric measurements in section 5.3). Note: the circular arrows indicate that the beamway in the microscope is perpendicular to the paper plane.

3.2 Experimental methods

3.2.1 Microoptical setup

For all experiments discussed in this work it is of central importance to have an efficient long term stability and to collect a maximum of the emission from the QDs. Both need to be done under accurate polarization control for excitation and emission.

In order to achieve this, a microoptical setup in confocal geometry is used (see figure 3.4(a)). Confocal means that inside the microscope the excitation laser and the collected PL use the same beamway. So on one hand, the microscope objective (NA = 0.46) is used to focus the parallel laser beam on the sample surface, and on the other hand it collects the PL and forms a parallel beam from it. In such a configuration at least one beamsplitter is necessary to separate the excitation laser from the detected PL. Since for the main experiments the excitation energy is always close to the detection energy the beamsplitters have a ratio of transmission versus reflection of nearly 50 : 50.

The setup sketched in figure 3.4(a) is optimized for maximal polarization control. Since the reflectivity and transmission of a beamsplitter plate is different for light which is parallel or perpendicularly polarized in respect to the reflection plane, a compensation is necessary. In order to achieve this, two identical beamsplitter plates (BSI and BSII) are used which are rotated 90 degrees against each other. In the figure, this is indicated by the curved arrow. The beamway in the microscope is in the experiment perpendicular to the table plane. The excitation polarization is fixed by the Glan-Thomson polarizer GT2 exactly parallel or perpendicular (depending on experiment) with respect to the beamsplitter BSII. The PL is reflected on both beamsplitters. Light which is parallelly polarized in respect of BSI is perpendicularly polarized in respect of BSII, so the total reflectivity is independent from the polarization. The polarization of the PL is analyzed by a lambda half plate in connection with the Glan-Thomson polarizer GT2 in front of the spectrograph. This is only done for polarizations which are parallel or perpendicular to the BSI and BSII reflection planes, so that both beamsplitters can optimally compensate its respective reflectivity.

In order to analyze the QD emission for different linear polarization angles in accordance to the sample main axes or to analyze the circular polarization at the position P1 a $\lambda/2$- or a $\lambda/4$- plate is introduced directly in front of the microscope objective. This way of polarization measurement offers a polarization resolution of about 2%.

There are experiments which require a high detection efficiency rather than a high polarization accuracy, as e.g. the interferometric measurements conducted here. As will be discussed later, for this a triple spectrograph is used, which provides a parallel detection of one or two wavelength ranges in connection with a better scattered light reduction. The smaller detection efficiency due to the larger number of optical elements in it can only be compensated by a higher efficiency in the PL collecting and guiding part of the experiment. In order to achieve this, the setup discussed above is modified (see figure 3.4(b)). Mainly, there is only one beamsplitter used to coincide excitation and detection beamway. In this setup it is not possible to monitor the microscope picture during the measurement. This can only be done by introducing a flip mirror into the detection beamway. If the intensities of measurements with different polarization configurations should be compared with each other, the reflectivity of the beamsplitter for the respective polarizations needs to be carefully measured.

The spot diameter of the laser on the sample is usually $3\mu m$, one order larger than the typical diameter of the mesa. This produces an efficient long term stability. The sample is placed in an LHe cooled constant flow cryostat which is motorized. By observing the microscope picture it is possible with a high reproducibility to select a specific mesa.

Since the excitation energy is always close to the detection energy, efficient scattering light suppression is essential. This is achieved by using a 50 μm pinhole (H) together with a virtual image of the sample surface directly in front of the detection system, which allows only light coming from a specific surrounding of the mesa to enter the detection system. The PL is detected through a double monochromator (in subtractive mode) which supplies the required time-resolution connected with additional scattered light reduction. For time integrated measurements the signal can be detected by a standard photomultiplier tube (PMT) in connection with a single photon counting system (SPC) or with a charged coupled device camera (CCD, only setup figure 3.4 (b)) as a multi

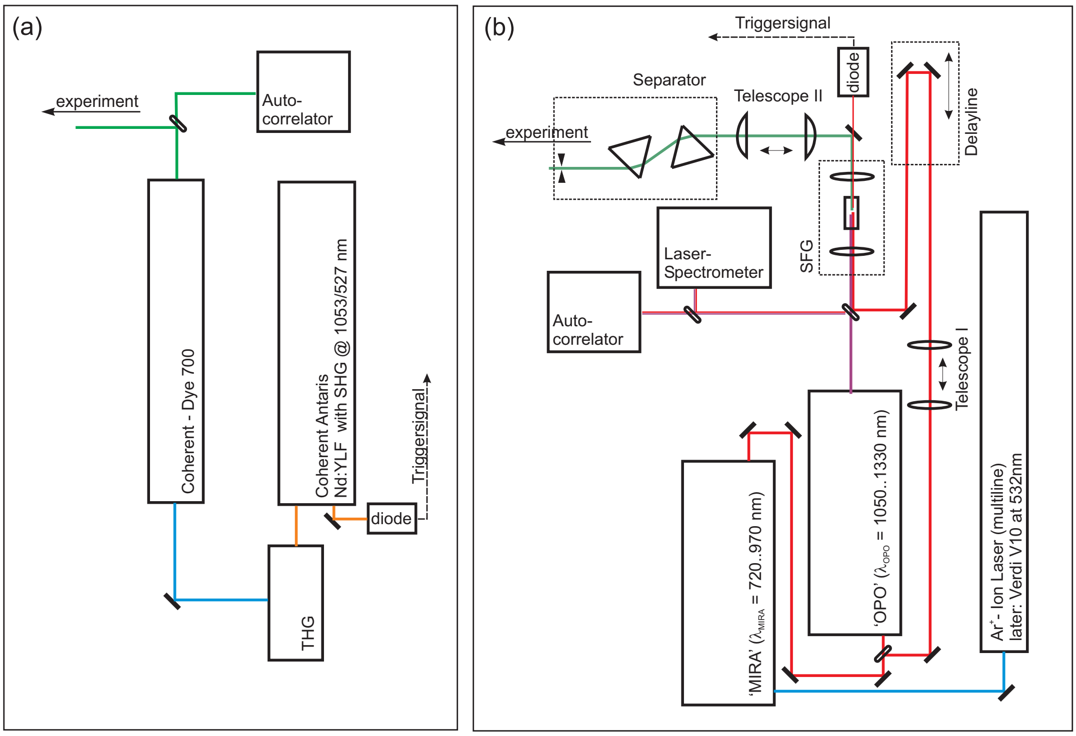

Figure 3.5: Setups for picosecond pulse generation: a.) Dye laser pumped by the third harmonic of an Nd:YLF laser. b.) System on the basis of a Ti:sapphire ps-oscillator with an optical parametric oscillator (OPO) followed by an sum frequency generation (SFG).

channel analyzer (MCA). For time resolved measurements a multi channel plate PMT (MCP-PMT) is used in connection with a time correlated photon counting system as discussed in the next section.

3.2.2 Time- and polarization resolved measurements

Nearly half of the experiments in this work are time- and polarization resolved. While the polarization resolution is achieved by the polarization optics in the μPL-setups sketched in Fig. 3.4 and discussed in the previous section, the overall time resolution is provided by two kinds of laser systems creating ps pulses in connection with a time resolved single photon counting system. All three subsystems will be discussed in what follows.

3.2.2.1 Generation of ps-laser pulses

Dye based laser system:
Since the beginning of this work a commercial picosecond dye laser system was available. The setup is shown in figure 3.5 (a). The central part is a Nd:YLF

laser[2] (Coherent Antaris) operating at $\lambda_{\mathrm{IR}} = 1053$ nm and creating pulses of 50 ps duration with a repetition period of 13 ns ($f = 76$ MHz). An internal second harmonics generation together with an external sum frequency generation[3] (THG) converts the pulses to the third harmonics wavelength of $\lambda_{\mathrm{THG}} = 351$ nm. These UV-pulses of 35 ps duration synchronously pump a Coherent 700 dye laser. The dye laser generates tunable pulses and the tunability is achieved by a three plate Lyot-filter inside the resonator. The laser operation spectral range ($\lambda_{\mathrm{Las}} < \lambda_{\mathrm{THG}}$) depends on the used dye solution. With dyes like Coumarin 102 and Stilbene 3, excitation resonant to the QDs and also excitation in the states of the wetting layer is possible. The pulse duration after the dye laser is about 1.5 ps. This system was used for the experiments on quantum coherence discussed in section 5.1.

Ti:sapphire based laser system:
For the other experiments in the time domain a more sophisticated pulse generation system was used, which connected smaller jittering in space and time with longer operation cycles and broader tunability. In addition, it has no background or sidebands in the surrounding of the operation wavelength so that also co-polarized excitation/detection configurations become possible. The setup is sketched in figure 3.5 (b). The system consist of a Titanium:sapphire ps-oscillator (Coherent 'MIRA' 900) operating in the range of $\lambda_{MIRA} = 720..970$ nm and driven by a diode pumped, frequency-doubled Nd:Vanadate laser (Coherent Verdi V10). The pulses of 1.8 ps duration and with a repetition rate of 76 MHz are partly used to pump an optical parametric oscillator ('OPO') which translates them into the longer wavelength range of $\lambda_{OPO} = 1050..1330$ nm. For resonant or non-resonant excitation of the used quantum dots higher excitation energies are necessary, realized by a frequency conversion from the infrared to the visible range. Therefore, a part of the MIRA-beam is coupled out before the OPO and used together with the OPO-beam for a sum-frequency generation (SFG) in a 10 mm long BBO (β-Bariumborat) crystal. For a proper conversion efficiency three criterions have to be fulfilled: 1.) The pulses of the two fundamental waves should be overlapped in space and time. 2.) They should be focussed for a minimized spot diameter which should be nearly constant over the whole crystal length. 3.) The phasematching condition (momentum conservation: $k_{OPO} + k_{MIRA} = k_{SFG}$ which leads to a specific angle between the beams and the optical axis of the crystal) is fulfilled. As seen in figure 3.5 (b) a telescope in the MIRA-beam is used to adjust the beam so that it has the same diameter and divergency at the position of the focussing lens of the SF-generator as the OPO-beam. In this way a maximum spatial overlap in the crystal between them is achieved. Furthermore, a delay line was used to overlap the pulses in time. Due to the properties of the BBO-crystal the outgoing SFG-beam is asymmetrically divergent, so that a spherical lens in

---

[2] The gain medium is a yttrium-lithium-fluorine crystal doped with neodymium atoms (Nd:YLF)

[3] The sum frequency generation between a fundamental wave and its second harmonic corresponds to a third harmonics generation.

connection with a cylinder lens telescope has to be used for collimation. Finally, the SFG-beam is spatially separated from the fundamental waves in a separator which consists of two dispersion prisms and a diaphragm. In this configuration it is possible to generate wavelengths between 430 and 530 nm with an equivalent CW power of $P \approx 10$ mW, making resonant and non-resonant excitation scenarios possible.

3.2.2.2 Time-resolved PL detection

The time resolution in the detection is achieved by the concept of time correlated single photon counting (TCSPC). In this concept the time between the detection event of a single photon and a reference pulse, derived from the pulsed excitation laser, is determined. Since this time can be only measured for the first detected photon resulting from an excitation event, this method yields only the correct time evolution of the PL signal if not more than one photon per excitation event reaches the detector. For time resolved measurements especially on single quantum dots the detection probability is usually between 10^{-6} and 10^{-4} photons per excitation event.

For detection a MCP-PMT can only be mounted on a double-monochromator in subtractive configuration[4]. In addition, a medium speed photodiode detects a part of the IR-beam coupled out of the ps-oscillator beam. So it generates a signal with exactly the same repetition rate as the pulses exciting the sample. Electronically the frequency of this signal is reduced by a factor of two yielding the reference frequency. This reduction results in two excitation events separated by the repetition period of the laser in one detection time window, which is given by the inverse reference frequency. The advantage of this modification is that the calibration of the timescale for the measured transients can be directly derived from the laser repetition period. Normally the calibration is created by measuring the apparatus function[5] of the system and identifying the distance of the two present laser transients with the laser repetition period of about 13 ns. Here the laser repetition period can be precisely determined using a frequency counter.

The electronic part of the setup, mainly consisting of a time to amplitude converter followed by an analog/digital converter, measures the time between one detection event at the MCP-PMT and a corresponding reference pulse. A computer counts the events appearing at the same time relative to the reference pulse. For an efficient number of events, the resulting histogram reflects the time evolution of the emission. The overall time resolution of this detection system is between 40 and 80 ps revealed by the measurement of the laser apparatus function.

---

[4] The subtractive configuration of two equal monochromators always provides the same transit time for photons entering the spectrometer in different incident angles or for photons with different energies.

[5] The apparatus function is measured by tuning the monochromator to the laser energy and measuring the transients of the laser. Two of them are present in one time trace, since for every reference pulse two excitation events appear.

3.2.3 Coherent control experimental techniques

As discussed in the introduction and in section 2.5 there are different ways to determine the optical dephasing time of a state or transition in a quantum system. One of them is the temporal coherent control which is used in this work. This technique, developed around the eighties, uses two short pulses with a variable coarse delay between them produced by an interferometer (see next section for detailed description). As discussed in section 2.5 each of these two pulses creates a subwave function which can interfere with each other if no dephasing occurs in between the delay time. The interference phase is related to the delay between the pulses. Variation of this delay results in oscillation of the interference signal with a period corresponding to the energy of the state which is controlled. This oscillation is modulated by an envelope function limited by the dephasing of the controlled state. The interference oscillations and dephasing are usually running on two different timescales. The oscillations are on the scale of the wavelength (500 nm $\hat{=}$ 0.6 fs) while the dephasing time is expected on a much longer time scale (i.e. ten to hundred picoseconds [10, 14]). There are several techniques to separate the fast oscillation from the slow varying envelope.

One of them is the *phase sensitive technique* [30, 31]. There an additional optical element (glass plate or movable mirror) inside the interferometer wobbles the phase between both pulses with a certain frequency. This frequency directly enters the interference signal and therefore, the amplitude of the signal can be extracted with a look-in amplifier. Unfortunately, this works well only for strong signal intensities yielding integration times shorter than the wobbling period.

Another frequently used method is the *phase locked technique* [66, 67, 68], where the delay between the two pulses can be selected on a short (fine delay time τ_F) and on a long (coarse delay time τ_C) timescale. By scanning step by step τ_F and gradually measuring the interference signal $I(\tau_F)$ the fast oscillations can be directly monitored. This technique was first applied to atomic [68] and molecular [66, 67] systems around 1990. Later this technique was used in the field of semiconductor quantum structures. It was applied in a series of experiments by *Heberle* and *Baumberg* [10] to coherent control of exciton properties in quantum wells like population, polarization and spin. Later, *Bonadeo et al.* [14] used this method to coherent control the population of the excited exciton in single semiconductor QDs, as already mentioned in the introduction.

The advantage of this method is in connection with single dot spectroscopy where the PL signal intensities are usually very small, that by this technique itself practically no limit for the integration time is given. The only demands are stability and reproducibility for the total delay $\tau = \tau_C + \tau_F$ on two timescales. First, during the integration time for a single point (τ_C, τ_F) the phase τ_F should be stable, otherwise the phase dependent intensity will not be correctly measured. Secondly, in order to measure an interferogram where the periodicity over τ_F of the phase dependent intensity is maintained, any combination $I(\tau_C = \text{const}, \tau_\text{F})$ should be precisely selectable for all measured points. This can be achieved using an active stabilization, as described in the next section.

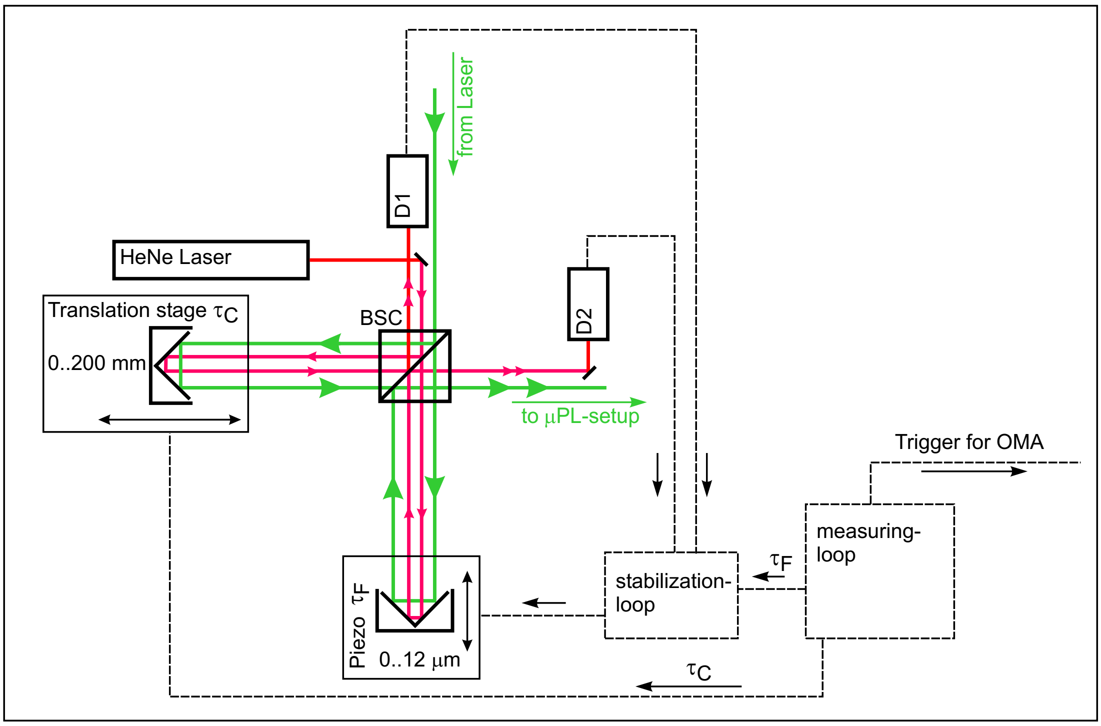

Figure 3.6: Optical layout of the actively stabilized Michelson-interferometer including a small information flowchart for the control- and stabilization-processes (dashed lines).

3.2.4 Actively stabilized interferometer

The general arrangement (see figure 3.6) is similar to that of the classical Michelson-interferometer. It provides two timescales for the delay between the two pulses, realized by an electrically powered mechanical translation stage (delay: 0..600 ps) on one arm for the coarse delay time τ_C and a Piezo (delay: 0..75 fs, resolution: 0.03 fs) on the other arm of the interferometer for the fine delay time τ_F. By varying the phase τ_F it is possible to resolve single interference fringes. The phase resolution is determined by the flatness of the optical elements used in the interferometer and the 'short term' phase stability (jittering) during the integration time for a single point in the interferogram. Typical integration times are between 10 and 30 s. Additionally, in order to measure interferograms which contain several interference fringes and where additional parameters as the coarse delay time τ_C or the excitation intensity are varied, a 'long term' stability of several hours is needed. While the short term stability can be partly achieved by well mechanical mounted optics the long term stability is only achievable with an active stabilization.

For active stabilization an additional HeNe CW-laser beam is passing the same optics in the interferometer as the working laser. The resulting interference is measured at both exits of the interferometer with two photodiodes ($D1$, $D2$). During an initialization routine the intensity distributions $D1_0(\tau_\mathrm{F})$ and $D2_0(\tau_\mathrm{F})$

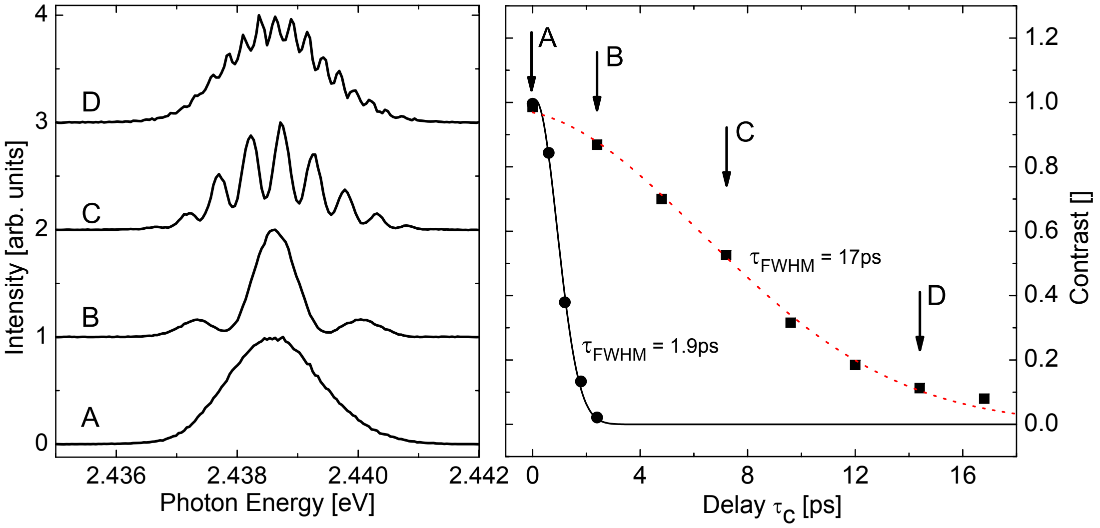

Figure 3.7: Spectra of two laser pulses for four different coarse delays τ_C and fixed τ_F between them (labelled as A,B,C,D in both panels). Corresponding decay of the interference contrast (right panel). The solid line indicates the autocorrelation function of the laser, where for the interferogram the total spectrum is integrated. The dashed line corresponds to an interferogram where only one tenth of spectral width of the laser is integrated (gaussian shaped).

are measured. These values are then used during the stabilized mode of the interferometer as 'target' intensities. In this mode a stabilization loop continuously compares the intensities $D1(\tau_\mathrm{F})$ and $D2(\tau_\mathrm{F})$ with the corresponding target intensities $D1_0(\tau_\mathrm{F})$ and $D2_0(\tau_\mathrm{F})$. The difference of both deviations is used to calculate a correction value, which is applied additionally to the piezo. This provides an overall stability of better than $\lambda/10$ (0.15 fs) for frequencies up to 30 Hz during typical measuring periods.

3.2.5 Acquisition of interferograms, test of the interferometer alignment

In the following, the technical way of interferogram acquisition is described. Special attention is put on the subsequent data processing, including possibilities of verification of the interferometer alignment given by additional data evaluation.

In order to measure an interferogram for different values τ_C a preselected number of fine delays τ_F is set by the control program. For each combination $(\tau_\mathrm{C}, \tau_\mathrm{F})$ a spectrum with the optical multichannel analyzer (OMA) is acquired. The use of an OMA for signal acquisition has the advantage to test the answer of several emission lines on the control pulses simultaneously. Furthermore, the use of a triple spectrometer where the two first stages are arranged in subtractive mode, together with a double split in between the first and the second stage, gives the possibility to measure the stokes and antistokes components simultaneously[6] at exactly the same τ_F while the scattered laser itself is blocked inside the spectrometer. This enables the later discussed two photon coherent control on biexcitons. Finally, in a data processing step, for all spectra, the range which contains the line under observation is integrated. This integrated value plotted over τ_F yield one interferogram for each τ_C and a specific line.

Paramount for the measurement of dephasing times is a proper align interferometer, providing both beams overlapped for all possible coarse delay times τ_C. The standard test for a cw laser is the measurement of the interference contrast of the laser itself and the verification that it is nearly 100% for all used coarse delay times τ_C[7]. To apply this method efficiently for pulsed lasers the duration of the pulses τ_P needs to be longer than the largest used coarse delay time τ_C. This is not the case here ($\tau_\mathrm{P} = 1.5$ ps < 30 ps $= \tau_\mathrm{C,max}$) and so spectral filtering of the laser is necessary in order to make the pulse efficient longer. This spectral filtering can be done before or after the interferometer. A spectral filtering in front of the interferometer with use of an additional prism or grating arrangement raises the problem of beam shifts resulting in inaccuracies of the alignment test. On the other hand, the applied setup offers a much easier possibility of realizing this spectral filtering with use of the spectrometer, exactly in the same configuration and alignment of the setup as in the real measurement. Only the spectrometer is tuned to the laser wavelength and several spectra of the laser for different combinations $(\tau_\mathrm{C}, \tau_\mathrm{F})$ are measured. In figure 3.7 (left panel) four laser spectra for different delays $(\tau_\mathrm{C} + \tau_\mathrm{F})$ are plotted. Numerical integration over the total laser line ($\Delta E_\mathrm{FWHM} \approx 1.8$ meV) and calculation of the interference contrast leads to the laser autocorrelation function in the right panel of the figure (solid line). It clearly demonstrates the laser autocorrelation length of about 1.9 ps.

Since the product $\Delta E_\mathrm{FWHM} \cdot \tau_\mathrm{FWHM}$ is constant, a spectral narrowing yields longer pulses. If one integrates only over the central part with 200μeV spectral width[8], as expected the contrast holds almost ten times longer (dashed line in figure 3.7). This indicates that the two beams leaving the interferometer are still correctly overlapped at coarse delay times τ_C one order larger than the pulse length. A loss of the interferometer alignment will result in a fast drop in the contrast function for the narrow range integrated interferogram of the laser.

3.2.6 Magnetic field dependent measurements

The used setup for measurements in magnetic field is sketched in figure 3.8. The sample is mounted in a split-coil cryostat (Oxford Spectromag 4000) capable of fields $0 \leq B \leq 12T$. The split-coil construction of the magnet allows switching between Faraday and Voigt geometry by rotating the magnet. An argon ion laser (Spectra Physics model 2085) is operated in single line mode at 488nm to excite

---

[6] The available spectral range is 40meV below and above the laser.

[7] For large delays τ_C it is necessary to take the coherence length of the used cw-laser into account.

[8] This is slightly above the spectral resolution in coherent control measurements of 180μeV.

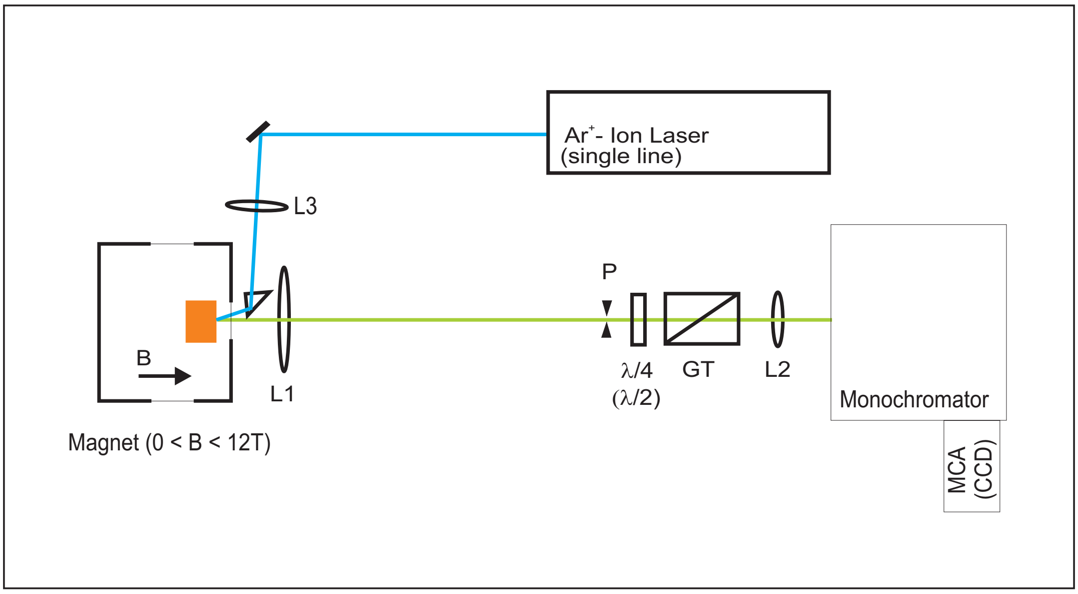

Figure 3.8: Experimental setup for magnetic field dependent measurements. The split-coil magnet can be rotated by 90° in order to switch between longitudinal (as in the figure) and transverse fields.

the sample nonresonant. In order to select the emission from a single mesa a conventional setup is used. The lens L1 gives a highly enlarged picture of the sample at the diaphragm P, where the emission of the mesa is selected and imaged via the lens L2 on the spectrometer slit. A half- or quarter-wavelength plate and a Glan-Thomson polarizer enable analysis of the emission for circular and linear polarization. The spectrometer itself provide a linear dispersion of 0.24 nm/mm, leading to a maximal resolution of 20 μeV [9]. A liquid nitrogen cooled CCD-matrix mounted to the spectrometer detects the signal for recording the time integrated spectra. The experiments were carried out in backward geometry with the propagation direction of incident and emitted light parallel to the [001] growth axis (z-axis) of the crystal.

---

[9] Depends on the used entrance slits

Chapter 4

Optical characterization of complexes in charged and uncharged QDs

As discussed in chapter 1 the used samples contain QDs with different orders of in-plane anisotropy. Furthermore, they can be charged with a resident electron, which fundamentally changes the properties of the QD. For the realization of the different experiments below, it is essential to know which kind of complex, either an exciton or a trion, is responsible for the emission under particular consideration.

In the following section different basic experimental methods will be discussed, which reveal specific properties of excitons (in uncharged QD) and trions (in charged QD), respectively. These methods will be networked to different characterization possibilities. Any emission line used needs to characterized by at least one of these possibilities in order to reveal if it is of excitonic or trionic nature.

4.1 PL emission from single QDs at zero magnetic fields

As discussed in chapter 2.1 the degree of symmetry of the three dimensional confinement, which is realized by a single QD, has strong influence on the optical properties of an exciton confined in this QD. By this reason, the first idea to distinguish between exciton and trions is to analyze their emission in the spectral domain. In figure 4.1 panel (a) the time integrated μPL spectra of different QDs are summarized, all taken from mesa structures below (150×150) nm^2 in size under non-resonant CW-excitation. By inspecting the different emission lines, one can divide the QDs into two groups:

The first group is demonstrated by the first three QDs labelled as QD#1, QD#2, and QD#3, where a clear identification of an exciton in an anisotropic QD is possible, since a splitting of the ground state is observable. The value

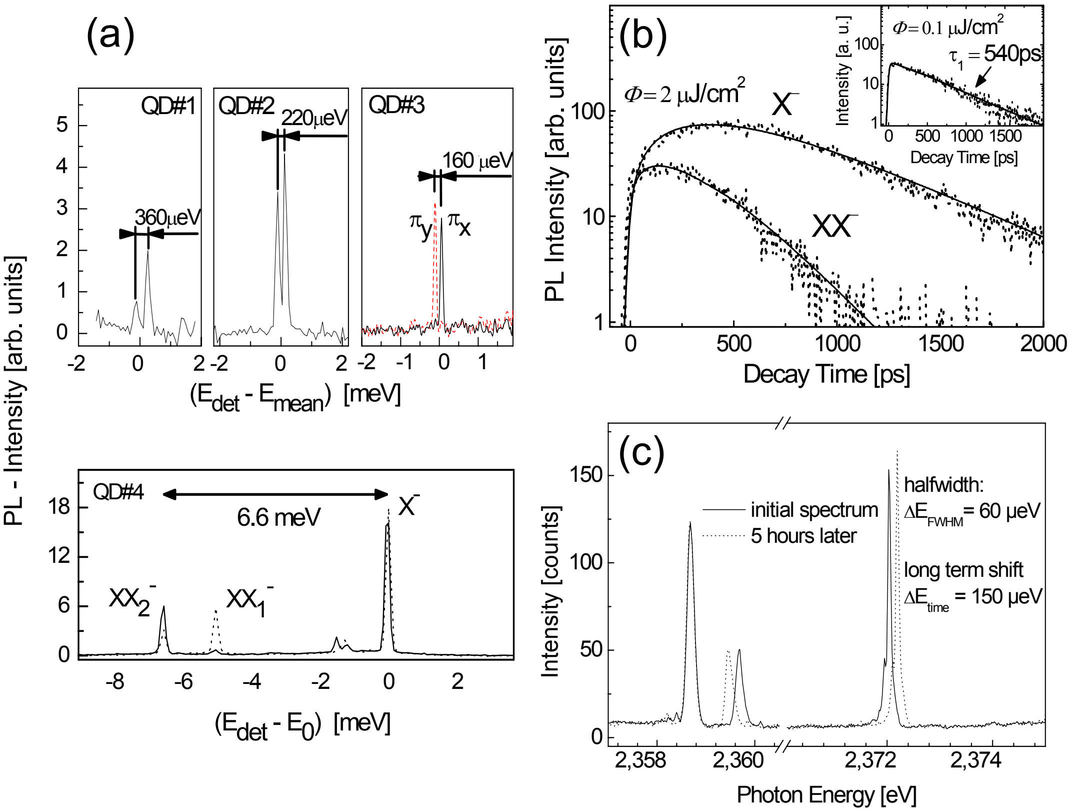

Figure 4.1: a) PL emission from different QDs under CW excitation above the wetting layer. b) Time transient for a trion and a charged biexciton. Inset: Transient of the same trion at low excitation power, where no charged biexciton is observed. c) Temporal stability of different emission lines.

of the splitting differs from dot to dot. An upper boundary for this splitting range can be evaluated from the observed splitting in the spectral domain, it was never larger than 450 μeV. As a lower boundary, the quantum beats discussed in chapter 2.1 yielding values of the order of 10 μeV already not resolvable in the spectral domain.

The two components are linearly cross polarized to each other, directly manifested by the plot of QD#3 which is done for two cross aligned polarizations. The labels π_x and π_y correspond to linear polarized detection along the [110] and $[1\bar{1}0]$ crystal axes respectively. However, as recent polarization resolved experiments uncovered, there are also QDs where the main axes of in-plane anisotropy do not coincide with the above crystal axes [69]. All the emission lines for QD#1 to QD#3 grow linear with excitation power, which manifests that they are excited by a single photon absorption process. As discussed in section 2.1 the splitting of the ground state is due to electron-hole exchange interaction in an anisotropic QD and its observation proves directly the excitonic nature of these lines.

However, if instead of such a line doublet a single emission line is observed (isotropic QD) additional information is necessary. Such information can be extracted from the emission spectrum at high excitation powers. If the excitation power is sufficiently high so that multi excitonic effects come into play (i.e. more than one electron hole pair in the QD) then the resulting spectrum for charged and uncharged QDs is different.

For the case of an uncharged QD, in addition to the excitonic emission line a second line below should appear which is separated by the biexciton binding energy of about 22 meV and grows quadratic with excitation power [70]. This fact alone does not prove exactly that both of these lines are coming from the same QD[1] and so the biexciton emission can not proof that the isotropic QD is uncharged. This situation is different for an anisotropic QD as it will be discussed in section 5.3.2.

In case of a charged QD the situation is different as it is demonstrated by the trion emission for QD#4 which represents the second group of QDs. The spectrum of a trion shows three characteristic features. First, in accordance with the discussion in section 2.2 and in contrast to the above excitons, there is a sharp unpolarized line without any resolvable splitting[2]. Secondly, there are two lines labelled with XX_1^- and XX_2^- in the figure. These lines are always separated from each other by an energy in the range of (1.6 ± 0.1) and appear 5..9 meV below the X^- line. While the X^- line shows a linear dependence on the excitation power, the lines XX_1^- and XX_2^- grow nearly quadratic with low excitation power. The latter is a characteristic sign that two photons are absorbed and so at least two electron hole pairs should be involved in the corresponding state behind the emission lines XX_1^- and XX_2^-. In addition, in figure 4.1 panel (b) time resolved PL data is summarized. Under weak excitation ($\Phi = 0.1 \mu J/cm^2$), when the lines XX_1^- and XX_2^- are absent, the emission of the line X^- obeys a single exponential decay with a lifetime of $T_1 = 540$ ps as indicated in the inset. However, if the excitation power is risen so that the lines XX_1^- and XX_2^- appear simultaneously ($\Phi = 2 \mu J/cm^2$ in the figure), the X^- line shows a double exponential behavior with an rise time of 280 ps and a decay time of 540 ps. The lines XX_1^- and XX_2^- decay single exponentially with one time constant of 250 ps. The PL transients, as well as the power dependence manifests clearly that the lines XX_1^- and XX_2^- are due to recombination of charged biexcitons in connection with the trion line labelled with X^-.

The spectrum of QD#4 is characteristic for a charged QD. However, analysis is based on a clear identification of the three lines (XX_1^-,XX_2^- and X^-) which can be difficult if a larger number of QDs is on the mesa. Additionally, it is in general necessary to proof experimentally that the line which is presumable a trion is not split. The latter can not be fulfilled since the splitting of the exciton ground state can be smaller than the best available resolution of 20 μeV. This means that if the spectrum of a QD is not as clear as for QD#4 additional experiments should be performed to check if the dot is charged or not.

This leads to the main conclusion of this analysis, that from the above dis-

---

[1] This prove is important, since even at a small mesa several QDs give a contribution to the spectrum.

[2] Proofed down to 20μeV best available spectral resolution

cussed spectral data one can only get a first hint of the origin of the emission lines and additional information to distinguish between the different groups is necessary. This will be provided by magnetic field data presented in the next section. But before this is done a short discussion of the spectral stability of the single QD emission will appear.

The spectral stability of the QD emission lines is an important property in connection with the main experiments in this work, which require long integration times or measuring series. Emission lines from single QD often show a spectral drift in time. Three such QD emission lines are summarized in figure 4.1 panel (c). They are measured two times with 5 hours in between detection. Some lines are ultra stable and show no spectral drift even if they are excited over several hours. Other lines show a spectral drift of several 100 μeV in some hours while exciting them up to the saturation limit. Sometimes lines also shift much more strongly. The last one was often connected with an excitation power which saturates the QD. Finally, it does not become clear if the high excitation power causes the strong shift of the QD emission, since other dots remain stable under comparable excitation conditions. In general, no blinking effects are observed on the dots used here as discussed in [71, 72, 73]. Since spectral stability is paramount for the following experiments only QD with a high stability are used, where this spectral line drift is not observed during typical measuring periods. The stable QDs used are selected during the exciton/trion identification experiments described in this section.

4.2 Single QDs in external magnetic field

Transverse magnetic fields, Voigt geometry

The most powerful tool which provides information in addition to the preceding section for distinction between excitons and trions is the analysis of their behavior in an external magnetic field applied perpendicularly to the main quantization axis (transverse magnetic field). In figure 4.2 the emission from a trion (a) and an exciton (b) is summarized for three different field strengths. One can see that the single emission line of a trion at $B = 0$ splits into four components at fields $B \neq 0$ with growing distances if the magnetic field becomes larger. In contrast, the exciton emission consists already at $B = 0$ of two components and for stronger magnetic fields these two components shift to higher energies while keeping their distance equal.

Beginning with the discussion of the behavior of the trion, in accordance with section 2.2.1, it is clearly manifested by the four components in figure 4.2 that in transverse magnetic fields the projections of J_{hh} and S_{e} in z-direction are no longer good quantum numbers. Consequently, with the new eigenfunctions of the form $1/\sqrt{2}\,(|+a\rangle \pm |-a\rangle)$ where a is 3/2 for the trion singlet state (initial state) and 1/2 for the single electron state (final state), all four possible transitions become optically allowed. The energy positions of the four components are connected

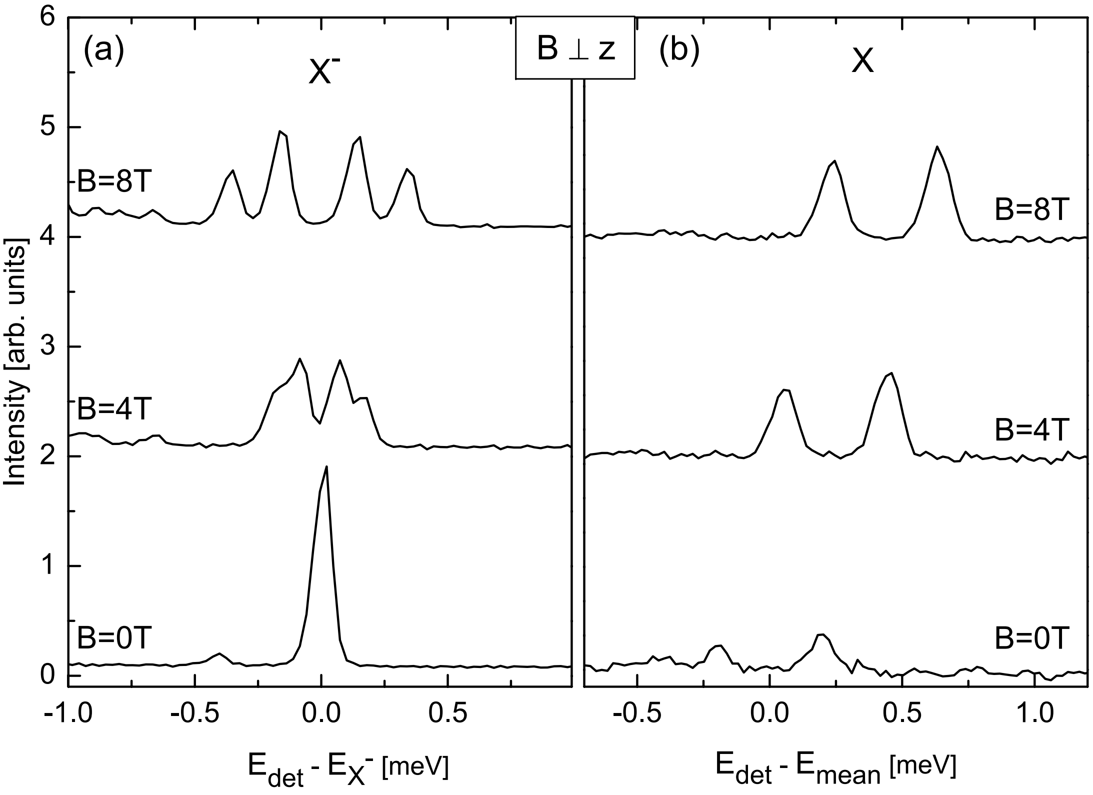

Figure 4.2: Trion (a) and exciton (b) in transverse magnetic field.

with the in-plane g-factors for electron $g_{\mathrm{e},\perp}$ and heavy-hole $g_{\mathrm{hh},\perp}$ in accordance with the equations in table 2.16. By careful evaluation of the energies one can determine these g-factors which is done below. An extrapolation of the energy positions to $B = 0$ yields that all four transitions there have the same transition energies corresponding to the single emission line visible for $B = 0$.

For the exciton the situation is different. There the bright and dark states at $B = 0$ are separated by the zero field splitting of about $\Delta_0 \approx 1.9$ meV [58]. As discussed in section 2.1, a transverse magnetic field mixes the bright and dark exciton states, so that in general four different transitions become possible and consequently four emission lines can be observed. However this occurs only if the magnetic field is so strong that it creates an energy contribution larger than the electron hole exchange interaction. The two visible components in figure 4.2 (b) for $B = 0$ arise from the bright states. The separation of about $\Delta_1 \approx 400\mu$eV manifests that the exciton is located in a QD with in-plane anisotropy. The magnetic field dependent energy of the two bright states is given in accordance with section 2.1 by:

$$E_{1,2} = E_0 + E_{1,2}^{\mathrm{dia}} + \frac{1}{4}\left[\pm(\Delta_1 + \Delta_2) + \sqrt{(2\Delta_0 \pm \Delta_1 \mp \Delta_2)^2 + 4\left(g_{\mathrm{e,x}} \mp g_{\mathrm{h,x}}\right)^2 \mu_{\mathrm{B}}^2 B^2}\right] \tag{4.1}$$

where $E_{1,2}^{\mathrm{dia}}$ takes the diamagnetic shift into account. The equation illustrates that the Zeeman effect is small for the applied magnetic field strengths ($B <$

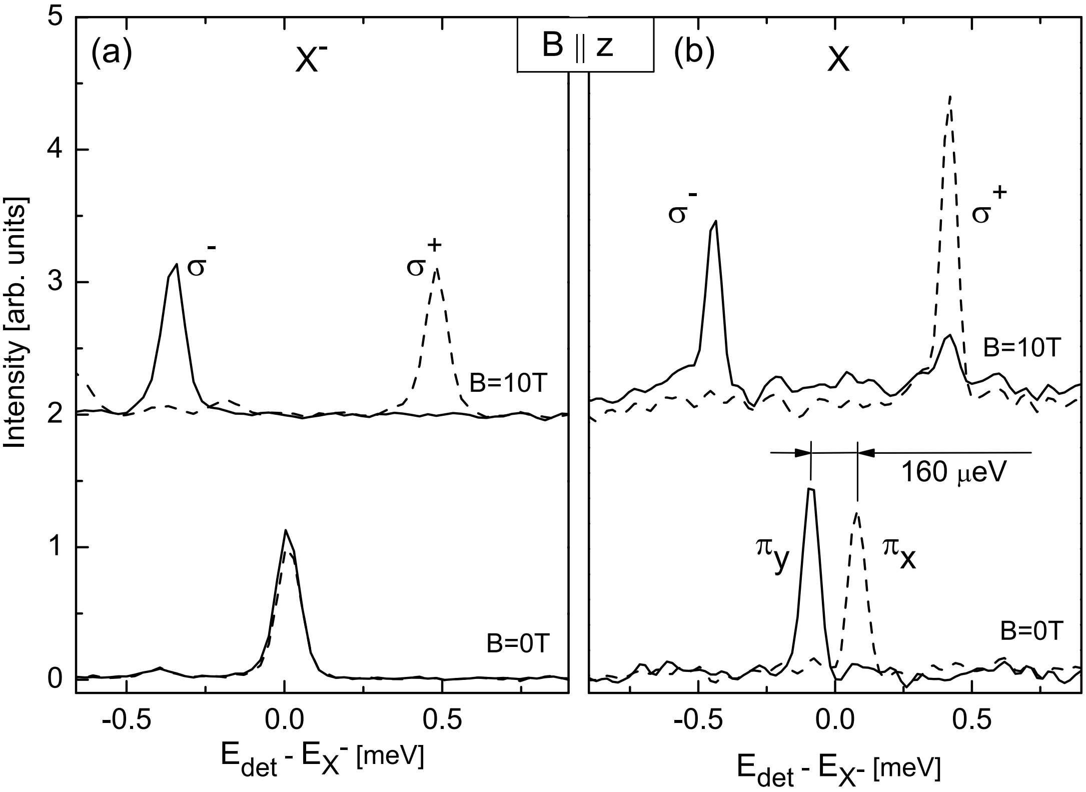

Figure 4.3: QDs in longitudinal magnetic field: a.) Circular polarization resolved trion emission for zero and non-zero fields. b.) Linear polarization resolved emission from a QD with in-plane anisotropy for zero field and circular polarization resolved for non-zero field (π_x and π_y corresponds to the [110] and [1$\bar{1}$0] crystal axes respectively).

8T) using the later determined g-factors $g_{\mathrm{e,x}} \approx 1.08$ and $g_{\mathrm{hh,x}} \leq 0.4$. With use of the above given values for Δ_0 and Δ_1 and assuming that Δ_2 is small compared to them, a value for the first term in the square root for $E_1(E_2)$ of 18(12)meV^2 can be estimated. On the other hand, the second term yields at 8T values of 0.55(1.7)meV^2. This means that the Zeeman term is at least one order of magnitude smaller than the first term, which describes the electron-hole exchange contribution. The shift in figure 4.2 (b) is then mostly provided by the diamagnetic shift acting the same on both emission lines, which explains that the energy separation of both components remains the same for the different field strengths at approximately Δ_1.

In conclusion, the different characteristic behavior of the trion and the exciton in transverse magnetic fields provides a sufficient tool for trion and exciton identification.

Longitudinal magnetic fields, Faraday geometry

The behavior of a trion and of an exciton in longitudinal magnetic fields (Faraday geometry) is demonstrated in figure 4.3 (a) and (b), respectively. As discussed in chapter 2, under longitudinal magnetic fields the z-projections of J and S are still good quantum numbers. Consequently, for a trion as well as for the exciton only two emission lines can be observed. The spectra in figure 4.3 are polarization resolved. In case of a trion, one can see an unpolarized line for $B = 0$ corresponding to the two transitions $|\pm 3/2\rangle \rightarrow |\pm 1/2\rangle$, where both initial and final states are degenerated. For non-zero magnetic fields the degeneration of the final and the initial state is lifted. The resulting total splitting between both optically allowed transitions is defined by equation 2.14 as $\Delta E = \mu_{\mathrm{B}}\left(g_{\mathrm{h,z}} - g_{\mathrm{e,z}}\right) B_{\mathrm{z}}$. This equation is used below in connection with a more careful data analysis to determine the g-factor difference $g_{\mathrm{h,z}} - g_{\mathrm{e,z}}$. While at zero magnetic fields the single emission line is unpolarized, in case of non-zero fields one can clearly see that due to momentum conservation the emission from the two transitions is oppositely circularly polarized.

The exciton in panel (b) is again one in a QD with in-plane anisotropy. One can clearly see the splitting of the ground state in two linearly cross polarized components indicating that Δ_1 in the matrix 2.8 is non-zero. For the QD in the figure it has a value of $\Delta_1 = 160\mu\mathrm{eV}$. If a longitudinal magnetic field is applied the polarization of the two components change to circular. This suggests that the symmetry of the dot is only moderately broken, so that $\beta_1 = \mu_{\mathrm{B}}\left(g_{\mathrm{e,z}} + g_{\mathrm{h,z}}\right) B_{\mathrm{z}}$ is larger than Δ_1 and the symmetry can be easily restored by the used magnetic fields. In this case the mixed eigenfunctions for $B = 0$ of $1/\sqrt{2}\left(|+1\rangle \pm |-1\rangle\right)$ change in good approximation into $|\pm 1\rangle$ as in a symmetric QD.

In summary this kind of experiment is only able to prove that two emission lines closely adjacent in energy originate from the same anisotropic QD. The longitudinal magnetic field dependence of an exciton and a trion provides no possibility for distinction between both, since especially in case of a QD with small in-plane anisotropy where no splitting of the ground state is observed ($\Delta_1 \approx 0$) the spectral behavior is not different.

Determination of g-factors from the trion emission

Trion PL data like presented in the figures 4.2 and 4.3 can be further evaluated in order to determine the g-factors for electron and hole, which will be needed for the discussion of the results in section 5.2.1. In order to do this, the energy positions for the different emission lines of a typical trion are plotted versus the magnetic field strength for both geometries in figure 4.4. In both of the figures the diamagnetic shift is corrected. As discussed in section 2.2.1 from the longitudinal magnetic field data (panel a) only the difference of the g-factors in z-direction can be determined. The solid lines in figure 4.4 (a) correspond to a fit of the data with equation 2.14 and yields a g-factor difference of:

$$\left(g_{\mathrm{h,z}} - g_{\mathrm{e,z}}\right) = (1.54 \pm 0.08) \tag{4.2}$$

In panel (b) where the transverse magnetic field data is summarized in the same way as the longitudinal one in panel (a), the situation is - as expected - different.

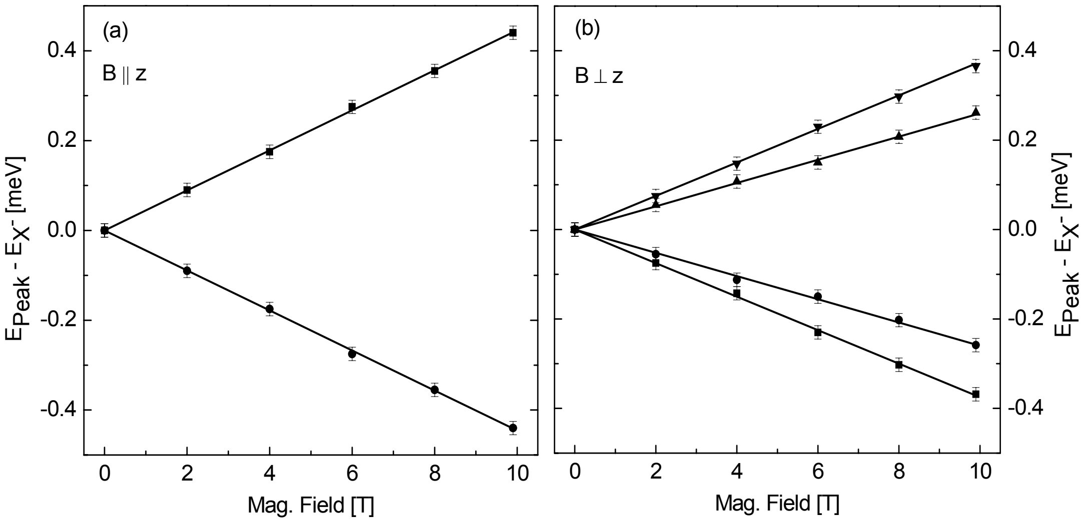

Figure 4.4: Determination of the electron and hole g-factors from typical trion PL data: energy positions of the different components versus longitudinal (a) and transverse (b) magnetic field.

Due to the transverse magnetic field the z-projections of J and S are not good quantum numbers, so that all possible transitions become optically allowed. In this case, the g-factors for electron and hole become independently accessible. The solid lines in the figure represent fits in accordance with the equations in table 2.16 and one can extract the in-plane g-factors for electron and hole as:

$$g_{\mathrm{e,x}} = (1.10 \pm 0.03) \qquad g_{\mathrm{h,x}} = (0.20 \pm 0.03) \tag{4.3}$$

This evaluation was done for several trions. The electron g-factor for these trions was always about 1.1 ± 0.1. The in-plane g-factor for the hole differs more strongly from dot to dot. The largest one was found to be $g_{\mathrm{h,x}} = 0.44$, which suggests different in-plane extensions of the QDs. While the electron g-factor is in good approximation isotropic [74], this is not the case for the hole g-factor. Using the above determined difference $(g_{\mathrm{h,z}} - g_{\mathrm{e,z}}) = 1.54$ and the assumption of an isotropic electron g-factor $g_{\mathrm{e,z}} \approx g_{\mathrm{e,x}} = 1.1$, yields a heavy hole g-factor in z-direction of $g_{\mathrm{h,z}} = 2.6$.

The strong anisotropy of g_{h} is a consequence of the properties of J and J^3 and can be understood by inspection of the hamiltonian 2.11. There it can be seen that since J_{x} has no diagonal elements the in-plane energy splitting can only be due to the cubic hole Zeeman interaction term proportional to q. This yields the definitions already discussed in section 2.1.1 of the hole g-factors $g_{\mathrm{h,z}} = 6\left(\kappa_{\mathrm{z}} + \frac{9}{4}q_{\mathrm{z}}\right)$ and $g_{\mathrm{h,x}} = 3q$ and since it is $q \ll \kappa$ [74] it follows $g_{\mathrm{h,z}} > g_{\mathrm{h,x}}$, which is in agreement with the above findings.

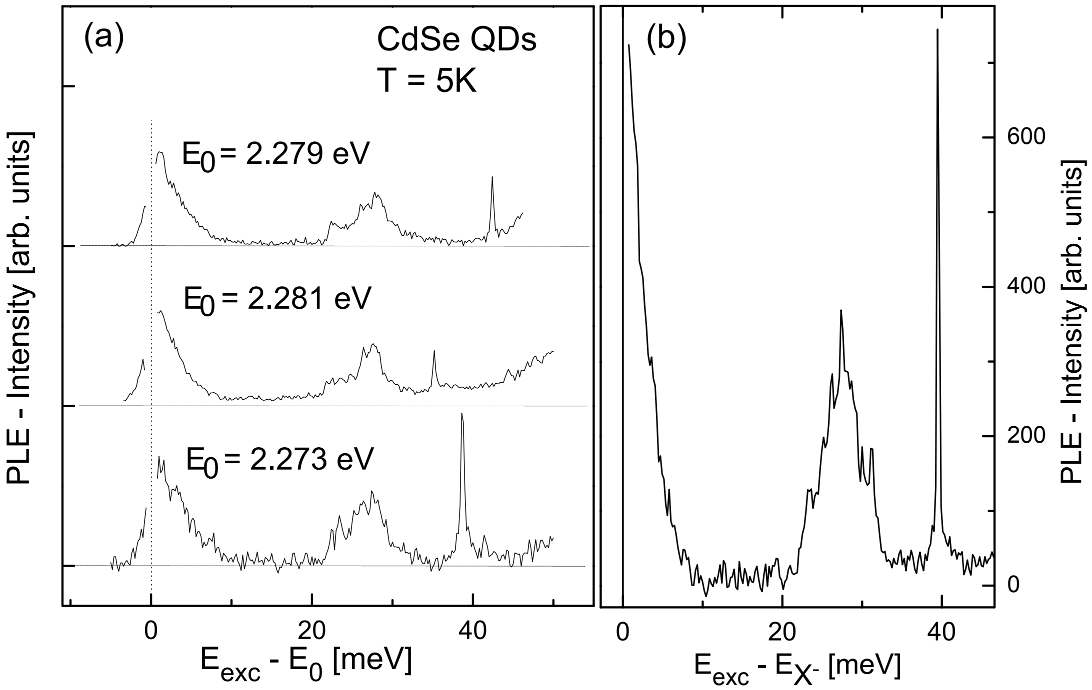

Figure 4.5: PLE spectra for excitons (a) and trions (b).

4.3 PL excitation spectra

In the following section, the energy structure of electron-hole complexes in QD will be discussed by means of photoluminescence excitation spectra (PLE), in order to uncover possible excitation energies for quasi resonant excitation.

In figure 4.5 PLE of four different QDs are presented. The energy of the ground state from which the emission is observed is different for all of the used QDs. The used mesa structures are below 150 nm in diameter, providing a sufficient separation of the QD emission lines. This is also proved by the fact that the PLE spectra in figure 4.5 are free of background, ensuring that signals from QDs other than the selected one are not involved. Furthermore, additional PL measurements uncovered that the emission lines under observation are independent in its energy position of the excitation energy. The three emission lines under investigation in figure 4.5 panel (a) are from uncharged QDs, while the emission line in panel (b) was clearly identified as a trion from a charged QD.

Independent of its origin, all PLE spectra measured on the different QDs show three characteristic features in the displayed energy range (up to 50 meV above the ground state). First there is a sharp peak ($\Delta_{\mathrm{FWHM}} \approx 0.5$ meV) on the high energy side, associated with the first excited optically allowed state $|X_1\rangle$. While its overall position is consistent with the size of the QD, fluctuations from dot to dot in the separation energy $E_1 - E_0$ of 35..45 meV indicate a complex dependence of the excited state energy E_1 on the size, shape and in general also the composition of the particular QD.

In addition, there are two broad bands. One in direct proximity of the ground state energy E_0 and the other 25 to 30 meV above, with practically no variation of their relative position in respect to the ground state. Both features are due to phonons. The one which is close to E_0 is due to acoustic and the other one is due to optical phonons. Especially the second phonon replica has a complex shape, which is slightly different from dot to dot. This shape and the surprisingly large width suggests that different types of LO-phonons are involved. Inspecting the LO-phonon band yields that at least three LO-phonon types should be involved. Since the wavefunction is not totally confined in the QD also phonons which have their origin in the wetting layer or the ZnSe buffer layer can provide a contribution [64]. In particular it can be the ZnSe LO-phonon ($\hbar\omega_{\mathrm{LO,bulk}}^{\mathrm{ZnSe}} = 28$ meV) and the CdSe LO-phonon ($\hbar\omega_{\mathrm{LO,bulk}}^{\mathrm{CdSe}} = 26.3$ meV) which can explain the subbands at 28 meV and (26 ± 1.5) meV. There are two possible explanations for the subband at 23.5 meV. On the first hand one knows that the wetting layer is under a certain stress. This stress leads to a splitting in the phonon modes in singlet and doublet modes with a splitting of about 3 meV [64]. In this case, both of the subbands (at 23.5 meV as well as at 26 meV) can be accounted to phonons in the CdSe wetting layer. On the other hand, also the QDs can give a contribution to the phonon spectrum. As one knows, QDs can show surface phonon modes (SO-phonons), which have an energy in between the LO- and the transverse optical (TO) phonon energy of the corresponding bulk semiconductor. Such phonon spectra are observed for self-assembled *GaAs/(In,Ga)As* QDs by Farfad et al. and Heitz et al. and not fully understood yet [75, 76]. But, a further discussion is out of the scope of this work and so the reader is directed to the actual literature if further progress is made in the future.

In conclusion, the PLE spectra in the discussed energy range provides no information for the distinction between exciton and trion. Both types of electron-hole complexes can be generated by LO-phonon assisted excitation or excitation in the first excited state which is situated in both cases 35..45 meV above the ground state.

4.4 Summary about experimental characterization tools

In conclusion of this section there are three different methods usable to identify the nature of a specific line under observation:

- In transverse magnetic fields the trion splits up into four components already at moderate fields. Extrapolating all four components to $B = 0$ all line will coincide in the same energy. On the other hand, one finds in the same way for an exciton, that the bright and dark states are separated by a zero field splitting of about 1.9 meV. Furthermore, for an exciton much stronger fields compared to the trion are necessary to lift the degeneracy of the two bright (dark) states in an isotropic QD or change the energy separation of them in a QD with stronger in-plane anisotropy, so that clearly four lines can be observed.

- Using a spectrometer with sufficiently high resolution, one can search for the doublet of a ground state exciton in a QD with in-plane anisotropy. The two components found have to be linearly cross polarized to each other. Additionally, one can check if these two components become oppositely circular polarized in longitudinal magnetic field.

- Inspection of the PL-spectra for different excitation powers and checking if biexcitonic (in case of exciton) or charged-biexcitonic (in case of trion) emission lines become visible. These lines can be identified by their energy positions and super-linear excitation power dependence. In case of a trion, the charged biexciton emission lines appear 5..10 meV below the single trion emission line. For an exciton the biexciton emission is below the exciton emission separated by the biexciton binding energy of 22 meV. Especially in case of an anisotropic QD the exciton as well as biexciton emission consist of a line doublet with the same energy splitting where the two components are oppositely linearly cross polarized to each other. This method is only convincing if the spectral density of all emission lines from the mesa is so small that the lines from exciton and biexciton (trion and charged biexciton) can be clearly attributed to the same QD.

Chapter 5

Coherence and spin-memory in QDs

5.1 Quantum coherence of excitons

In the previous chapter it was demonstrated that in an anisotropic QD the electron-hole exchange interaction leads to a splitting of the ground state exciton. This energy doublet of the $|X_0\rangle$ exciton is radiatively coupled to the crystal ground state and represents a V-type system, where quantum beats in the spontaneous emission may occur if the phase between these two substates is maintained during the lifetime [77]. So the beats associated with single-photon interference carry direct information about the coherence of the electronic states behind the emission. Previous observations of quantum beats in semiconductors were connected with the additional application of an external magnetic field, since they were based on the Zeeman-splitting of the exciton spin states [11, 13, 78].

The experiment presented here operates without external magnetic fields. In figure 5.1 the energy structure is schematized. The two substates $|x\rangle$ and $|y\rangle$, which are used as the upper states of the V-system, represent different spin states of the ground state exciton $|X\rangle$ in accordance with the discussion in section 2.1. Since a beating between these two spin states tells that the phase between them is maintained, such a quantum beat experiment provides information about the transverse spin relaxation time. In order to observe a clear beating every excitation shoot of the laser should prepare the states $|x\rangle$ and $|y\rangle$ with the same initial phase relation. To achieve this, the excitation was chosen quasi-resonant one LO-phonon above the ground state as indicated in figure 5.1 (a). If the laser is energetically so close to the detection energy, the used time resolved detection system has strong stray light problems. To reduce the scattered light, the detection polarization is always crossed to the excitation polarization. Furthermore, the two states $|x\rangle$ and $|y\rangle$ are cross polarized to each other. So, quantum beats as a result of interference between the two states can be only observed by projecting both polarizations on a common axis before detection.

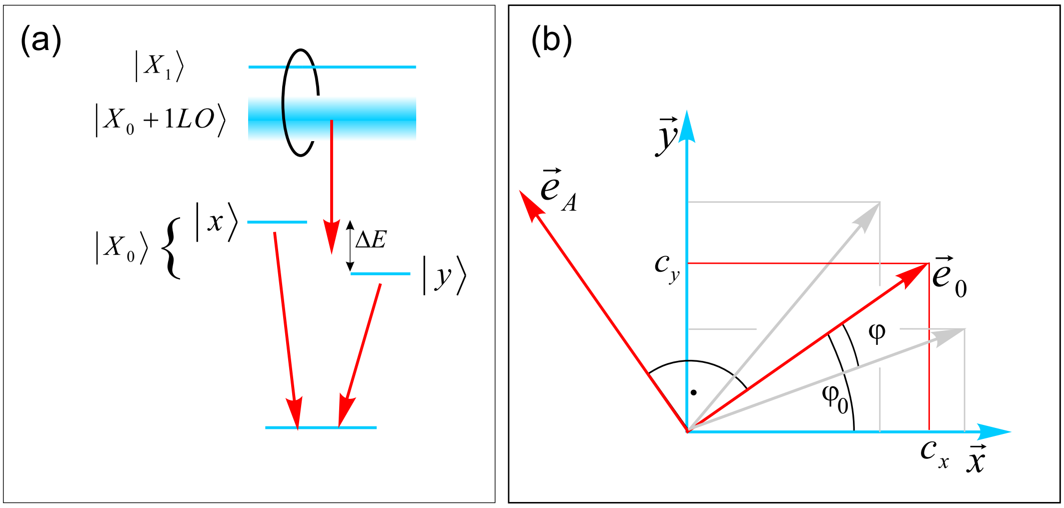

Figure 5.1: (a) Energy scheme of the quantum beat experiment and (b) the geometrical situation. The polarization of the excitation $\vec{e}_0$ is fixed cross polarized to the detection polarization $\vec{e}_\mathrm{A}$. Both are rotated by φ_0 against the fundamental QD axes $|x\rangle$ and $|y\rangle$. The gray arrows illustrate the fuzzy preparation of c_x and c_y.

This suggests the schematized geometry in figure 5.1 (b) for the polarization situation in the experiment. Two cross aligned polarizers for excitation ($\vec{e}_0$) and detection ($\vec{e}_\mathrm{A}$) can be tuned with a variable angle φ_0 to the fundamental quantum dot axes oriented along $[1,1,0]$ and $[1,\bar{1},0]$, and denoted by $\vec{x}$ and $\vec{y}$ in the figure 5.1 (b). If linearly polarized excitation pulses are applied, the projection will always lead to the same coefficients c_x and c_y and a 'pure' initial state is prepared, which in accordance with equation 2.29 reads as:

$$\Psi\left(t=0\right) = c_\mathrm{x}\left|x\right\rangle + c_\mathrm{y}\left|y\right\rangle . \tag{5.1}$$

As discussed above, due to necessary stray light reduction, the excitation is not strictly resonant to the states $|x\rangle$ and $|y\rangle$. The polarization is slightly randomized during the relaxation from the excitation in the LO-phonon replica into the exciton ground state. This leads to not sharp defined c_x and c_y (i.e. they are different for every excitation shoot) and the prepared state $\Psi\left(0\right)$ becomes 'fuzzy'. This situation is sketched in figure 5.1 (b) by the additional gray arrows. Since the total signal is given by the integration over about 10^{11} excitation shoots this 'fuzzy' preparation enters the consideration by the mean values $\langle c_\mathrm{x}^2\rangle$, $\left\langle c_\mathrm{y}^2\right\rangle$ and $\langle c_\mathrm{x}^* c_\mathrm{y}\rangle$, where the last term carries the degree of coherence for the two substates $|x\rangle$ and $|y\rangle$.

The expected far field signal at the detector in the assumption of purely radiative damping (Weisskopf-Wigner approximation) reads as [77]:

$$\begin{aligned} I\left(t\right) &\propto \left\langle \Psi\left(t\right) \left| \left[\vec{e}_\mathrm{A}\vec{E}^{(-)}\left(t\right)\right] \left[\vec{e}_\mathrm{A}\vec{E}^{(+)}\left(t\right)\right] \right| \Psi\left(t\right) \right\rangle \\ &\propto \left\langle \left| \left(\vec{e}_\mathrm{A}\vec{x}\right) c_\mathrm{x} e^{-i\omega_\mathrm{x}\mathrm{t}} + \left(\vec{e}_\mathrm{A}\vec{y}\right) c_\mathrm{y} e^{-i\omega_\mathrm{y}\mathrm{t}} \right|^2 \right\rangle \cdot e^{-\Gamma \mathrm{t}} . \end{aligned} \tag{5.2}$$

The two terms in equation 5.2 represent the components x and y, where the round brackets give the projection on a common axis. Moreover it is assumed that both substates are decaying in time with the same rate Γ. Using the abbreviations $x = sin\left(\varphi_0\right)$ and $y = cos\left(\varphi_0\right)$ and defining $c_{\mathrm{x}} = \cos\left(\varphi_0 + \varphi\right)$ and $c_{\mathrm{y}} = \sin\left(\varphi_0 + \varphi\right)$ one can rewrite equation 5.2 as:

$$I\left(t\right) \propto \left(A + B \cdot cos\left(\Delta\omega_{\mathrm{ex}} t\right)\right) \cdot e^{-\Gamma \mathrm{t}} \tag{5.3}$$

where

$$\begin{aligned} A &= 2x^2y^2 + \left(x^2 - y^2\right)^2 u - xy\left(x^2 - y^2\right) v && (5.4)\\ B &= 2x^2y^2\left(2u - 1\right) + xy\left(x^2 - y^2\right) v, && (5.5) \end{aligned}$$

with the two statistical parameters,

$$\begin{aligned} u &= \int_0^{2\pi} d\varphi\, P\left(\varphi\right) \sin^2\left(\varphi\right), \\ v &= 2\int_0^{2\pi} d\varphi\, P\left(\varphi\right) \sin\left(\varphi\right) \cos\left(\varphi\right) && (5.6) \end{aligned}$$

where $P\left(\varphi\right)$ is the angular distribution - measured relative to $\vec{e}_0$ - established during relaxation, which is normalized as $\int_0^{2\pi} P\left(\varphi\right) d\varphi = 1$.

Before equation 5.3 is compared with the experimental results the meaning of the two statistical parameters u and v in connection with the angular distribution $P\left(\phi\right)$ will be discussed.

Inspecting the equations 5.3 to 5.6 yields that the angular distribution $P\left(\varphi\right)$ can influence the beating strongly. One special case is $P\left(\varphi\right) = const$ where the polarization is totally washed out, so that $u = 1/2$ and $v = 0$. This yields $B = 0$ and no beatings can occur independently from φ_0. The second example is if $P\left(\varphi\right)$ can be described by a δ-function. Here the beating amplitude changes strongly with φ_0. By this reason, only the extreme value of $\varphi_0 = \pi/2$ will be considered. In case of $P\left(\varphi\right) = \delta\left(\varphi = 0\right)$ it yields $u = 0$, $v = 0$ and $A = -B$ so that the beating starts at $t = 0$ with a minimum. In case of $P\left(\varphi\right) = \delta\left(\varphi = \pi/2\right)$ it is $u = 1$, $v = 0$ and the beating has at $t = 0$ a maximum. This behavior can be generalized: If $P\left(\varphi\right)$ is distributed mainly close to $\varphi = 0$ it yields $u < 1/2$, $B < 0$ and the beatings start with a minimum. If $P\left(\varphi\right)$ is more located above $\pi/4$, u becomes larger than $1/2$ so that $B > 0$ and a beating maximum is observed at $t = 0$.

In figure 5.2 (a) it is illustrated how the randomization of the polarization expressed by the shape of $P\left(\varphi\right)$ influences the intensity at the detector. In case of a pure preparation ($P\left(\varphi\right)$ is a delta function) the oscillations go down to the baseline demonstrated by the solid curve plotted for $A = B$. For the case of fuzzy preparation where $P\left(\varphi\right)$ has a distribution different from a delta function

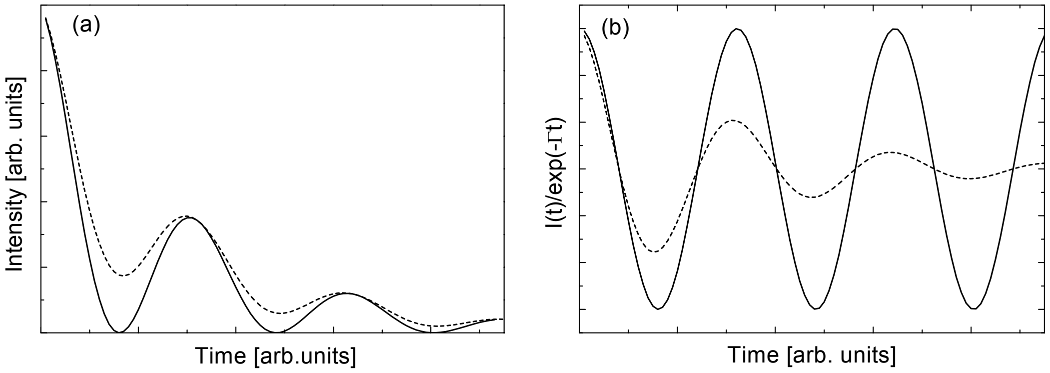

Figure 5.2: (a) Signal at the detector in accordance with formula 5.3 for pure $A = B$ (solid line) and fuzzy $A = 2B$ (dashed line) preparation of the initial state $\Psi(t = 0)$. (b) Signal plotted for infinite (solid line) and finite (dashed line) coherence time T_2. Note, only the term in the brackets of equation 5.3 is plotted, which corresponds to an infinite lifetime.

an additional background arises since $A > |B|$. This is demonstrated by the dashed curve in the figure for $A = 2B$.

The assumption behind the Weisskopf-Wigner approximation for $I(t)$ is that the electronic state is purely radiatively damped and stays, hence, entirely coherent during its lifetime.

In order to allow decoherence beside the pure radiative damping rate $\Gamma = 1/T_1$ for the total occupation, extra dampings need to be introduced. As there are $1/T_1^{'}$ for the occupation difference and $1/T_2$ for $\langle c_{\mathrm{x}} c_{\mathrm{y}}^{*} \rangle$ [79]. The last damping coefficient leads to a change in equation 5.3 like:

$$I\left(t\right) \propto \left(A + B \cdot e^{-\mathrm{t}/\mathrm{T}_2} \cdot cos\left(\Delta\omega_{\mathrm{ex}} t\right)\right) \cdot e^{-\Gamma \mathrm{t}} \tag{5.7}$$

Equation 5.7 offers a possibility to distinguish between an initial decoherence due to fuzzy preparation and an additional decoherence which takes place after the exciton has reached the ground state. In case of an infinitely long coherence time of the ground state the background and the oscillation decay with the same rate (see figure 5.2 (b) solid line), while for a shorter[1] coherence time it decays with different rates (dashed line).

After having discussed the manifestation of the preparation in the detector signal one can compare it with the experimental results. In figure 5.3 the typical time-resolved PL transients of a single QD for different excitation conditions are summarized. For excitation in the continuum states of the wetting layer (panel a), the PL decays monotonously with a single exponential time constant of $1/\Gamma = T_1 = 330$ ps. This value is in the range of the expected radiative lifetime. Any phase dependent correlation between c_{x} and c_{y} is washed out, yielding $\langle c_{\mathrm{x}}^{*} c_{\mathrm{y}} \rangle = 0$. No beating is observed in this case.

---

[1] That means, so short that the beating amplitude is changed during the signal decay, as it is the case if the coherence time is of the order of the lifetime.

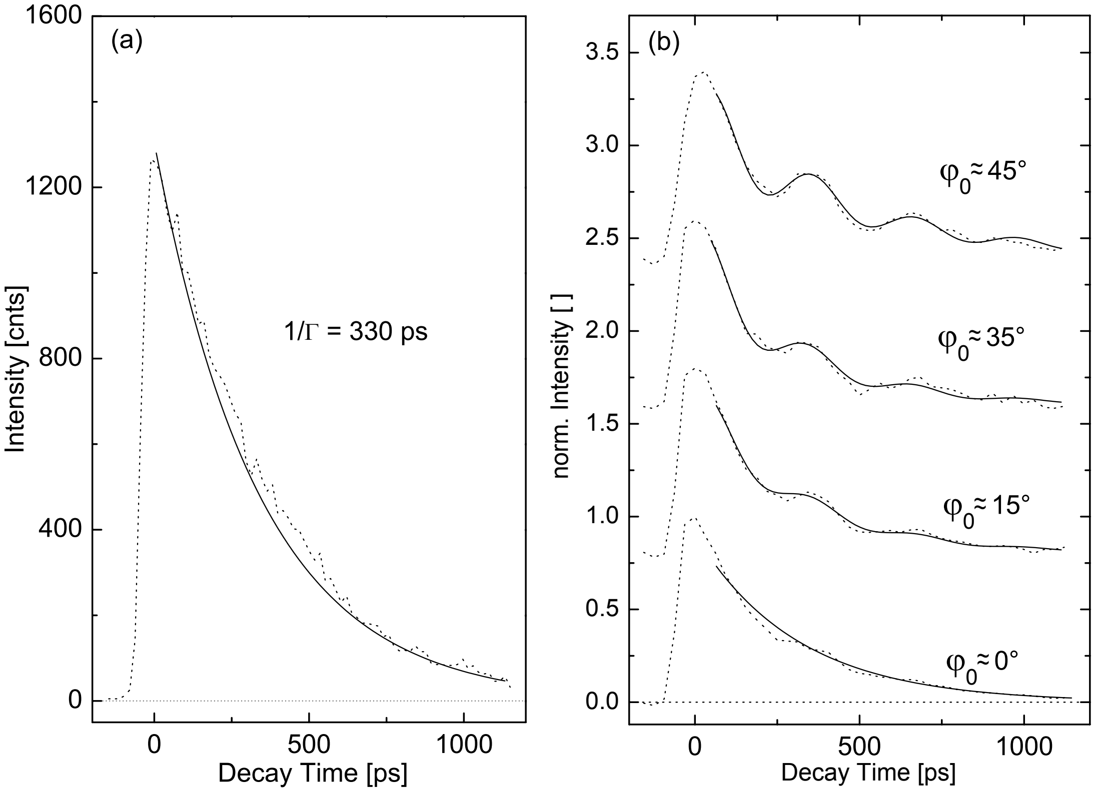

Figure 5.3: Polarization resolved transients of a single exciton under non-resonant excitation in the high energy states of the wetting layer (a) and the same dot under quasiresonant excitation (LO-phonon) measured in the geometry discussed in the text for four different angles between the fundamental axes of the QD and the excitation polarization (b).

However, after tuning the excitation energy in the 1-LO-phonon excitation feature and exciting the QD quasiresonantly, clear modulations of the signal appear for $\varphi_0 = 45°$ (upper curve). Furthermore, when analyzing parallel to the excitonic dipole moments ($\varphi_0 = 0°$), the beats disappear in accordance with equation 5.2, while the single-exponential background persists despite of $\vec{e}_\mathrm{A} \perp \vec{e}_0$. The beating period of $T_\mathrm{beat} = 320$ ps corresponds to a fine-structure splitting of $\Delta E_\mathrm{exc} = \hbar\,(\omega_\mathrm{x} - \omega_\mathrm{y}) = \hbar\,(2\pi/T_\mathrm{beat}) = 13\mu\mathrm{eV}$, which is consistent with the fact, that there was no resolvable splitting of this line observed in the spectral domain[2].

In none of the measurements in figure 5.3 a signal rise is observable, so that relaxation and subsequent radiative decay are well separated processes in time. This supports the above consideration that a loss of phase correlation between c_x and c_y during relaxation should be separately discussed from the loss of phase memory during recombination of the ground state exciton.

The observed beating for $\varphi_0 = 45°$ means that during relaxation the phase

---

[2] spectral resolution: $800\mu\mathrm{eV}$

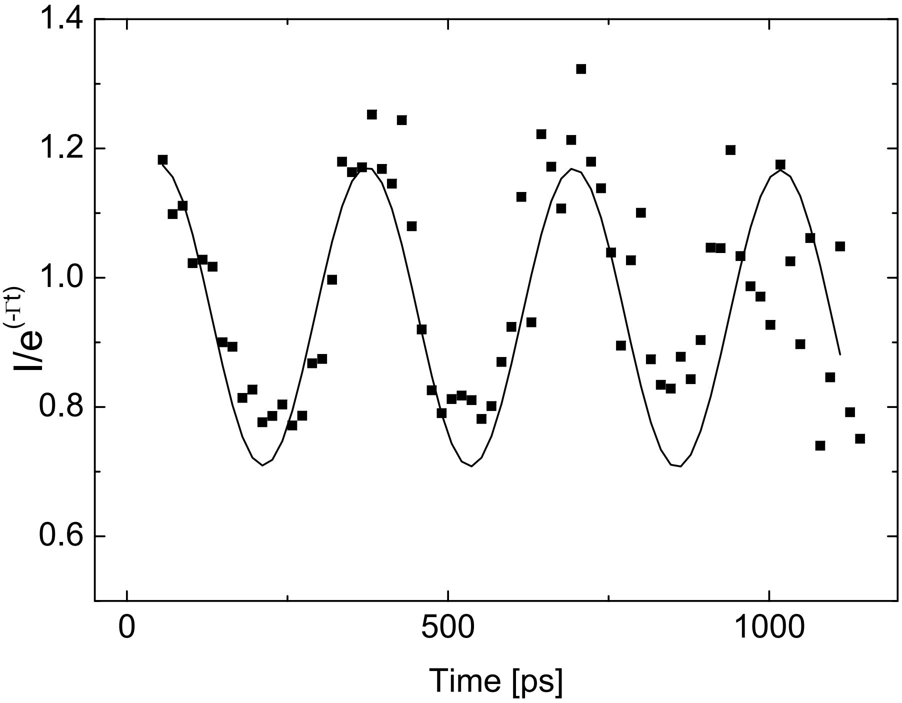

Figure 5.4: The PL-transient and the corresponding fit from figure 5.3 for $\varphi_0 = 45°$ divided by a single exponential decay with the lifetime.

correlation between c_x and c_y is not totally lost so that $P(\varphi)$ is far away from an equal distribution. Fitting the data curves with equation 5.3 (solid lines in figure 5.3) leads to the values of $u = (0.7 \pm 0.1)$ and $v = (0.05 \pm 0.05)$ for the statistical parameters in equation 5.6.

On the other hand, the found value u demonstrates also a rapid orientational relaxation of the imprinted dipole moment corresponding to a broadening of the distribution function $P(\varphi)$, since u is far away from the values $u = 0$ or $u = 1$ which results for $P(\varphi) = \delta(0)$ or $P(\varphi) = \delta(\pi/2)$, respectively.

This can be explained by the fact that the excitation at $E_0 + \hbar\omega_{\mathrm{LO}}$ creates an exciton-phonon complex, comprising components of both $|X_0, 1LO\rangle$ and $|X_1, 0LO\rangle$ (see figure 5.1 (a)) [80].

During this work there were no details about the internal structure of $|X_1\rangle$ available. Thus, it is very unlikely that $|X_1\rangle$ and $|X_0\rangle$ have identical dipole moments. Consequently the total moment is not conserved during succeeding evolution. The lifetime of the exciton phonon complex is limited by the decay of the LO in acoustical phonons, escaping from the QD, by which the current polarization is projected onto the $|X_0\rangle$ substates. The homogeneous width of $|X_1\rangle$ yields an upper limit of the LO-phonon lifetime of $\tau_{\mathrm{LO}} = 1.5$ ps, which is in fact close to the inverse level spacing $\hbar/(E_1 - E_0 - \hbar\omega_{\mathrm{LO}})$.

Note that the lifetime of the electron- (LO)phonon oscillation in bulk III-V semiconductors is about 100 fs or even shorter [81].

Unfortunately, the experiment has not the accuracy to give a value for the coherence time T_2. In order to evaluate the data further in figure 5.4 the measured transient from figure 5.3 for $\varphi_0 = 45°$ and the corresponding fit is plotted divided by a single exponential decay with the lifetime of 330 ps. It is clearly seen that in the range where the data is relevant (up to 800 ps) there is almost no decay of the beating amplitude. This fact proves directly that $\Gamma \gg 1/T_2$ and leads to the main conclusion of this experiment that once the exciton has reached the $|X_0\rangle$ ground state, practically no further decay of the coherence takes place.

5.2 Single hole spin relaxation

The previously discussed experiment deals with the transverse spin flip and was limited to information about the phase between two spin states. The experiments of this section are directed to the determination of the longitudinal spin flip time for the spin of a single carrier. The exciton in a QD comprises optically allowed and forbidden states. Their splitting by the electron-hole exchange interaction, leads to a complex multi component time scenario, where the contributions of the electron- and of the hole-spin can be hardly separated. In reality, a spinflip at one of the carriers of the exciton will switch the exciton from a bright to a dark state or oppositely.

One possible way to determine the spin relaxation properties of a single carrier is the use of charged QDs with resident carriers which provide access to the separate spin dynamics of electrons and holes [82, 18, 83]. Recently, an electron spin memory time of 15 ns has been deduced from ensemble data on n-doped InAs/GaAs QD structures [18].

As a consequence of the complicated valence band substructure with hh-, lh-,and so- bands, the spin relaxation for holes is generally faster than for electrons [19, 20]. In quantum wells, where heavy- and light- hole sub-bands are split, the relaxation time can reach 1 ns [84]. In QDs, where only single states for the heavy- and light hole are available (each of them two times degenerated) the relaxation time is expected to be longer.

Both following experiments use the fact that for a trion in the singlet state, due to Pauli exclusion principle, the spins of the two electrons are oppositely aligned to each other. As discussed in the second chapter the total spin of a trion in the singlet state is given by the spin of the heavy hole with projection of $J_{\mathrm{hh,z}} = \pm 3/2$ and recombination leave one electron of spin $S = \pm 1/2$ behind. The angular momentum rule demands $|\pm 3/2\rangle \rightarrow \sigma^{\pm} + |\pm 1/2\rangle$ with $\sigma^{\pm}$ denoting the respective circular light polarization. Therefore, the polarization of the emitted photon directly monitors the spin orientation of the hole, so that the emission of a $\sigma^{+}(\sigma^{-})$-photon indicates that the trion was in the $|+3/2\rangle$ ($|-3/2\rangle$)-state. An electron spin flip can be excluded since it would bring one electron in the next electronic shell to bypass the Pauli exclusion principle. The next electronic shell corresponds to the trion triplet state for the complex, which is $70 - 80$ meV on the high-energy side.

5.2.1 Spin-relaxation in QDs in presence of a longitudinal magnetic field

The lift of the degeneracy of the two allowed trion transitions due to the Zeeman effect in longitudinal magnetic field was already discussed in section 4.2. In what follows, these kind of data will be further analyzed in order to get an estimation of the hole spin relaxation time.

The experimental configuration is sketched in figure 5.5. The charged QD is excited nonresonantly with linearly polarized cw excitation. The magnetic field

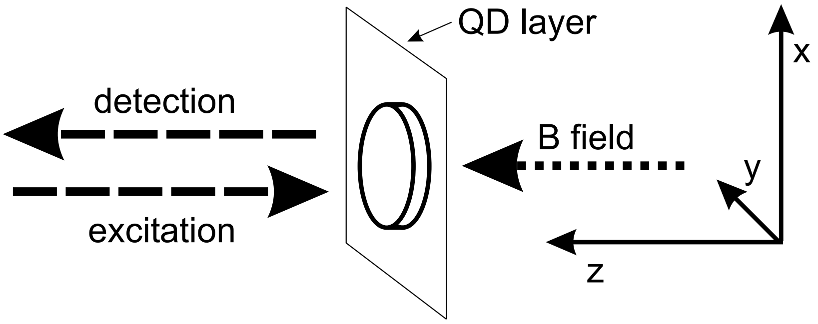

Figure 5.5: Scheme of the experimental configuration with an longitudinal magnetic field (Faraday geometry)

is directed parallel to the main quantization axis (z-axis).

As discussed in chapter 2, the eigenstates of the trion in this magnetic field configuration are given by $|\pm 3/2\rangle$ and the two PL emission lines correspond to the recombination from the lowest trion singlet state leaving one resident electron behind: $|\pm 3/2\rangle \rightarrow \sigma^{\pm} + |\pm 1/2\rangle$. In figure 5.6 (a) the PL of a trion is plotted for $B = 0$ T (bottom, single line) and for $B = 10$ T, where the line splits - as expected - in two oppositely circularly polarized components. The trionic nature of this line is proven by its splitting in Voight geometry into four components and the absence of a zero-field splitting at $B = 0$.

As already mentioned in chapter 2 and 4, for transverse magnetic field the field induced splitting is determined by the g-factors along the quantization axis. It reads:

$$\Delta E = \mu_{\mathrm{B}} \left(g_{\mathrm{h,z}} - g_{\mathrm{e,z}} \right) B_{\mathrm{z}} \tag{5.8}$$

and is experimentally evaluated for the present QD for different magnetic fields in figure 5.6 (b). It yields a difference of the g-factors in z-direction of $(g_{\mathrm{h,z}} - g_{\mathrm{e,z}}) = 1.5$ comparable with the value found in section 4.2. Using again the isotropic electron g-factor $g_{\mathrm{e,z}} \approx 1.1$ the hole g-factor in z-direction is calculated to $g_{\mathrm{h,z}} = 2.6$, which allows estimation of the energy splitting of $\Delta E_{\mathrm{h}} = g_{\mathrm{h,z}} \mu_{\mathrm{B}} B_{\mathrm{z}}$ between the two initial spin states of the recombination, which will be used below.

Since the excitation is linearly polarized and placed energetically in the high energy states of the wetting layer for this experiment, both of these ground states are addressed with equal probability. This means the excitation creates no optical orientation between the states $|+3/2\rangle$ and $|-3/2\rangle$ of the trion, while thermalization subsequently increases the occupation of the $|-3/2\rangle$ state. Hence, the ratio of the intensity yield of the PL lines provides a measure of the longitudinal spin relaxation time for the hole $T'_{1,\mathrm{h}}$. This time is of the same nature as the population difference decay time T'_1 introduced for the example of an exciton in section 2.5.3. The only difference is that in the present case the spin flip which provides the relaxation from one state to the other can be directly attributed to the hole.

The ratio $r = I_{\sigma^+}/I_{\sigma^-}$ is plotted in figure 5.6 (c) versus B. There is only a very weak variation up to $B = 10$ T, although, at this field strength, $\Delta E_{\mathrm{h}} \left(B_{\mathrm{z}} = 10T \right) =$

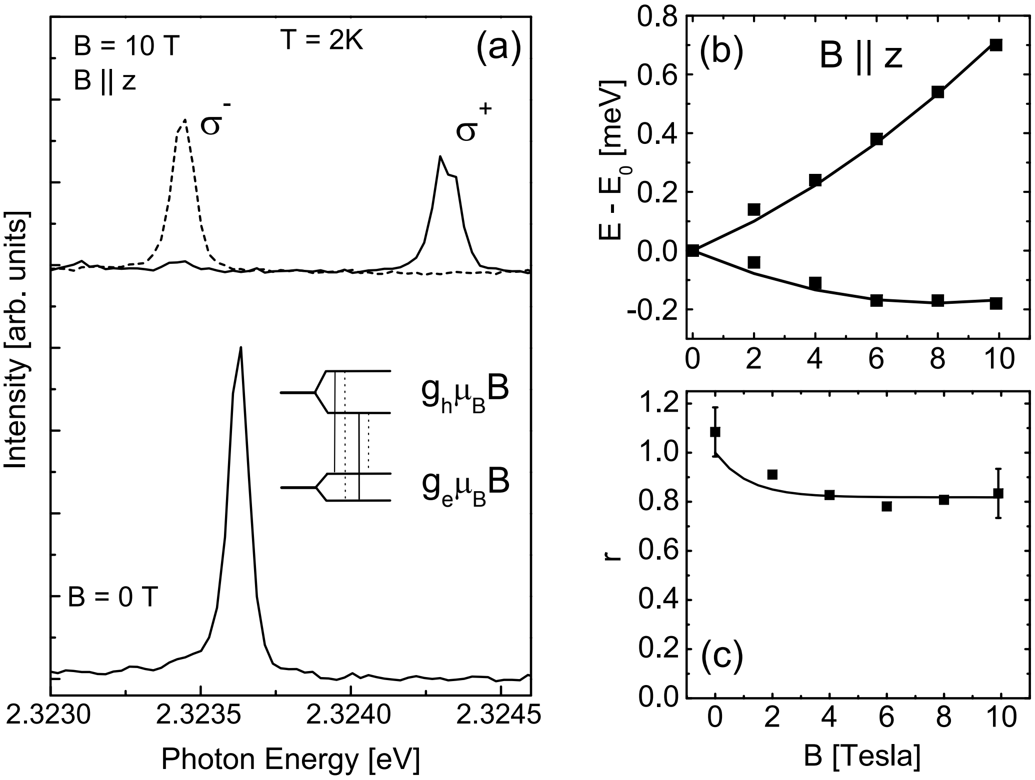

Figure 5.6: (a) PL spectra of a single negatively charged quantum dot under cw excitation at $B = 0$ T (bottom) and $B = 10$ T in Faraday geometry (top). In Faraday geometry both components are circularly polarized. Inset: scheme of the optical transitions. (b) Fan charts demonstrating the Zeeman splitting versus magnetic field. (c) Intensity ratio r between σ^+ and σ^- components. Solid line: fit with equation 5.10

1.50 meV is markedly larger than the thermal energy of $k_\mathrm{B}T = 0.34$ meV. This fact suggests slow thermalization and thus a long longitudinal spin relaxation time $T'_{1,\mathrm{h}}$.

One can describe this process in sense of two level rate equations. The influence of $T'_{1,\mathrm{h}}$ on these equations is discussed in more detail in the appendix B. Denoting by $n_\pm$ the occupation of the $|\pm 3/2\rangle$ state, these equations read:

$$\begin{aligned}\dot{n}_+ &= g_+ - \frac{n_+}{T_1} - \frac{n_+}{2T'_{1,\mathrm{h}}} + \exp\left(-\frac{\Delta E_\mathrm{h}}{k_\mathrm{B}T}\right)\frac{n_-}{2T'_{1,\mathrm{h}}} \\ \dot{n}_- &= g_- - \frac{n_-}{T_1} + \frac{n_+}{2T'_{1,\mathrm{h}}} - \exp\left(-\frac{\Delta E_\mathrm{h}}{k_\mathrm{B}T}\right)\frac{n_-}{2T'_{1,\mathrm{h}}}\end{aligned} \tag{5.9}$$

where T_1 is the radiative average level decay time (total lifetime) for the trion and $g_\pm$ denotes the respective pump rates. For steady-state conditions ($\dot{n}_+ = \dot{n}_- = 0$)

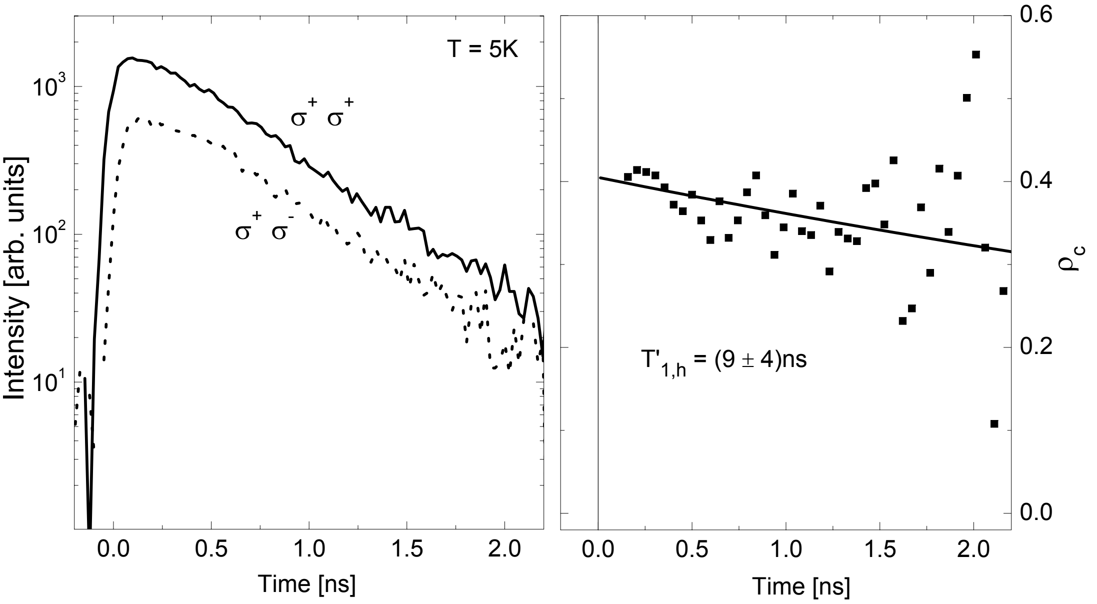

Figure 5.7: Left side: Decay transient of the trion PL under LO-phonon-assisted pulsed σ^+ polarized excitation for σ^+ (solid line) and σ^- detection (dashed line) at $T = 5$ K. Right side: Time dependence of the degree of circular polarization ρ_c (squares). The solid line is a fit with equation given in the text.

and $g_+ = g_-$, it follows:

$$r = \frac{n_+}{n_-} = \frac{1 + \frac{T_1}{T'_{1,\mathrm{h}}} \exp\left(-\frac{\Delta E_\mathrm{h}}{k_\mathrm{B} T}\right)}{1 + \frac{T_1}{T'_{1,\mathrm{h}}}}. \tag{5.10}$$

A fit of the data in figure 5.6 (c) with this formula yields a ratio of $T_1/T'_{1,\mathrm{h}} = (0.22 \pm 0.16)$. The average level decay of the trion is separately evaluated (not shown in the figure) by analyzing the unpolarized decay transient of the trion emission and a value of about $\tau = 500$ ps is found. Together with the above ratio this yields a longitudinal spin relaxation time in the range of 2..5 ns. In the next section a more direct measurement of $T'_{1,\mathrm{h}}$ in the time domain will be introduced.

5.2.2 Hole spin dynamics

Excitation of the trion ground state with σ^+ polarized pulses creates predominantly trions with a hole spin of $J_\mathrm{z} = +3/2$, as long the excitation energy is sufficiently below the trion triplet state. By analyzing the depolarization of the emission, one can determine $T'_{1,\mathrm{h}}$. The following experiment was done with the basic μPL setup, ps pulses from the Ti:sapphier laser setup and time correlated single photon counting for time resolved detection. Strictly resonant excitation of the ground state is faced with extreme stray light problems. For this reason, the excitation energy is tuned 28 meV above the ground state transition, which is still sufficiently below the triplet state. The time- and polarization resolved data for a single QD measured at $T = 5$ K are summarized in figure 5.7. The left side depicts the PL transients for σ^+ and σ^- detection. During the first 150 ps, the signal is still spoiled by stray light and will be hence excluded for the further analysis. Beyond this range, both signals decay in good approximation single exponentially. In the right part of the figure, the degree of circular polarization defined as $\rho_\mathrm{c} = (I_{\sigma^+} - I_{\sigma^-}) \,/\, (I_{\sigma^+} + I_{\sigma^-})$ is shown, where I_{σ^+} and I_{σ^-} are the intensities under σ^+ and σ^- polarized detection. Consistent with the magneto-PL results discussed in the preceding section, only very little depolarization within the trion lifetime is found. Note, however, that the initial degree of polarization, observed when the experimental data start to be meaningful, is only about 0.4. Under linearly polarized excitation, the PL signal exhibits no linear polarization component within the experimental accuracy of ±0.05. Solving the rate equations 5.9 now in the transient case and, since there is no magnetic field, for $\Delta E_\mathrm{h} = 0$ yields for the degree of polarization:

$$\rho_\mathrm{c} = \rho_0 \exp\left(-\frac{t}{T'_{1,\mathrm{h}}}\right), \tag{5.11}$$

where ρ_0 is the initial degree of polarization. From the fit of the data in figure 5.7 (right side) one obtains $T'_{1,\mathrm{h}} = (9 \pm 4)$ ns and $T_1 = 500$ ps. These numbers compare reasonably well with the ratio $T_1/T_{1,\mathrm{h}'}$ determined from the magneto-PL data in the preceding section. However, here $T'_{1,\mathrm{h}}$ is slightly longer than the range estimated above. This behavior was theoretically discussed by *Woods et al.* [85] where the hole spin relaxation in a QD due to acoustic phonon assisted spin flips was evaluated. The scattering rates for relaxation of the holes due to the emission and absorption of acoustical phonons was calculated. It was found that in case of zero magnetic fields where the two spin states are degenerated the scattering rate is zero. For non-zero magnetic fields, where the degeneracy is lifted, the scattering rate grows with $\propto B^7$. In case of degenerated spin states the scattering with phonons is less efficient since there are no phonons with zero phonon energy available.

In order to uncover the temperature dependence of the spin relaxation time the same experiment as above is carried out on higher temperatures. Except for one difference: for a better signal to noise ratio, the temperature dependence was studied on a mesa with 400 μm^2 size. Here, the emission lines from single QDs cannot be separated. The excitation photon energy is tuned to the maximum of the inhomogeneously broadened PL band occurring for excitation in the continuum states of the wetting layer. This ensemble consists of charged and uncharged QDs, however, the linearly polarized excitons from uncharged QDs do not contribute to the decay of circular polarization degree ρ_c [5, 16, 15]. The actual PL band is plotted in figure 5.8 (a). It has a width of 10 meV and its maximum is located 28 meV below the excitation laser. The excitation via 1-LO-phonon assistance is hence predominant, resembling the situation for the measurements on single QDs. In figure 5.8 (a) this first phonon replica is plotted for σ^+ and σ^-

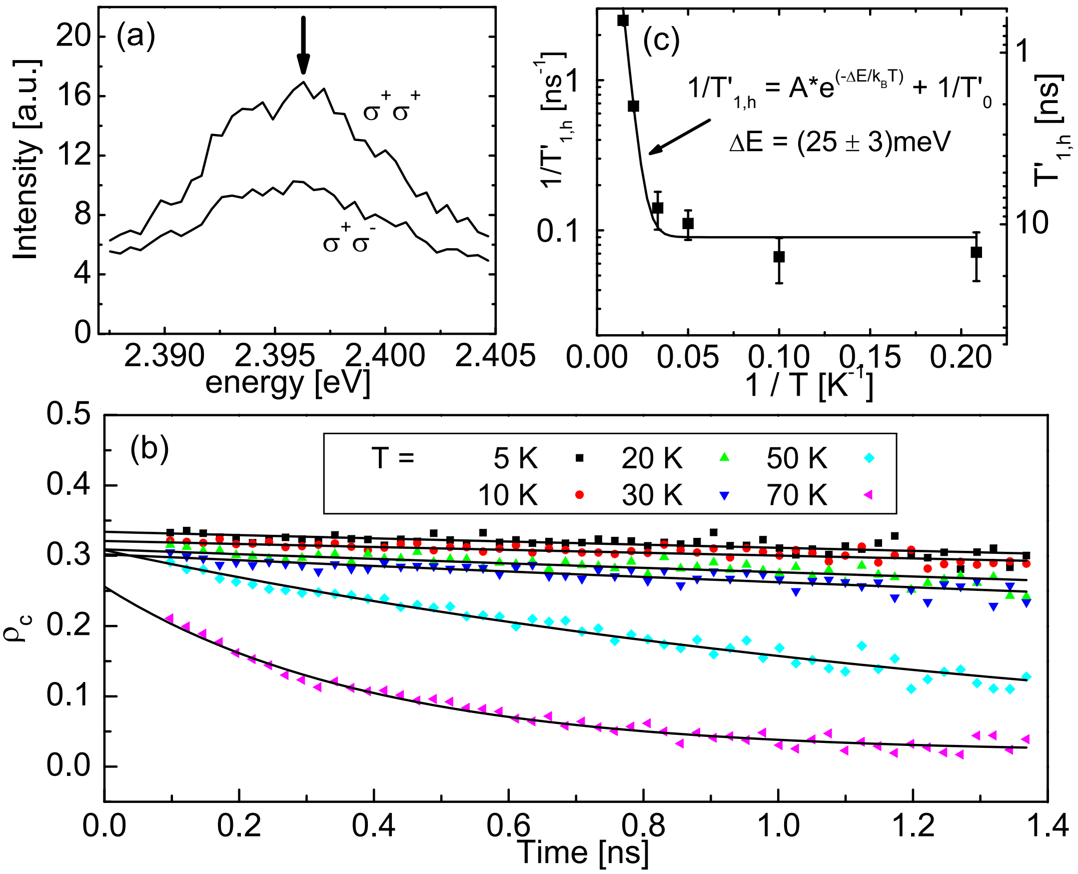

Figure 5.8: (a) Time integrated PL spectra measured in σ^+ and σ^- polarization from an ensemble of QDs under σ^+ pulsed excitation one LO-phonon energy above the value marked by the arrow. (b) Time dependence of ρ_c taken in a 0.5 meV window around the arrow. The solid curves correspond to an exponential fit with equation 5.11. (c) Temperature dependence of the spin-relaxation rate $1/T'_{1,\mathrm{h}}$. The solid curve is a fit with $(0.09 + 160 \cdot \exp(-\Delta E/k_\mathrm{B}T))\,\mathrm{ns}^{-1}$ and ΔE given in the text.

detection polarization. Across the whole band the polarization is positive, however, with smaller values at the edges than at the center. Obviously, acoustical phonons come into play at the edges as a source of further depolarization. In figure 5.8 (b) the time resolved polarization degree taken at the maximum of the LO-phonon replica (arrow in figure 5.8 (a)) is plotted for different temperatures between 5 and 70 K. The low-temperature curves ($T < 30$ K) are consistent with the results for the single trion PL, demonstrating that the ensemble data are not disturbed by statistical properties. From all transients the spin relaxation times are extracted by an exponential fit and summarized in figure 5.8 (c). A marked shortening proceeds at higher temperatures resulting in a value of only $\tau_\mathrm{SF} = 0.8$ ns reached at 70 K. The data points follow closely an Arrhenius plot with an activation energy of $\Delta E = (25 \pm 3)$ meV.

In general, the spin dynamics of the hole are governed by the substructure

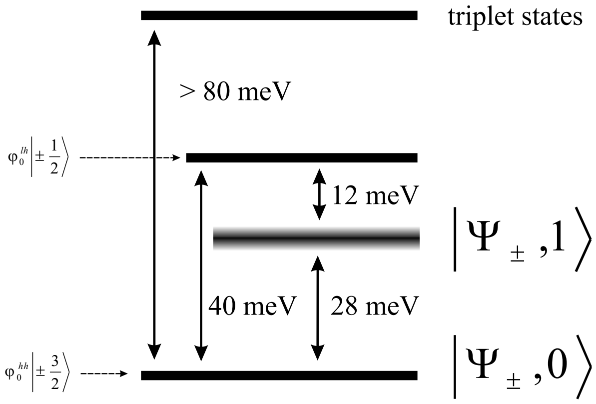

Figure 5.9: Scheme of the energy separation between the trion hole ground state ($|\Psi_{\pm},0\rangle$) and the trion-LO-phonon state ($|\Psi_{\pm},1\rangle$) in respect to the light- and heavy-hole ground state ($\varphi_0^{\mathrm{lh}}|\pm 1/2\rangle$ and $\varphi_0^{\mathrm{hh}}|\pm 3/2\rangle$) in the absence of heavy-light-hole mixing. The index ± denotes that both positive and negative angular momentum projections are taken into account.

of the valence band. At $\vec{k} \neq 0$, none of the states $|j_{\mathrm{z}}\rangle$ is a true eigenfunction of the angular projection operator $\mathbf{J}_{\mathrm{z}}$. In case of a QD this fact leads to hole wave functions of the form $\Psi = \sum \varphi_{j_{\mathrm{z}}}(\vec{r})|j_{\mathrm{z}}\rangle$, restricting the following consideration to the heavy- and light- hole bands ($j_{\mathrm{z}} = \pm 3/2, \pm 1/2$).

As the PL excitation measurements uncovered the trion has an excited state around 40 meV above the ground state transition (see section 4.3) which corresponds to the second hole shell, presumably associated with the first light-hole shell. On the other hand, the second electron shell is situated at least at energies above 80 meV. This is a trion triplet state and it can be clearly identified by its fine structure.

In figure 5.9 the general situation is schematized. The LO-phonon assisted excitation, 28 meV above the heavy hole ground state, is only 12 meV below the first light hole shell. Due to the large energy separation to the triplet state, the main contribution to Ψ arises from the heavy- and light-hole ground states. The trion wave function can be determined by perturbation theory and can be written as:

$$\begin{pmatrix}\Psi_+\\ \Psi_-\end{pmatrix} = \varphi_0^{\mathrm{hh}}\begin{pmatrix}\left|+\frac{3}{2}\right\rangle\\ \left|-\frac{3}{2}\right\rangle\end{pmatrix} - \frac{\varphi_0^{\mathrm{lh}}}{\Delta}\begin{pmatrix} I\left|-\frac{1}{2}\right\rangle + S\left|+\frac{1}{2}\right\rangle\\ I^*\left|+\frac{1}{2}\right\rangle - S^*\left|-\frac{1}{2}\right\rangle\end{pmatrix}. \tag{5.12}$$

Here I and S are the $\mathbf{k}\cdot\mathbf{p}$ matrix elements of the Luttinger-Hamiltonian. They can be evaluated as:

$$I = \sqrt{3}\,\frac{\hbar^2}{2m}\,\gamma_3\left(\frac{\partial}{\partial y} + i\frac{\partial}{\partial x}\right)^2 \tag{5.13}$$

$$S = \sqrt{3}\,\frac{\hbar^2}{m}\,\gamma_3\,\frac{\partial}{\partial z}\left(-\frac{\partial}{\partial x} + i\frac{\partial}{\partial y}\right) \tag{5.14}$$

A more detailed evaluation of the wave functions 5.12 is given in appendix A. The terms in 5.12 lead to two different sources of spin coupling. At first, the excitation imprints the spin not totally perfectly. A σ^+ photon can create not only a Ψ_+ wave function from an initial spin-up electron as is done by the first term in equation 5.12. By the second term in each equation, which is a parity conserving term and proportional to I or I^* it creates also Ψ_- wave function from an initial spin-down electron, which is a softening of the selection rule.

Secondly, by the third term, which is proportional to S or S^*, a flip between a once created Ψ_+ and Ψ_- is mediated. The Term S which has odd in-plain symmetry, does not conserve parity. Note that interactions V, which are not depending on the spin, then provide a non-vanishing scattering matrix element $\langle\Psi_+|V|\Psi_+\rangle$.

The experimental results show both kinds of spin coupling. The fact that the signal exhibits almost no linear polarization signifies that the light-hole admixture is very small in the zero-phonon trion ground state $|\Psi_\pm, 0\rangle$, which is $\Delta_{0\mathrm{LO}} =$ 40 meV below the light-hole level. This situation is different for the one-LO trion state $|\Psi_\pm, 1\rangle$ which is only $\Delta_{1\mathrm{LO}} = 12$ meV below the light-hole level, where the QD is excited. This energy differences $\Delta = \{\Delta_{1\mathrm{LO}}, \Delta_{0\mathrm{LO}}\}$ enter the wave functions 5.12 in the denominator of the second and the third term.

Taking the ratio $\Delta_{0\mathrm{LO}}/\Delta_{1\mathrm{LO}} = 40/12$ into account, the light-hole admixture, provided by the mixing coefficients $I^\pm/\Delta$ and $S^\pm/\Delta$, is for the $|\Psi_\pm, 1\rangle$ state by more than a factor of three stronger than for the $|\Psi_\pm, 0\rangle$ state. For their squares this yields even an order of magnitude.

So σ^+ polarized excitation in the $|\Psi_\pm, 1\rangle$ state creates a significant portion of Ψ_-. During the relaxation from the $|\Psi_\pm, 1\rangle$ state, this is converted in the practically pure angular momentum state $|\Psi_\pm, 0\rangle \approx \varphi_0^{\mathrm{hh}} \left|\pm\frac{3}{2}\right\rangle$, which subsequently gives rise to both σ^+ and σ^- PL components. This depolarization effect is not connected with a direct flip between Ψ_+ and Ψ_-. As is visible in figure 5.7, it causes the initial drop of the polarization down to $\rho_\mathrm{c} \approx 0.4$ before the first evaluable photons are observed after about 150 ps. In general, the time scale for this kind of depolarization is given by the lifetime of the trion-LO-phonon complex, which is limited by the decay of the optical phonon, most probably in acoustical phonons. The PL spectra for trions in chapter 4.1 does not show any noticeable PL yield from this complex, indicating that the lifetime is at maximum a few 10 ps. This time compares well with the fact that the initial drop of polarization - observed in figure 5.7 - is already completed after 150 ps, where the signal overcomes the scattered laser light. In comparison, on excitons in uncharged CdSe/ZnSe QDs a similar effect is observed. There, a partial loss of polarization in time integrated emission during the relaxation from the one- to the zero LO-phonon complex appears [16].

Since the above discussed kind of depolarization appears on a time scale shorter than 150 ps, the second much slower depolarization seen in the low-temperature PL transients is related to the scattering from Ψ_+ to Ψ_- in the trion ground state. Here the spin relaxation times are found to be longer than 10 ns.

There are different possible reasons for such behavior: In the literature the hyperfine interaction with the nuclear spin is discussed, which defines a limit for the electron spin flip in QDs [86]. In the present case, the spin flip can be attributed to the hole. For holes this kind of interaction should have less effect, because of their p-type Bloch functions [87].

A direct flip between Ψ_+ and Ψ_- by a spin independent process requires parity breaking, so that $S^{\pm}$ should be non-zero. A QD shape with a higher in-plane anisotropy (i.e. symmetry below $C_{2\mathrm{v}}$, $D_{2\mathrm{v}}$) can be a reason for this. Alternatively, envelope functions of excited states need to be included, which have a larger energy separation Δ and hence a smaller mixing element. The resulting matrix element for the spin flip $\langle\Psi_{\pm}|V|\Psi_{\mp}\rangle$ mediated by an arbitrary scattering potential V is however of second order $\left(\approx I^{\pm}S^{\mp} \approx \frac{1}{\Delta^2}\right)$ in the band mixing.

In conclusion, in this section the longitudinal spin relaxation time for a hole in a single negatively charged QD is evaluated in two different ways. In both cases a low temperature spin relaxation time $T^{'}_{1,\mathrm{h}}$ of several nanoseconds was found. While it is not possible at the moment to specify the actual low-temperature spin flip mechanism (defects, disorder, phonons ...), the above considerations demonstrate that the observation of very long spin flip times for the hole is in no contradiction to the general expectation. The somewhat shorter $T^{'}_{1,\mathrm{h}}$ obtained from the magneto PL data might indicate a more efficient spin flip when the degeneracy of the doublet is removed, enabling direct transition with acoustical phonons.

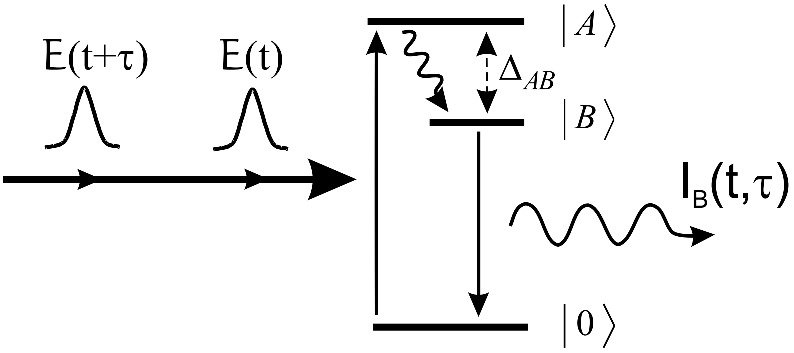

Figure 5.10: Scheme of a three level system where the state $|A\rangle$ is phase locked temporally coherently controlled and its occupation is monitored by a lower lying state $|B\rangle$.

5.3 Coherent control

The topic of the following section is the optical coherence properties of single quantum dots. The fundamental parameter describing the degree of optical coherence of a system is the optical dephasing time, as discussed in chapter 2. A powerful experimental concept to uncover this fundamental property is the variation of the relative phase in a sequence of two optical pulses interacting with the quantum system, as discussed in the introduction.

In subsection 3.2.3 it was said that this concept of coherent control is used in this thesis in the way of phase locked temporal coherent control where single interference fringes can be resolved. By choosing an appropriate energy, in accordance to the state under observation, the population of this state is coherently controlled by varying the relative phase of the excitation pulses in accordance to equation 2.28.

One central experimental problem is given by the question: How to monitor the population of a specific state if this population is coherently controlled by laser pulses with an energy strictly resonant to this state? The scheme in figure 2.3 suggests that the PL emission from the coherently controlled state can be used. In this case it is hard to distinguish between the scattered excitation laser and the PL emission if the latter one is detected with standard time integrating methods. In the experiment of *Marie* et al. on excitons in GaAs quantum wells, this problem was solved by applying a technique which is usually used for time resolved experiments [51]. The PL emission is up converted in order to separate the scattered laser light created by both excitation pulses from the emitted PL. For this an additional laser pulse is overlapped with the PL in a non linear LiO_3 crystal at a time where the scattered laser light is over. In this case, only a small portion of the PL transient which is available is analyzed and so this method can be mainly applied, since the PL intensities from quantum wells are sufficiently high.

In the present case, where a state in a single QD will be coherently controlled, the signal intensities are much smaller and methods are preferred which can integrate the total PL emission. In this case, the emission from the controlled state can not be directly analyzed.

An alternative is given by the three level system summarized in figure 5.10 and represents the central idea of the coherent control experiments conducted here. Here an upper state $|A\rangle$ is coherently controlled. In order to monitor its occupation, a second state $|B\rangle$ is used, which is in between the state $|A\rangle$ and the crystal ground state $|0\rangle$. If the relaxation $|A\rangle \rightarrow |B\rangle$ is much faster with respect to the relaxation $|B\rangle \rightarrow |0\rangle$ then the population in the state $|B\rangle$ provides a measure of the population in the state $|A\rangle$. Consequently, the emission from the state $|B\rangle$ can then be used as a monitor of the population in the state $|A\rangle$. Additionally, if the transition $|A\rangle \rightarrow |B\rangle$ is a radiative one, also the emission from this transition can be used as a monitor of the population of the state $|A\rangle$. If the energy separation Δ_{AB} is larger than the spectral width of the excitation laser, so that the laser has no spectral components at the state $|B\rangle$, a clear distinction between scattered laser light and the PL emission used for population monitoring is possible.

There are several possible implementations of the three level system from figure 5.10. A widely applied configuration is the coherent control of an excited state by using the correspondent exciton ground state as a monitor [14].

Another possibility is the coherent control of the biexciton population. In this case, the corresponding exciton can be used to monitor the biexciton population. The energy of the biexciton state is twice larger than the exciton energy reduced by the biexciton binding energy. So, if the biexciton is created by a two photon absorption process (TPA), the used excitation laser can be still below the exciton state and the direct excitation of the exciton can be prevented, if the biexciton binding energy is sufficiently large. *Blanchet* et al. demonstrated on an ensemble of cesium atoms that the population of a biexciton state can be indeed controlled by two-photon coherent control [88]. Two photon coherent control on the biexciton in a single QD is first realized during this work and will be discussed in detail below.

This section is organized as follows: At first, the experimental results of the coherent control of an excited state in a single QD will be discussed. In a second part the TPA excitation of a biexciton for an ensemble and for a single QD will be summarized. In a third part, after the reader is convinced that a biexciton is excited via two-photon process, the two-photon coherent control data for a single QD will be presented.

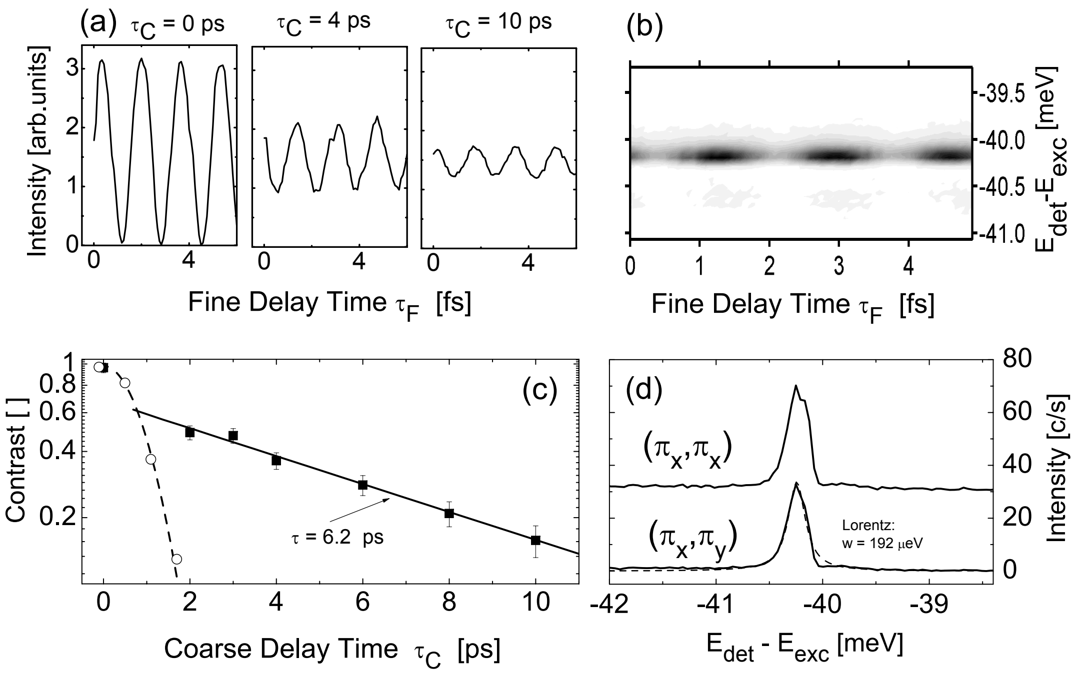

Figure 5.11: Excited state coherent control: (a) Single photo interferograms for different delays τ_C between the two pulses. (b) Two dimensional plot of the spectra for $\tau_C = 4$ ps. (c) Contrast as a function of the pulse delay τ_C (solid squares) together with an exponential fit of $\tau = 6.2$ ps (solid line). For comparison the laser autocorrelation function is inserted (open circles, dashed line). (d) Ground state emission under excitation in the excited state for two configurations of linear polarization for excitation and detection.

5.3.1 Single photon coherent control of excited states

First, in this section the experimental concept of coherent control with two phase locked pulses will be applied to control the population of the excited state of a single QD.

Such kind of coherent control of a single photon resonance has been recently achieved in self-assembled III-V QDs, yielding dephasing times in the range of 10 to 40ps [14, 36, 37].

As discussed in section 4.3 the exciton has its first excited state around 40 meV above the ground state exciton. The excitation source is tuned resonant to the excited state. Since the spectral width of the excited state is narrow compared with the laser, the value of the excitation energy was checked by tuning the excitation laser away from the excited state and observing the disappearance of the corresponding ground states emission.

The coherent control data for a single QD is summarized in figure 5.11. The interferograms in panel (a) represent the spectral integrated intensity of the ground state emission while exciting with two phase locked pulses in the excited state. Both pulses had the same polarization and power density of 2.5 μJ/cm^2 and they are separated in time by $\tau = \tau_C + \tau_F$ as discussed in section 3.2.4.

Applying the concept from section 2.5.1 every excitation pulse creates a subwave function $X_1(t)$ in the excited state. The three interferograms for a coarse delay of 0, 4, and 10 ps in panel (a) of figure 5.11 can be divided into two groups. For $\tau_C = 0$ ps the oscillations are due to the interference of the electro magnetic field from the overlapped laser pulses. The oscillations demonstrate only the change of the excitation laser intensity and provide no information about phase memory of the excited state. On the contrary, at larger coarse delay times (in the figure displayed for $\tau_C = 4$ and 10 ps) the oscillations arise directly from the interference of the subwave functions $X_1(t)$ and $X_1(t+\tau)$, created from the first and the second pulse. In panel (b) the same data for $\tau_C = 4$ ps is plotted spectrally resolved for the used ground state emission. It demonstrates that on the time scale where the interferogram is acquired no spectral shifts take place.

In accordance with equation 2.28, τ can be divided in two parts. The oscillations appear if the fine delay time τ_F is varied and the oscillation period reflects the energy of the excited state. The amplitude of the oscillations is a function of the coarse delay time τ_C. In order to evaluate this dependence more carefully in panel (c) of figure 5.11 the fringe contrast of the oscillations for this QD is plotted. This fringe contrast is similar defined as the degree of polarization in subsection 5.2.2 in the way:

$$c(\tau_C) = \frac{I_+ - I_-}{I_+ + I_-}. \tag{5.15}$$

Here I_+ and I_- represent the mean value of the local maxima and minima of the oscillating intensity, respectively. The contrast is evaluated from the data in panel (a) by fitting a sinus function $I(\tau_F) = o + a \cdot \sin(\omega \cdot \tau_F)$ into the interferogram for every τ_C. Since the resulting amplitude a and the offset o are connected with the extreme values I_+ and I_- by $I_+ = o + a$ and $I_- = o - a$ the fringe contrast can be calculated by $c(\tau_C) = a/o$. Equation 2.28 says that the interference part of the intensity, which is proportional to the occupation of the controlled state, decays exponentially with the optical dephasing time $\tau_p = 1/\gamma$ for this state. Putting this into equation 5.15 this leads to the fact that $c(\tau_C)$ decays with the same exponent and so it reflects the loss of phase memory. The contrast data in panel (c) demonstrates that this happens indeed single exponentially with a coefficient of $\tau_p = 6.2$ ps. For comparison the laser autocorrelation function (dashed line) is plotted in the panel. It is clearly seen that after more than two picoseconds delay the pulses are well separated in time, but the interference of the two subwave functions is still present, demonstrating the nature of the interference fringes. The fact that the contrast really decays single exponentially suggests that the controlled excited state is only homogeneously broadened. The optical dephasing time of 6.2 ps corresponds in the spectral domain to a homogeneous width of $\gamma = \hbar/\tau_p = 100$ μeV. This compares well with the half-width of the excited state usually measured in PLE spectra of several hundred micro electronvolts.

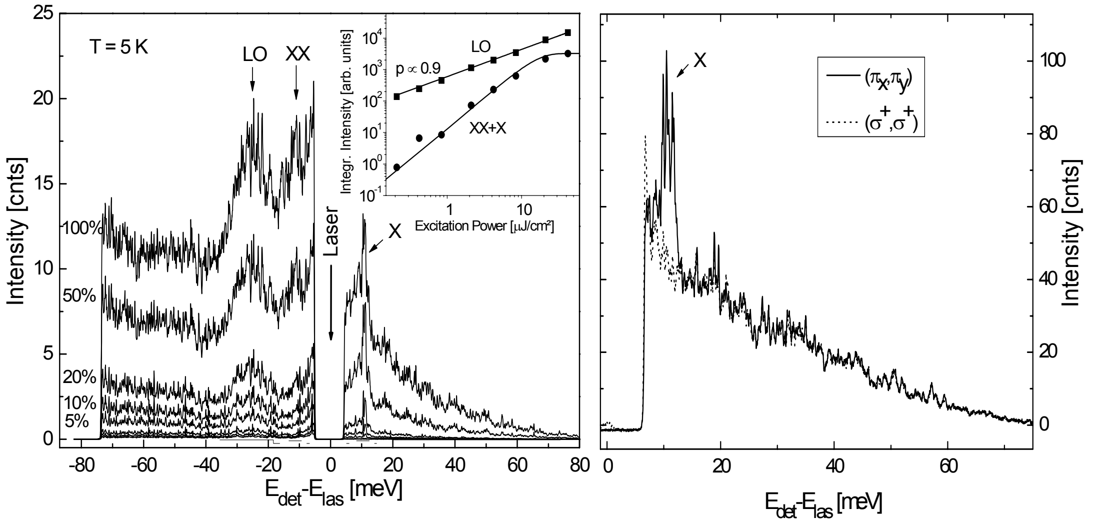

Figure 5.12: Left side: Ensemble PL excited in the PL-band maximum with linearly polarized ps pulses for different excitation power densities (100% $\widehat{=}$ 40μJ). Inset: The squares represent the integrated intensity of the LO-phonon feature below the laser, while the circles represent the sum of the integrated intensities for the exciton (X) and the biexciton (XX) emission excited via TPA. The solid lines are fits with $\propto b \cdot x^{\mathrm{p}}$. Right side: Spectra at the high energy side for linear and circular excitation polarization. The dashed curve clearly demonstrates the disappearance of the exciton TPA feature (X) for circular polarized excitation.

5.3.2 Creation of biexcitons by two photon absorption

Biexcitons can be created directly by a resonantly enhanced two photon process. This is already observed on interface islands in III-V quantum wells [89] as well as on ensembles of II-VI QDs [55]. So far there is no observation on single Stranski-Krastanov QDs. First, the TPA excitation will be demonstrated by tuning an excitation laser to the center of the inhomogeneously broadened ensemble of 10^5 QDs.

In figure 5.12 (left side) the time integrated emission from such a QD ensemble under linearly polarized ps-excitation is summarized for different excitation intensities. Approximately 11 meV below and above the laser line two narrow bands (labelled with XX and X) with a half-width of about 2 meV are visible. As will be demonstrated in more detail below, the band XX is due to the recombination from biexciton states into the correspondent exciton states, which then further recombine into the crystal ground state emitting the band X. Both of these bands grow superlinearly with the excitation power in contrast to all other emissions below the laser which show a linear power dependence, see e.g. the LO phonon band which grows with $I \propto P^{0.9}$. Except the band labelled with XX the other emissions below the laser are from QDs which are excited by one photon per QD under emission of one or several phonons. Such single photon excitation processes should show a linear power dependence and this is in correspondence

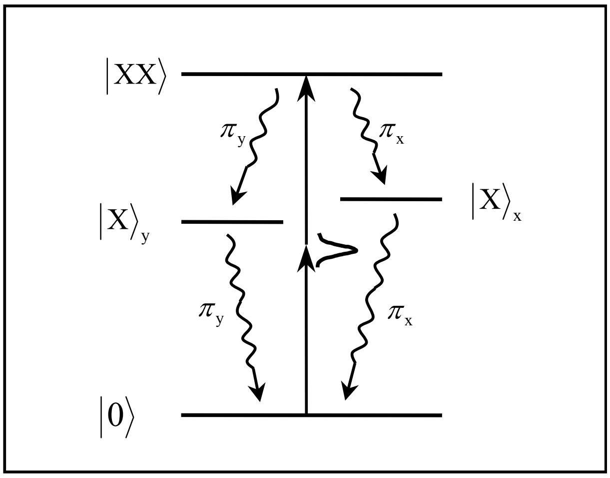

Figure 5.13: Scheme of the optical transitions and their polarizations in a QD with in-plane anisotropy. The exciton ground state $|X\rangle$ is split by electron-hole exchange in the sub-states $|X\rangle_{\mathrm{x}}$ and $|X\rangle_{\mathrm{y}}$. In the center, the two arrows and the symbol of a laser pulse indicate that the excitation is spectrally well separated from the exciton ground state.

with the experimental result. The band above the laser labelled with X is also surrounded by a background emission. In contrast to the situation below the laser this background also grows superlinearly. The reason for this is probably that TPA processes also create high energy electron-hole pairs in ZnSe, which can relax in all available QDs creating then a background in the spectra. If the excitation polarization is chosen circular, both bands (X and XX) disappear. This is clearly demonstrated for the high energy side in figure 5.12 (right side) and will be discussed below in connection with the single dot data.

There are now different possibilities to prove the biexcitonic nature of the emission lines labelled X and XX. At first their energy separation of 22 meV. In figure 5.13 a scheme of the energy levels is sketched. The energy of the biexciton is $E_{XX} = 2E_X - E^B_{XX}$, where E_X is the exciton ground state energy and E^B_{XX} is the biexciton binding energy. The recombination of the biexciton is a cascaded process summarized in figure 5.13. One electron-hole pair from the biexciton recombines under emission of a photon with an energy of $E_X - E^B_{XX}$ and leaving one exciton behind. Further recombination of the exciton leads to the emission of one photon with the exciton energy E_X. So the distance of the lines XX and X corresponds to the biexciton binding energy. The found value of 22 meV compares well with the published range [55]. A second prove is given by the excitation power dependence, evaluated in the inset of figure 5.12. Two photons are necessary in order to create one biexciton, so there should be a quadratic dependence on the excitation power for the line XX and X. However, at high excitation powers a saturation appears, caused by depletion of the ground states. Taking this depletion into account, the occupation of the biexciton states as a

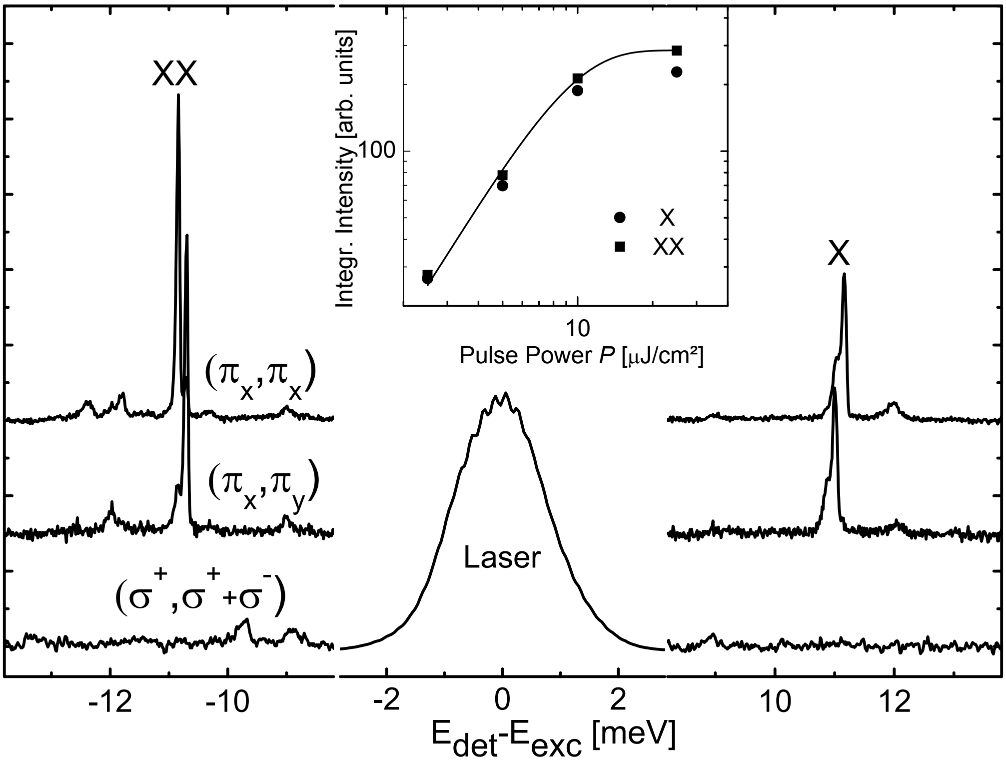

Figure 5.14: Exciton and biexciton emission from a single QD (QD#1) in a 100 nm mesa under pulsed excitation measured in different polarization configurations at low temperature. The round parentheses $(e_{\mathrm{exc}}, e_{\mathrm{det}})$ used in the figure, indicate the polarization configuration of excitation and detection, respectively, where the indices x and y denote the [110] and [1$\bar{1}$0] crystal axes. All spectra are plotted relative to the energy of the excitation laser of $E_{\mathrm{exc}} = 2.437$ meV. Inset: Integral PL yield of the exciton and biexciton recombination versus excitation power. The solid line represents a fit with $I \propto (1 - \exp(-b \cdot P^2))$ and $b = 0.013$.

function of the excitation power is given by:

$$N_{\mathrm{xx}} \propto \left(1 - e^{-b \cdot P^2}\right) \tag{5.16}$$

where P is the excitation power and b represents the degree of depletion. The solid line through the circles in the inset in figure 5.12 is a fit with equation 5.16 and $b = 0.004$. For comparison in the inset the power dependence of the LO-phonon band is plotted, demonstrating a clear linear power dependence.

The third fact is that the spins of the two electrons as well as of the two holes in the biexciton are antiparallel oriented, which yields $J_{\mathrm{xx}} = 0$ for the biexciton state. Since the crystal ground state also has no angular momentum, a biexciton can be only created via TPA from two photons with oppositely circular polarization to fulfill the momentum conservation rule. If the excitation is made with pure σ^+ or σ^- polarized light the emission lines X and XX should disappear. This is in accordance with the observation in figure 5.12 (right side). The clearly observed excitonic (X) and biexciton (XX) emission for linearly polarized excitation disappears if the excitation polarization is chosen circularly, while the background remains at the same intensity.

In case of a single QD, the same tools as for the above discussed ensemble data can be used to prove that the biexciton under observation is excited by a TPA process. Additionally, if the single QD has an in-plane anisotropy the fine structure can provide further information. In the scheme of figure 5.13, what is happening for such a QD is sketched. As discussed in the previous chapters the radiative ground state exciton with $J_X = \pm 1$ is split by electron-hole exchange interaction, while the non-degenerated biexciton ($J_{XX} = 0$) is not split. This leads to different transition energies with different linear polarizations. The corresponding experimental data for a single QD are summarized in figure 5.14. The curves show the excitonic and biexcitonic emission for three different polarization configurations. The two upper curves show the signal detected in parallel and crossed polarization to a linearly polarized excitation. There the exciton splitting is manifested by the reversed polarization. Both X and XX emission doublets are showing identical line separation of 150 μeV. Again, both lines disappear, if the excitation polarization is turned to circular and they are in superlinear dependence on the excitation power (inset). If the excitation energy is tuned out of the center of $E_x + E_{xx}^B/2$ both lines disappear very fast simultaneously. This behavior will be discussed in more detail below.

After carefully proved that the biexciton is created by a TPA process and the two emission doublets are of biexcitonic nature, they will be used to investigate the optical dephasing properties of the biexciton in a single QD by the two-photon coherent control experiment discussed in the next section.

Before doing this, one remark on the excitation. For an efficient two-photon absorption high excitation intensities are important. For this reason, in the present case a pulsed laser on the ps- timescale is used. Since the pulses are spectrally broadened in accordance with the pulse length, it is of paramount importance that the excitation laser has no spectral components at the single photon exciton resonance. One advantage of the used sample structures is the large biexciton binding energy in comparison to the spectral width of the laser of about 1.5 meV.

5.3.3 Coherent two photon control of biexciton states

Two-photon coherent control interferograms for exactly the same biexciton presented in the previous section are summarized in figure 5.15. Two linearly copolarized pulses with the same energy density of 2.5 μJ/cm^2 interact with the biexciton state. The data points in columns a,b and c represent the integrated intensity of the biexciton (XX) and of the exciton line (X) respectively, recorded for different fine- (τ_F) and coarse- delays (τ_C). Biexciton- and exciton- emission is recorded simultaneously using a double slit between the first and the second stage of a triple spectrometer in connection with a CCD-matrix. For a coarse delay time of $\tau_C = 0$ ps the plots reflect again the optical interference of the

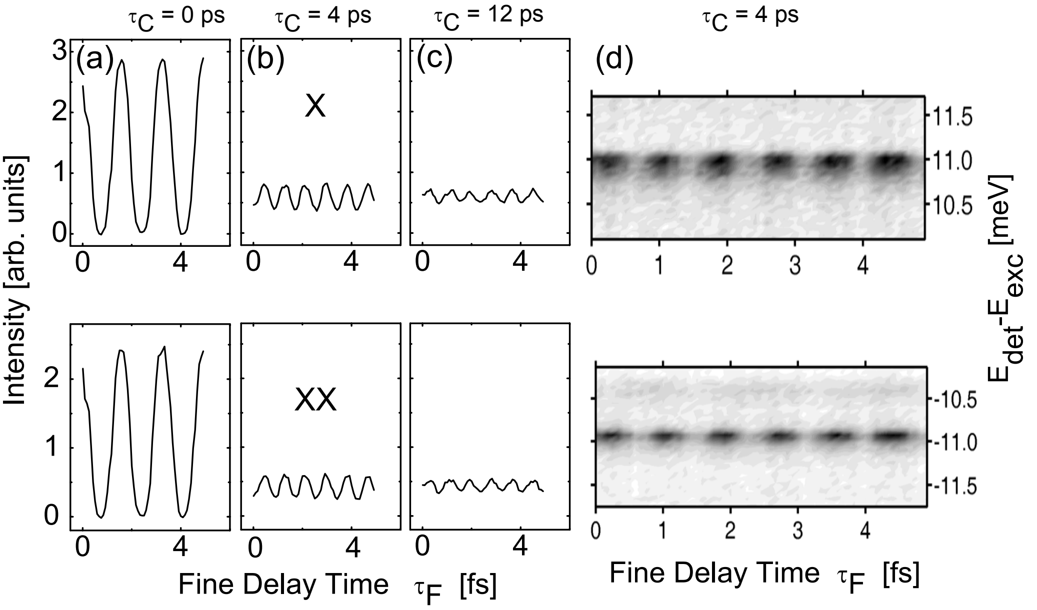

Figure 5.15: Two photon coherent control interferograms for exciton (X) and biexciton (XX) PL from QD#1, for pulses overlapped (column a) and separated in time by 4 ps and 12 ps (column b,c). In column (d) a two-dimensional plot extracted from the measured spectra for $\tau_{\mathrm{C}} = 4$ ps (column b) demonstrates the spectral stability of the lines during the measurement.

two overlapped excitation pulses. In accordance to this, both lines show an oscillation in phase to the excitation laser interference. For non-zero coarse delay times (displayed for $\tau_C = 4$ ps and $\tau_C = 12$ ps), where the two pulses are well separated the behavior changes qualitatively. Both lines X and XX start to oscillate with the double frequency and in addition the in respect to τ_F averaged signal $\bar{I} = (I_+ + I_-)/2$ drops down by a factor of two. Here, the values I_+ and I_- represents the maximum and minimum values of the interferogram extracted by fitting it by a sinus function. In column (d), a two dimensional plot for both lines shows their respective PL distribution as a function of the photon energy as well as the fine delay time τ_F at a fixed coarse delay time $\tau_C = 4$ ps. It is clearly recognized that no measurable long-term energy shift is present during the detection period.

The above interferograms for time delays $\tau = \tau_C + \tau_F$ longer than the pulse duration τ_P result from quantum interference between the wave functions $\Psi(t)$ and $\Psi(t + \tau)$ generated by the first and the second pulse, respectively.

The wave function of a state created by a two-photon excitation process can be written as:

$$\Psi(t) = C_g(t)\,|g\rangle + C_{XX}(t)\,e^{-iE_{XX}t/\hbar}|XX\rangle. \tag{5.17}$$

The amplitude $C_{XX}(t)$ can be determined by second-order time-dependent perturbation theory [88, 90]. If the excitation laser has no spectral components at

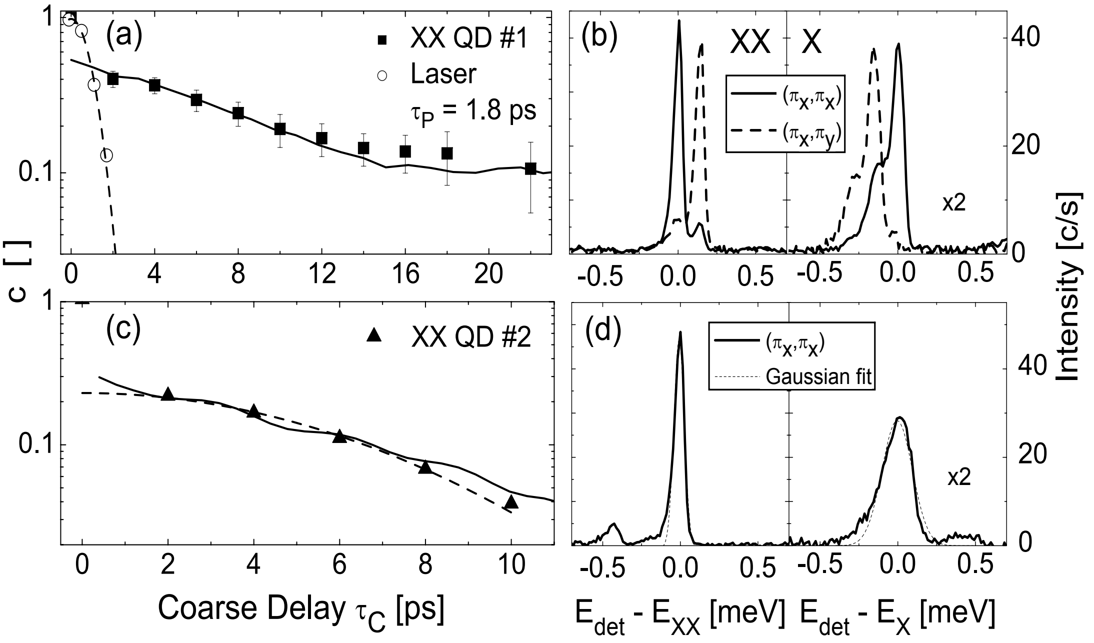

Figure 5.16: Contrast c as a function of the pulse delay τ_{C}, for the biexciton emission of QD#1 (panel a, the same QD as in figure 5.14 and figure 5.15) and QD#2 (panel c). For comparison the autocorrelation function of the excitation pulses is shown as a dashed line. The corresponding PL lines X and XX of QD#1 (panel b) and QD#2 (panel d) are measured with a resolution of 35μeV in the indicated polarization configurations. The solid line in panel (a) is the numerical calculated Fourier transformations of the exciton emission (X) in panel (b) taken the $(\pi_{\mathrm{x}}, \pi_{\mathrm{x}})$ polarization configuration. The dashed lines in panel (d) are fits to a Gaussian distribution. The Fourier transformation of the fit for X in (d) is the solid line in panel (c).

the exciton resonance, it is of the form:

$$C_{XX}(t) \propto Q_{g,XX} \tilde{\mathcal{E}}^2(\omega), \tag{5.18}$$

where $\mathcal{E}^2(\omega)$ is the Fourier transform of the square of the exciting electric field at the two-photon resonance $E_{XX}/2$ and $Q_{g,XX}$ is the two-photon transition matrix element containing contributions from all intermediate exciton states $|X_i\rangle$. It reads like:

$$Q_{g,XX} = \sum_i \frac{\langle XX|H_{\mathrm{D}}|X_i\rangle\langle X_i|H_{\mathrm{D}}|g\rangle}{\hbar(\omega_{x,i} - \omega_{exc})}, \tag{5.19}$$

where H_{D} is the electric dipole moment operator.

The dependence of the occupation of a state after excitation with two phase locked pulses is given by the equations 2.26 and 2.27. In the present case, one can distinguish in the detected biexciton PL signal proportional to the occupation of the biexciton $I(t) \propto \langle \Psi(t,\tau)|\Psi(t,\tau)\rangle$ a non-coherent and a coherent part. The non-coherent contribution is produced by the uncoupled excitation pulses and given by

$$I_{\text{non-coh}} = \langle |C_{XX}(t)|^2 + |C_{XX}(t+\tau)|^2 \rangle. \tag{5.20}$$

Here $\langle ... \rangle$ denotes the time average over the detection period comprising about 10^9 excitation events.

Since the amplitude $C_{\text{XX}}(t+\tau)$ enters the equation 5.20 only by the square of its absolute value, changes of the phase τ especially on the scale of τ_F does not change the value $I_{\text{non-coh}}$. However, changes of the delay on the scale of τ_C have an effect on $I_{\text{non-coh}}$: Due to the quadratic excitation power dependence given by the two-photon process, the in respect to τ_F averaged PL intensity $\bar{I}_{XX-X}$ depends on the temporal overlap of the two excitation pulses. If P is the excitation power of a single excitation pulse, equal for both pulses, then $\bar{I}_{XX-X}$ is for the case of overlapped pulses ($\tau < \tau_P$) of the order $\bar{I}_{XX-X} \approx 4P$. For the case of temporal separated pulses ($\tau > \tau_P$) it is only $\bar{I}_{XX-X} \approx 2P$. This drop of the signal by a factor of two if τ becomes larger than the pulse duration τ_{P} is indeed observed in the data presented in figure 5.15.

The coherent contribution, which depends on τ is given by:

$$I_{coh} = C_{XX}(t)\, C^*_{XX}(t+\tau)\, e^{iE_{XX}\tau/\hbar} \tag{5.21}$$

and oscillates with twice the excitation photon energy $2\hbar\omega_{exc} = E_{XX}$, consistent with the observed scenario. This interference pattern is imprinted in the occupation of the exciton state by the radiative biexciton decay.

Decoherence destroys the interference. Assuming a single biexciton decoherence rate by introducing the homogenous width γ_{XX} in equation 5.21 by the substitution $iE_{XX} \rightarrow iE_{XX} - \gamma_{XX}$, the fringe contrast $c(\tau_C)$ defined by equation 5.15 decays single exponentially with the time constant $\hbar/\gamma_{XX}$. Therefore, the coherent control data contains direct information on the decoherence processes in the biexciton, which is addressed next, after a particularity connected with the two photon excitation process is discussed.

Figure 5.16 summarizes data recorded on two different QDs, where QD#1 is the same as already used in figure 5.15. The interference contrast calculated in accordance with equation 5.15 for different coarse delays τ_C is compared with high resolution spectra of the respective exciton (X) and biexciton (XX) emission line. The contrast $c(\tau_C)$ is identical for the exciton and biexciton signal. However, further examination of the data in figure 5.16 uncovers two surprising findings: First, the decay of the contrast for both QDs is clearly non-exponential in contrast to the expectation of a single decoherence time. Secondly, the time which corresponds to the typical broadening of the biexciton emission should describe the decay of the coherent control contrast. In the present case, the Fourier transformation of the biexciton emission yields a decay which is by a factor of 2..3 slower than the measured contrast decay. Thirdly, if one compares the line widths of the exciton and the biexciton in the high resolution spectra (panel b and d) one finds that the exciton emission line is always broader. Surprisingly, the Fourier transformation of the non-Lorentzian exciton PL line shapes yields time transients that agree rather well with the experimental contrast decay.

The above behavior is remarkable in two ways. It is in contradiction with the fact that the time evolution of the contrast monitors the dephasing of the biexciton state and this should be independent of the broadening (homogenous or inhomogeneous) of the exciton state. Secondly, the broader line width of the exciton emission compared to the biexcitonic one is at the first glance in contradiction with the general expectation. Assuming homogeneous broadening of γ_X and γ_{XX} for the exciton and biexciton state, respectively, the broadening of the biexciton to exciton transition $\gamma_{XX-X} = \gamma_X + \gamma_{XX}$ should always be larger than the width of the exciton to ground state transition of γ_X.

An explanation for the above presented behavior is a inhomogeneous broadening of the exciton and biexciton state, due to fluctuations in the QD environment, e.g. by space charge effects due to off-resonantly created background carriers, leading to fluctuating electro-static fields in the vicinity of the dot. Such fluctuations, as a side effect of the strong optical excitation, needed to drive the TPA process, giving rise to dynamical transition energies via the quantum confined Stark effect [91, 92, 93, 94].

In the spectrally resolved interferograms in panel (d) of figure 5.15 no spectral drift of the emission lines XX and X is observed. This suggests that the fluctuation should appear on a timescale shorter than the typical integration time for a single spectrum of 10..20 s. On the other hand, it was found [95, 96] that these fluctuations change slowly on timescales longer than the biexciton and exciton lifetime so that the QD can go through repeated exciton/biexciton creation and decay cycles.

Let us assume that the fluctuation can be described by a distribution function ρ, which provides the probability to find a specific exciton energy E_X. The function itself is not specified, accept a central energy E_X^0 around E_X is fluctuating with an characteristic bandwidth Γ_X. So the distribution can be written as $\rho\left[\left(E_X - E_X^0\right)/\Gamma_X\right]$. The spectral shape of the PL emission is then a convolution of the homogeneous broadening function for E_X given by a Lorentz function δ with the homogeneous width γ_X and the inhomogeneous distribution function ρ. It can be written as:

$$S_x\left(\hbar\omega\right) = \int \rho\left[\left(E_X - E_X^0\right)/\Gamma_X\right] \delta\left(E_X - \hbar\omega, \gamma_X\right) dE_X \tag{5.22}$$

In the case that the homogeneous width is smaller than the inhomogeneous distribution $\gamma_X \ll \Gamma_X$ the width of the PL emission of the exciton is directly given by ρ and Γ_X.

For the biexciton and its emission ($E_{XX-X} = E_{XX} - E_X$) this fluctuation of the interaction energy has to be accounted as well. A good approximation is that E_{XX}^B is in lowest order a linear function of E_X with a slope $Q > 0$ [96]. This mainly means, that the external field leads to a shift of E_X and E_{XX}, which goes in the same direction for the exciton and the biexciton, however with different amplitudes. Taking the convolution of the distribution ρ for X and XX, this yields an inhomogeneous width for the $XX \rightarrow X$ transition of $\Gamma_{XX-X} = (1-Q)\,\Gamma_X$, being indeed smaller than for the exciton PL emission line. This is at variance with static inhomogeneous broadening, where the width of the biexciton emission is always larger than the exciton emission as demonstrated in [97, 98]. Inspecting the line width of the exciton and biexciton emission from several QDs, Q was found to be in the range of 0.4...0.7. As for the exciton, here it is also assumed that the homogeneous width of the biexciton is smaller than this inhomogeneous jittering $\gamma_{XX} \ll \Gamma_{XX}$. As a result of these considerations, the narrow emission line width is different from $\gamma_{XX}+\gamma_X$ and is therefore not comparable to the decay constant of the coherent control contrast as seen in the data of figure 5.16. How this fluctuation influences the decay in detail is addressed next.

The energy of the biexciton state is given by $E_{XX} = 2E_X - E_{XX}^B = (2-Q)\,E_X$ taking into account the previously discussed assumption of $E_{XX}^B \propto QE_X$. This leads to a broadening of the biexciton state of $\Gamma_{XX} = (2-Q)\,\Gamma_X$, which yields a jittering in the control phase $\phi_{XX} = \left(2E_X - E_{XX}^B\right)\tau/\hbar$ in a coherent control experiment. The coherent control intensity as a function of the delay τ between the two pulses averaged over a large number of excitation events is given by equation 5.21 convoluted with the inhomogeneous distribution ρ. It reads:

$$\bar{I}\,(\tau) = \int_{-\infty}^{\infty} \rho\left(\frac{E_X - E_X^0}{\Gamma_X}\right) \exp\left[\left(-i\,(2-Q)\,\frac{E_X}{\hbar} - \gamma_{XX}\right)\tau\right] dE_X. \tag{5.23}$$

Rewriting equation 5.23 and defining $u := \left(E_X - E_X^0\right)/\Gamma_X$ it follows:

$$\bar{I}\,(\tau) \propto \exp\left[\left(-\frac{iE_{XX}^0}{\hbar} - \gamma_{XX}\right)\tau\right] \int_{-\infty}^{\infty} \rho\,(u) \exp\left(-\frac{i\,(2-Q)\,\Gamma_X}{\hbar}\,u\tau\right) du. \tag{5.24}$$

While the first exponential function in equation 5.24 represents an oscillation, homogeneously damped with a time constant $1/\gamma_{XX}$, the integral defines a Fourier transformation of $\rho\,(u)$ with signal decay. The Fourier integral can be worked out without an assumption about the shape of ρ. Doing this and using in addition the approximation for $\gamma_{XX} \ll (2-Q)\,\Gamma_X$, the equation 5.24 reads:

$$\bar{I}\,(\tau) \propto \exp\left[-\frac{iE_{XX}^0}{\hbar}\,\tau\right] \tilde{\rho}\left(\frac{(2-Q)\,\Gamma_X}{\hbar}\tau\right) \tag{5.25}$$

One can now use equation 5.25 to calculate the contrast $c\,(\tau_C)$ at different coarse delay times τ_C. In accordance with equation 5.15 the contrast is given by the ratio of the oscillation amplitude in equation 5.25 and the constant background given by $I_{non-coh}$ (equation 5.20). So it is:

$$c\,(\tau_C) \propto \tilde{\rho}\left(\frac{(2-Q)\,\Gamma_X}{\hbar}\tau\right). \tag{5.26}$$

To illustrate the above considerations one can compare them with the data in figure 5.16.

As already stated above, the observed contrast decay for both QDs is non-exponential. For QD#1 the spectral shape of the exciton emission for each of the components π_X and π_Y consists of two gaussian like distributions. The Fourier transformation of the component π_X fits well the time evolution of the coherent control contrast (panel (a)). For QD#2 the exciton emission (panel (d)) can be in good approximation fitted by using a single gaussian distribution for ρ_X with a spectral width of 230 μeV (FWHM) corresponding to 18 ps in the time domain. Remembering that the Fourier transformation of a Gaussian distribution $\rho_X(u) = \exp(-u^2)$ yields a Gaussian contrast decay in the time domain, the contrast decay for QD#2 is fitted with a Gaussian decay resulting in a time of 12 ps (FWHM). For comparison, for the QD#2 in panel (c) also the Fourier transformed spectral distribution of the exciton emission is plotted (dashed line), comparing also well with the contrast decay. So, for both QDs the shape of the contrast decay is well reproduced within a certain accuracy by the Fourier transformation of the spectral distribution of the exciton emission in accordance with equation 5.26. This finding means that Q is close to one, however not exactly and the broadening of the biexciton state can be approximated by the broadening of the exciton state. The fact that the distributions of the exciton emission for QD#1 and QD#2 are clearly different (monomodal and bimodal shape) means that the charge distributions are possibly different for different QDs.

Since the inhomogeneous broadening of the total biexciton energy enters the two photon control, the contrast decay is governed by this inhomogeneous part, despite of a narrow PL width of the transition $XX \to X$. As the central result of this experiment, the interference disappears on a 10 ps time scale, much shorter than the intrinsic coherence loss.

In addition it is necessary to mention that for the spectral width of the biexciton emission $XX \to X$ in the experiments a value of 70..80μeV was observed[3]. Currently it is not clear which part of this width is still due to inhomogeneous broadening. The observed width is markedly larger than is expected for a homogeneous broadening of the biexciton state which has a lifetime of 200..300 ps [95, 99] corresponding to a spectral width below 2μeV. Also time resolved degenerated four wave mixing measurements on III-V QD ensembles at low temperatures yielded a width below 10μeV [100]. In general, the observed broadening of the biexciton emission line supports the above consideration that Q is close to one.

5.3.4 Coherent control of biexciton states versus excitation energy

The two photon coherent control data in the preceding section was collected with an excitation energy exactly centered between the energies of the exciton and biexciton emission, so that the energy conservation $2E_{\mathrm{exc}} = 2E_{\mathrm{X}} - E_{\mathrm{XX}}^{\mathrm{B}}$ was fulfilled. In the present section it will be discussed what happens if the laser energy is slightly different from this center energy. As stated above the coherent control experiments are done with ps excitation, where the laser has a spectral half width of $\hbar\omega_{\mathrm{exc}} = 1.8$ meV. In figure 5.17 it is summarized what happens

---

[3] Spectral resolution of the detection system was 35μeV.

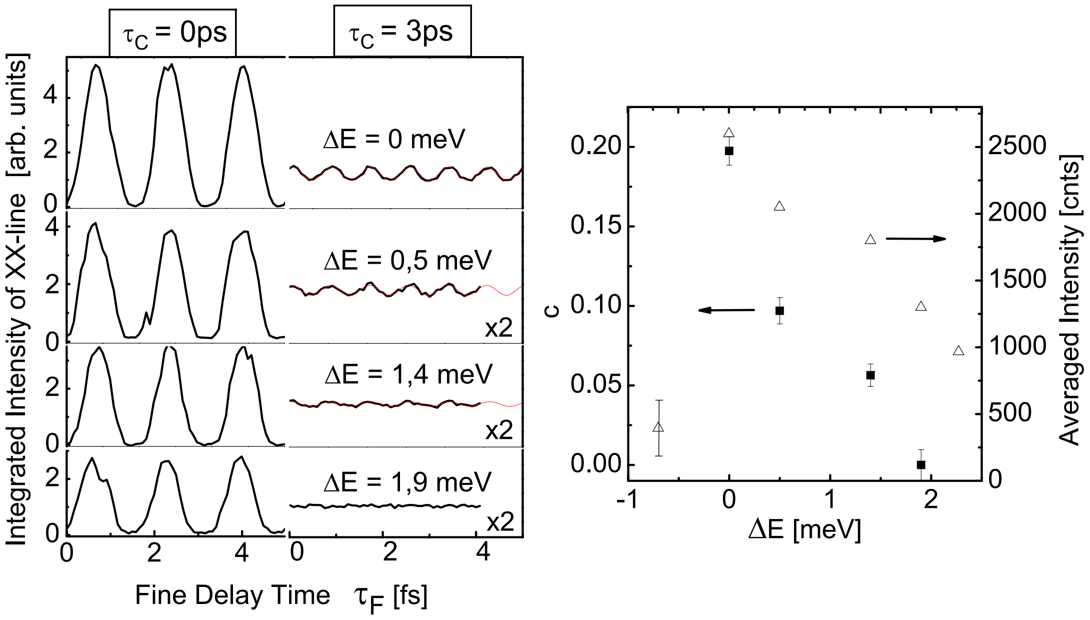

Figure 5.17: Left side: Two photon coherent control interferograms for the biexciton PL of QD#2 for pulses overlapped (τ_C = 0ps) and pulses separated in time (τ_C = 3ps) at different excitation energies. Right side: Contrast c for τ_C = 3ps delay versus excitation energy (solid squares) and the corresponding yield of the biexciton line (empty triangles).

if this excitation laser is tuned in steps of a quarter of its half width out of the center to higher energies. On the left side, interferograms for four different excitation energies are summarized, for the case if both pulses are overlapped ($\tau_C = 0$ ps) and if both pulses are well separated in time ($\tau_C = 3$ ps). For the interferograms the signal of the biexciton and exciton emission is integrated for each single interferogram point. On the right side, the corresponding contrast $c\,(\tau_C = 3$ ps) as well as the averaged intensity[4] is plotted versus excitation energy.

As one can see, if the excitation laser is tuned by more than one half width to higher energies, the coherent control oscillations disappear totally while the intensity is only reduced by nearly a factor of two. For comparison, if the excitation laser is tuned to the low energy side, already a detuning of 1 meV is enough to reduce the emission intensity to a not evaluable value, where no oscillations can be determined.

The left plot in the figure shows that if the excitation laser is above the center energy, biexcitons can still be created but the phase memory is more and more lost with larger detuning ΔE demonstrated by the fast reduction of the coherent control contrast. A possible explanation for this can be the involvement of acoustical phonons. In general, if the excitation energy is tuned out of the center energy $E_X - E_{XX}^B/2$ the energy conservation is not exactly fulfilled.

---

[4] The averaged intensity is calculated by integrating the interferogram for $\tau_C = 3$ ps and dividing by the number of data points.

The emission of one or more acoustical phonons can solve this problem as it is the case for single photon excitation of the exciton state demonstrated by the PLE spectra in section 4.3. However, in this case the phase relation between the exciting light field and the created biexciton subwave functions is lost with the number of acoustical phonons which are involved, which yields a smaller initial coherent control contrast.

Chapter 6

Summary

In this thesis two kinds of decoherence in a single CdSe QD are investigated. For the case of quantum coherence the phase memory between the two states of the ground state exciton are measured. These states are different spin states where the degeneracy is lifted by electron hole exchange interaction if the QD has a in-plane anisotropy. By the observation of quantum beats it was carried out that the dephasing between these two states is slower than its radiative lifetime.

For the same kind of QDs the optical coherence is also investigated. Single photon coherent control on the excited state of an exciton as well as two photon coherent control on the biexciton state is performed. For the excited state of the exciton an optical coherence time of 6 ps is determined. In case of the biexciton, the decay of the coherent control contrast is governed by an inhomogeneous decay due to a jittering of the biexciton energy. This is caused by fluctuating charges in the QD environment giving rise to variable transition energies due to the quantum confined Stark effect. So, as a result, the observed contrast decay provides a lower limit for the optical dephasing time of the biexciton in the range of 10 ps.

The above findings demonstrate that the quantum states in a single dot are partly well separated from influences of the environment. Especially, scattering processes which lead to different phase shifts for two different states in the same QD are very improbable as demonstrated by the quantum beat experiment. A coherent control experiment probes the phase memory on a more external time scale. Any discontinuity of the phase for a single state will result in a drop down of the measured contrast. By this reason it was already mentioned in the introduction that the optical coherence time, which is measured by the coherent control experiment, can be in general shorter than the quantum coherence times. This is what in principle is observed here. While the coherent control data on a biexciton provides only a lower limit for its optical dephasing time on a 10 ps timescale, for the excited state a slightly shorter time on the sub 10 ps timescale was found. This suggests that most of the scattering processes interacting with the states in a QD create nearly the same phase changes for the different states. This can be important for applications where different QDs are coupled to each other and a certain phase relation between their states is needed.

In a second complex of investigations the spin memory of a single carrier was determined. Here the spin state of a single hole was directly accessible with optical methods since negatively charged QDs are present in the sample. Here the total momentum in the trion ground state is given by the spin state of the hole. The low temperature longitudinal spin relaxation in the degenerated hole doublet exhibits a component with a time constant longer than 10 ns. This is as well as the above coherence properties a consequence of the large separations between the discrete energy levels in QDs reducing strongly the band mixing.

While the experiments carried out that phase- and spin- memory times in the ground state of a QD can be rather long it was also found that the involvement of higher states give rise to a fast additional loss of such memory. This is directly demonstrated if the ground state is quasi resonantly excited via the 1-LO-phonon band. In this case the first excited state, which is a light hole state, is close to the excitation energy. This results in a fast initial loss of linear polarization in case of an exciton or an incomplete spin imprint in case of the trion ground state.

In general, the results of this work support the expectation in the introduction that single QDs are interesting candidates for quantum information processing. The long phase memory of the ground state exciton enables a large number of quantum operations if fs-laser sources are used. The long spin memory in connection with the good accessibility of the spin states by optical methods makes these structures interesting for information storage devices.

In the near future new impetus for the research can be given by the coupling of different QDs or the usage of different states in one QD (e.g. biexciton, exciton, and crystal ground state) in order to implement conditional quantum operations and go a step ahead to quantum information processing with these QD structures. In the field of basic research in sense of single dot spectroscopy there remain still interesting questions. What is the optical coherence time of the ground exciton and how does it depend on the excitation condition? Is it possible to determine the optical coherence of the biexciton more exactly?

In general, the found coherence properties of single QDs in connection with the above considerations show that many other interesting quantum optical experiments are possible on these man made 'atoms'.

Appendix A

Trion wave functions including hh-lh-mixing

In this appendix the trion wave functions including hh-lh-mixing are derived. Since the heavy-hole and the light-hole band are well separated, the trion wave functions are discussed in sense of perturbation theory.

The Luttinger hamiltonian describing the band structure of the top valence band in the basis of the spin functions $(|+3/2\rangle, |+1/2\rangle, |-1/2\rangle, |-3/2\rangle)$ can be written in the matrix form [41]:

$$H = \begin{pmatrix} F & S & I & 0 \\ S^* & G & 0 & I \\ I^* & 0 & G & -S \\ 0 & I^* & -S^* & F \end{pmatrix} \tag{A.1}$$

where the following abbreviations are used:

$$\begin{array}{rlcrl} F = & -Ak^2 - \frac{B}{2}\left(k^2 - 3k_{\mathrm{z}}^2\right) & , & G = & -Ak^2 + \frac{B}{2}\left(k^2 - 3k_{\mathrm{z}}^2\right) \\ S = & Dk_{\mathrm{z}}\left(k_{\mathrm{x}} - ik_{\mathrm{y}}\right) & , & I = & \frac{\sqrt{3}}{2}B\left(k_{\mathrm{x}}^2 - k_{\mathrm{y}}^2\right) - iDk_{\mathrm{x}}k_{\mathrm{y}} \end{array} \tag{A.2}$$

$$A = -\frac{\hbar^2}{2m}\gamma_1 \quad , \quad B = -\frac{\hbar^2}{m}\gamma_2 \quad , \quad D = -\sqrt{3}\frac{\hbar^2}{m}\gamma_3$$

Where γ_1, γ_2 and γ_3 are the so called Luttinger parameters.

Since the energy separation between the heavy- and the light-hole bands is large against the heavy-hole light-hole coupling energy, one can decompose the hamiltonian A.1 into a diagonal part with an non-diagonal perturbation:

$$H = H_{\mathrm{D}} + V = \begin{pmatrix} F & 0 & 0 & 0 \\ 0 & G & 0 & 0 \\ 0 & 0 & G & 0 \\ 0 & 0 & 0 & F \end{pmatrix} + \begin{pmatrix} 0 & S & I & 0 \\ S^* & 0 & 0 & I \\ I^* & 0 & 0 & -S \\ 0 & I^* & -S^* & 0 \end{pmatrix} \tag{A.3}$$

In this case the heavy-hole wave function can be written in first order perturbation theory as:

$$\Psi_\pm = \varphi_0^{\mathrm{hh}} \left|\pm\frac{3}{2}\right\rangle + \sum_{\mathrm{j}=\pm\frac{1}{2}} \sum_{\mathrm{n}=0}^{\infty} \frac{\left\langle \varphi_{\mathrm{n}}^{\mathrm{lh}} | V_{\mathrm{j},\pm\frac{3}{2}} | \varphi_0^{\mathrm{hh}} \right\rangle}{E_0^{\mathrm{hh}} - E_{\mathrm{n}}^{\mathrm{lh}}} \varphi_{\mathrm{n}}^{\mathrm{lh}} |j\rangle. \tag{A.4}$$

Limiting only to states with $n = 0$ this leads to:

$$\begin{pmatrix} \Psi_+ \\ \Psi_- \end{pmatrix} = \varphi_0^{\mathrm{hh}} \begin{pmatrix} \left|+\frac{3}{2}\right\rangle \\ \left|-\frac{3}{2}\right\rangle \end{pmatrix} - \frac{\varphi_0^{\mathrm{lh}}}{\Delta} \begin{pmatrix} I\left|-\frac{1}{2}\right\rangle + S\left|+\frac{1}{2}\right\rangle \\ I^*\left|+\frac{1}{2}\right\rangle - S^*\left|-\frac{1}{2}\right\rangle \end{pmatrix}. \tag{A.5}$$

Writing the abbreviations S and I more compactly and transformed into the real space leads to:

$$S = \sqrt{3}\,\frac{\hbar^2}{m}\,\gamma_3\,\frac{\partial}{\partial z}\left(\frac{\partial}{\partial x} - i\frac{\partial}{\partial y}\right) \tag{A.6}$$

with odd in-plane parity and for I:

$$\begin{aligned} I &= \sqrt{3}\,\frac{\hbar^2}{2m}\left[\gamma_2\left(-\frac{\partial^2}{\partial x^2} + \frac{\partial^2}{\partial y^2}\right) + 2i\gamma_3\frac{\partial}{\partial x}\frac{\partial}{\partial y}\right] && \text{(A.7)} \\ &= \sqrt{3}\,\frac{\hbar^2}{2m}\,\gamma_3\,\left(\frac{\partial}{\partial y} + i\frac{\partial}{\partial x}\right)^2 && \text{(A.8)} \end{aligned}$$

which is of even in-plane parity. Note: in the last step it is assumed that $\gamma_2 \approx \gamma_3$ which corresponds to a spherical approximation.

Appendix B

Definition of the spin relaxation time

In section 2.5.3 the occupation difference decay time $T_1^{'}$ is introduced and in chapter 5.2 such kind of time is used as $T_{1,h}^{'}$ to describe the change in the occupation $n_\pm$ of the trion spin states $|\pm 3/2\rangle$. In the following, the influence of the definition for this time on the rate equations for the occupation of the single states n_+ and n_- will be worked out and the factor 2 in the rate equations 5.9 will be verified.

The spin relaxation time $T_{1,h}^{'}$ is defined by the decay of the spin orientation [19] which can be written as:

$$\frac{dS}{dt} = -\frac{S}{T_{1,\mathrm{h}}^{'}}. \tag{B.1}$$

Here S is the total spin of the system given by:

$$S = \frac{3}{2}\frac{(n_+ - n_-)}{(n_+ + n_-)} = \frac{3}{2n}(n_+ - n_-) \tag{B.2}$$

where $n = n_+ + n_-$ is the total occupation in the state $|\pm 3/2\rangle$. Introducing B.2 into B.1 yields:

$$\frac{dS}{dt} = \frac{3}{2n}(\dot{n}_+ - \dot{n}_-) = -\frac{3}{2n}\frac{(n_+ - n_-)}{T_{1,\mathrm{h}}^{'}}. \tag{B.3}$$

The equation B.3 can be compared with the rate equations for the occupations of the single states using a characteristic time τ_{SF} for the spin flip between the two states. Assuming infinite long lifetime and an initial occupation for n_+ and n_- without any further generation it is:

$$\dot{n}_+ = -\frac{n_+}{\tau_{\mathrm{SF}}} + \frac{n_-}{\tau_{\mathrm{SF}}} \qquad \dot{n}_- = +\frac{n_+}{\tau_{\mathrm{SF}}} - \frac{n_-}{\tau_{\mathrm{SF}}} \tag{B.4}$$

and subtracting both equations from each other yields:

$$(\dot{n}_+ - \dot{n}_-) = -2\frac{(n_+ - n_-)}{\tau_{\mathrm{SF}}} \tag{B.5}$$

Comparing B.3 with B.5 yields:

$$\frac{(n_+ - n_-)}{2T^{'}_{1,\mathrm{h}}} = \frac{(n_+ - n_-)}{\tau_{\mathrm{SF}}} \tag{B.6}$$

which explains the additional factor of 2 in the rate equation 5.9. Due to the definition of the spin relaxation time $T^{'}_{1,\mathrm{h}}$ by B.1 the factor 2 appears in a rate equation for the single occupations n_+ or n_-.

Appendix C

Abbreviations, Variables, and Constants

list of abbreviations

DOS	density of states
QD	quantum dot
QW	quantum well
TR-FWM	time resolved four wave mixing
TI	time integrated
PL	photo luminescence
PLE	photo luminescence excitation
μPL	micro photo luminescence
GT	Glan-Thomson polarizer
OMA	optical multichannel analyzer
PMT	photo multiplier tube
MCP-PMT	multi channel plate photo multiplier tube
CCD	charge coupled device
NA	numerical aperture
SHG	second harmonic generation
THG	third harmonic generation
SFG	sum frequency generation
OPO	optical parametric oscillator
BBO	β Bariumborat
SPC	single photon counting
TCSPC	time correlated SPC
CW	continuous wave
TPA	two photon absorption
AFM	atomic force microscopy
SEM	scanning electron microscopy

used variables:

τ_{C},τ_{F}	coarse and fine delay time
τ_{P}	laser pulse length
$T_1^{'}$	population difference decay time between two states
$T_{1,\mathrm{h}}^{'}$	spin relaxation time for the heavy hole
T_1	population average level decay time for two states coupled to a common ground state
T_2	total phase relaxation time
$T_2^{'}$	pure phase relaxation time
J_{z}	angular momentum projection in z direction
$S_{\mathrm{e,z}}$	electron spin projection in z direction
$\vert X\rangle$,$\vert Y\rangle$	exciton states
$\vert XX\rangle$	biexciton state
E_{x},E_{y},E_{xx}	Eigenenergy of a state (here x and y)
Δ_0	
Δ_1,Δ_2	
ρ	density matrix operator
$\mathcal{H}_{\mathrm{eh}}$	electron-hole exchange interaction operator
$\mathcal{H}_{\mathrm{Zeeman}}$	Zeeman interaction operator
$\mathbf{B} = (B_{\mathrm{x}}, B_{\mathrm{y}}, B_{\mathrm{y}})$	external magnetic field
$g_{\mathrm{e},\Vert}$,$g_{\mathrm{e},\perp}$,$g_{\mathrm{e,i}}$	electron g-factor parallel to z axis, in the x-y plane, or in direction $i \in \{x, y, z\}$
$g_{\mathrm{h},\Vert}$,$g_{\mathrm{h},\perp}$,$g_{\mathrm{h,i}}$	heavy hole g-factor parallel to z axis, in the $x-y$ plane, or general in direction $i \in \{x, y, z\}$
ω	circular frequency
γ	homogeneous broadening
Γ	inhomogeneous broadening
$I(\omega)$,$I(t)$	intensity in spectral or time domain
N_{x}	population of a state $\vert X\rangle$

Fundamental physical constants: (in accordance with the recommendations of CODATA)

e, e_0	$= 1.60217653 \cdot 10^{-19}\ C$	elementary charge
μ_{B}	$= 9,27400949 \cdot 10^{-24}\ J/T$ $= 5.78838180 \cdot 10^{-2}\ meV/T$	Bohr magneton
$\hbar = h/(2\pi)$	$= 1.05457168 \cdot 10^{-34}\ J \cdot s$ $= 658.21191\ \mu eV \cdot ps$	Planck's constant
k_{B}	$= 1,3806505 \cdot 10^{-23}\ J/K$ $= 86.173432\ \mu eV/K$	Boltzmann constant

Bibliography

[1] P. Benioff. Quantum mechanical hamiltonian models of turing machines. *J. Stat. Phys.*, **29**:515, 1982.

[2] R. F. Feynman. Quantum mechanical computers. *Opt. News*, **11**:11, 1985.

[3] D. Bouwmeester, A. Ekert, and A. Zeilinger. *The Physics of Quantum Information.* Springer, Berlin, 2000.

[4] D. Deutsch and R. Jozsa. Rapid solution of problems by quantum computation. *Proc. R. Soc. London Ser. A*, **439**:554, 1992.

[5] D. Gammon and D. G. Steel. Optical studies of single quantum dots. *Physics Today*, **55**(10):36, 2002.

[6] L. Schultheis, J. Kuhl, A. Honold, and C. W. Tu. Ultrafast phase relaxation of excitons via exciton-exciton and exciton-electron collisions. *Phys. Rev. Lett.*, **57**:1635, 1986.

[7] E. O. Göbel, K. Leo, T. C. Damen, J. Shah, S. Schmitt-Rink, W. Schäfer, J. F. Müller, and K. Köhler. Quantum beats of excitons in quantum wells. *Phys. Rev. Lett.*, **64**:1801, 1990.

[8] A. Honold, L. Schultheis, J. Kuhl, and C. W. Tu. Collision broadening of two-dimensional excitons in a GaAs single quantum well. *Phys. Rev. B*, **40**:6442, 1989.

[9] G. Noll, U. Siegner, S. G. Shevel, and E. O. Göbel. Picosecond stimulated photon echo due to intrinsic excitations in semiconductor mixed crystals. *Phys. Rev. Lett*, **64**:792, 1990.

[10] A. P. Heberle, J. J. Baumberg, and K. Köhler. Ultrafast coherent control and destruction of excitons in quantum wells. *Phys. Rev. Lett.*, **75**:2598, 1995.

[11] V. Langer, H. Stolz, and W. von der Osten. Observation of quantum beats in the resonance fluorescence of free excitons. *Phys. Rev. Lett.*, **64**:854, 1990.

[12] L. Schultheis, M. D. Sturge, and J. Hegarty. Photon echoes from two-dimensional excitons in GaAs-AlGaAs quantum wells. *Appl. Rev. Lett.*, **47**:995, 1985.

[13] S. Bar-Ad and I. Bar-Joseph. Absorption quantum beats of magnetoexcitons in GaAs heterostructures. *Phys. Rev. Lett.*, **66**:2491, 1991.

[14] N. H. Bonadeo, J. Erland, D. Gammon, D. Park, D. S. Katzer, and D. G. Steel. Coherent optical control of the quantum states of a single quantum dot. *Sience*, **282**:1473, 1998.

[15] M. Paillard, X. Marie, P. Renucci, T. Amand, A. Jbeli, and J. M. Gérard. Spin relaxation quenching in semiconductor quantum dots. *Phys. Rev. Lett.*, **86**:1634, 2001.

[16] M. Scheibner, G. Bacher, S. Weber, A. Forchel, Th. Passow, and D. Hommel. Polarization dynamics in self-assembled CdSe/ZnSe quantum dots: The role of excess energy. *Phys. Rev. B*, **67**:153302, 2003.

[17] J. A. Gupta, D. D. Awschalom, Al. L. Efros, and A. V. Rodina. Spin dynamics in semiconductor nanocrystals. *Phys. Rev. B*, **66**:125307, 2002.

[18] S. Cortez, O. Krebs, S. Laurent, M. Senes, X. Marie, R. Voisin, R. Ferreira, G. Bastard, J.M. Gérard, and T. Amand. Optically driven spin memory in n-doped InAs-GaAs quantum dots. *Phys. Rev. Lett.*, **89**:207401, 2002.

[19] F. Meier and B. P. Zakharchenya. *Optical Orientation.* NORTH-HOLLAND, Amsterdam, 1984.

[20] L. Viña. Spin relaxation in low-dimensional systems. *J. Phys.: condens. Matter*, **11**:5929, 1999.

[21] L. Schultheis, J. Kuhl, and A. Honold. Picosecond phase coherence and orientational relaxation of excitons in GaAs. *Phys. Rev. Lett.*, **57**:1797, 1986.

[22] J. Hegarty. Enhanced inelastic scattering and localization of excitons in $In_{0.53}Ga_{0.47}As$/InP alloy quantum wells. *Phys. Rev. B*, **38**:7843, 1988.

[23] L. Schultheis, A. Honold, J. Kuhl, K. Köhler, and C. W. Tu. Optical dephasing of homogeneously broadened two-dimensional exciton transitions in GaAs quantum wells. *Phys. Rev. B*, **34**:9027, 1986.

[24] L. Schultheis, A. Honold, J. Kuhl, K. Köhler, and C. W. Tu. Phase coherence and line broadening of free excitons in gaas quantum wells. *Superlattices and Microstructures*, **2**:441, 1986.

[25] M. D. Webb, S. T. Cundiff, and D. G. Steel. Stimulated-picosecond-photon-echo studies of localized exciton relaxation and dephasing in GaAs/$Al_xGa_{1-x}As$ multiple quantum wells. *Phys. Rev. B*, **43**:12658, 1991.

[26] M. D. Webb, S. T. Cundiff, and D. G. Steel. Observation of time-resolved picosecond stimulated photon echoes and free polarization decay in GaAs/AlGaAs multiple quantum wells. *Phys. Rev. Lett.*, **66**:934, 1991.

[27] P. Borri, W. Langbein, S. Schneider, U. Woggon, R. L. Sellin, D. Ouyang, and D. Bimberg. Ultralong dephasing time in InGaAs quantum dots. *Phys. Rev. Lett.*, **87**:157401, 2001.

[28] D. Birkedal, K. Leosson, and J. M. Hvam. Long lived coherence in self-assembled quantum dots. *Phys. Rev. Lett.*, **87**:227401, 2001.

[29] M. Shapiro, J. W. Hepburn, and P. Bumer. Simplified laser control of unimolecular reactions. *Chem. Phys. Lett.*, **149**:451, 1988.

[30] L. D. Noordam, D. I. Duncan, and T. F. Gallagher. Ramsey fringes in atomic rydberg wave packets. *Phys. Rev. A*, **45**:4734, 1992.

[31] J. F. Christian et al. Rubidium electronic wave packets probed by a phase-sensitive pump-probe technique. *Opt. Commun.*, **103**:79, 1993.

[32] B. Broers, J. F. Christian, J. H. Hoogenraad, W. J. van der Zande, H. B. van Linden van den Heuvell, and L. D. Noordam. Time-resolved dynamics of electronic wave packets above the classical field-ionization threshold. *Phys. Rev. Lett.*, **71**:344, 1993.

[33] L. Marmet, H. Held, G. Raithel, J. A. Yeazell, and H. Walther. Observation of quasi-landau wave packets. *Phys. Rev. Lett.*, **72**:3779, 1994.

[34] I. Brener, P. C. M. Planken, M. C. Nuss, L. Pfeiffer, D. E. Learid, and A. M. Weiner. Repetitive excitation of charge oscillations in semiconductor heterostructures. *Appl. Phys. Lett.*, **63**:2213, 1993.

[35] P. C. M. Planken, I. Brener, M. C. Nuss, M. S. C. Luo, and S. L. Chuang. Coherent control of terahertz charge oscillations in a coupled quantum well using phase-locked optical pulses. *Phys. Rev. B*, **48**:4903, 1993.

[36] Y. Toda, T. Sugimoto, M. Nishioka, and Y. Arakawa. Near-field coherent excitation spectroscopy of InGaAs/GaAs self-assembled quantum dots. *Appl. Phys. Lett.*, **76**:3887, 2000.

[37] L. Besombes, J. J. Baumberg, and J. Motohisa. Coherent spectroscopy of optically gated charged single InGaAs quantum dots. *Phys. Rev. Lett.*, **90**:257402, 2003.

[38] E. Biolatti, R. C. Iotti, P. Zanardi, and F. Rossi. Quantum information processing with semiconductor macroatoms. *Phys. Rev. Lett.*, **85**:5647, 2000.

[39] P. Chen, C. Piermarocchi, and L. J. Sham. Control of exciton dynamics in nanodots for quantum operations. *Phys. Rev. Lett.*, **87**:067401, 2001.

[40] G. Chen, T. H. Stievater, E. T. Batteh, X. Li, D. G. Steel, D. Gammon, D. S. Katzer, D. Park, and L. J. Sham. Biexciton quantum coherence in a single quantum dot. *Phys. Rev. Lett.*, **88**:117901, 2002.

[41] E. L. Ivchenko and G. Pikus. *Superlattices and Other Heterostructures.* Springer, Berlin, 1997.

[42] D. Gammon, E. S. Snow, B. V. Shanabrook, D. S. Katzer, and D. Park. Fine structure splitting in the optical spectra of single GaAs quantum dots. *Phys. Rev. Lett.*, **76**:3005, 1996.

[43] V. D. Kulakovskii, G. Bacher, R. Weigand, T. Kümmell, A. Forchel, E. Borovitskaya, K Leonardi, and D. Hommel. Fine structure of biexciton emission in symmetric and asymmetric CdSe/ZnSe single quantum dots. *Phys. Rev. Lett*, **82**:1780, 1999.

[44] M. Bayer, G. Ortner, O. Stern, A. Kuther, A. A. Gorbunov, A. Forchel, P. Hawrylak, S. Fafard, K. Hinzer, T. L. Reinecke, S. N. Walck, J. P. Reithmaier, F. Klopf, and F. Schäfer. Fine structure of neutral and charged excitons in self-assembled In(Ga)As/(Al)GaAs quantum dots. *Phys. Rev. B*, **65**:195315, 2002.

[45] A. Hartmann, Y. Ducommun, E. Kapon, U. Hohenester, and E. Molinari. Few-particle effects in semiconductor quantum dots: Observation of multicharged excitons. *Phys. Rev. Letts.*, **84**:5648, 2000.

[46] J. Finley, W. Fry, A.D. Ashmore, A. Lematre, A.I. Tartakovskii, R. Oulton, D.J. Mowbray, M.S. Skolnick, M. Hopkinson, P.D. Buckle, and P.A. Maksym. Observation of multicharged excitons and biexcitons in a single InGaAs quantum dot. *Phys. Rev. B*, **63**:161305, 2001.

[47] V. Türck, S. Rodt, R. Heitz, O. Stier, M. Strassburg, U.W. Pohl, and D. Bimberg. Charged excitons and biexcitons in self-organized CdSe quantum dots. *Phys. Status Solidi B*, **224**:217, 2001.

[48] J.G. Tischler, A.S. Bracker, D. Gammon, and D. Park. Fine structure of trions and excitons in single GaAs quantum dots. *Phys. Rev. B*, **66**:081310, 2002.

[49] I. A. Akimov, A. Hundt, T. Flissikowski, and F. Henneberger. Fine structure of the trion triplet state in a single self-assembled semiconductor quantum dot. *Appl. Phys. Lett.*, **81**:4730, 2002.

[50] W. Demtröder. *Laser Spectroscopy.* Springer, Berlin, 1996.

[51] X. Marie, P. Le Jeune, T. Amand, M. Brousseau, J. Barrau, and M. Paillard. Coherent control of the optical orientation of excitons in quantum wells. *Phys. Rev. Lett.*, **79**:3222, 1997.

[52] S. Koizumi, M. Kamo, Y. Sato, H. Ozaki, and T. Inuzuka. Growth and characterization of phosphorous doped 111 homoepitaxial diamond thin films. *Appl. Phys. Lett.*, **71**:1065, 1997.

[53] D. Litvinov, A. Rosenauer, D. Gerthsen, P. Kratzert, M. Rabe, and F. Henneberger. Influence of the growth procedure on the Cd distribution in CdSe/ZnSe heterostructures: Stranski-krastanov versus two-dimensional islands. *Appl. Phys. Lett.*, **81**:640, 2002.

[54] P. Kratzert. *Molekularstrahlepitaxie von II-VI Quantenpunkten.* PhD thesis, Institut für Physik, Humboldt-Universität zu Berlin, 2002.

[55] F. Gindele, U. Woggon, W. Langbein, J. M. Hvam, K. Leonardi, D. Hommel, and H. Selke. Excitons, biexcitons, and phonons in ultrathin CdSe/ZnSe quantum structures. *Phys. Rev. B.*, **60**:8773, 1999.

[56] M. Nirmal et al. Observation of the 'dark exciton' in CdSe quantum dots. *Phys. Rev. Lett.*, **75**:3728, 1995.

[57] U. Woggon et al. Exchange interaction in II-VI quantum dots and wells. *Phys. Status Solidi (a)*, **164**:505, 1997.

[58] J. Puls, M. Rabe, H.-J. Wünsche, and F. Henneberger. Magneto-optical study of the exciton fine structure in self-assembled CdSe quantum dots. *Phys. Rev. B*, **60**:16303, 1999.

[59] M. Rabe, M. Lowisch, and F. Henneberger. Self-assembled cdse quantum dots formation by thermally activated surface reorganization. *J. Cryst. Growth*, **184/185**:248, 1998.

[60] N. Peranio, A. Rosenauer, D. Gerthsen, S. V. Sorokin, I. V. Sedova, and S. V. Ivanov. Structural and chemical analysis of CdSe/ZnSe nanostructures by transmission electron microscopy. *Phys. Rev. B*, **61**:16015, 2000.

[61] D. Litvinov, A. Rosenauer, D. Gerthsen, and N. N. Ledensov. Character of the Cd distribution in ultrathin CdSe layers in a ZnSe matrix. *Phys. Rev. B*, **61**:16819, 2000.

[62] A. Rosenauer and D. Gerthsen. Composition evaluation by the lattice fringe analysis method using defocus series. *Ultramicroscopy*, **76**:49, 1999.

[63] T. Yao. characterization of ZnSe grown by molecular beam epitaxy. *J. Cryst. Growth*, **72**:31, 1985.

[64] M. Lowisch. *Exzitonen in (Zn,Cd)Se und CdSe Quantenstrukturen - Vom Lokalisationsplatz zum Quantenpunkt.* PhD thesis, Institut für Physik, Humboldt-Universität zu Berlin, 1998.

[65] T. Flissikowski. Exziton-dynamik in selbstorganisierten CdSe-quantenpunkten. Master's thesis, Institut für Physik, Humboldt-Universität zu Berlin, 1998.

[66] N. F. Scherer, A. J. Ruggiero, M. Du, and G. R. Fleming. Time resolved dynamics of isolated molecular systems studied with phase-locked femtosecond pulse pairs. *J. Chem. Phys.*, **93**:856, 1990.

[67] N. F. Scherer, R. J. Carlson, A. Matro, M. Du, A. J. Ruggiero, V. Romero-Rochin, J. A. Cina, G. R. Fleming, and S. A. Rice. Fluorescence-detected wave packet interfrometry: Time resolved molecular spectroscopy with sequences of femtosecond phase-locked pulses. *J. Chem. Phys.*, **95**:1487, 1991.

[68] J. T. Fourkas, W. L. Wilson, G. Wäckerle, A. E. Frost, and M. D. Fayer. Picosecond time-scale phase-related optical pulses: measurement of sodium optical coherence decay by observation of incoherent fluorescence. *J. Opt. Soc. Am. B*, **6**:1905, 1989.

[69] I. A. Akimov. private communication.

[70] M. Lowische, M. Rabe, F. Kreller, and F. Henneberger. Electronic excitations and longitudinal optical phonon modes of self-assembled CdSe quantum dots revealed by microprobe studies. *Appl. Phys. Lett.*, **74**:2489, 1999.

[71] M. Nirmal, B. O. Dabbousi, M. G. Bawendi, J. J. Macklin, J. K. Trautman, T. D. Harris, and L. E. Brus. Fluorescence intermittency in single cadmium selenide nanocrystals. *Nature (London)*, **383**:802, 1996.

[72] U. Banin, M. Bruchez, A. O. Alivisatros, T. Ha, S. Weiss, and D. S. Chemla. Evidence for a thermal contribution to emission intermittency in single CdSe/CdS core/shell nanocrystals. *J. Chem. Phys.*, **110**:1195, 1999.

[73] M. Kuno, D. P. Fromm, H. F. Hamann, A. Gallagher, and D. J. Nesbitt. Nonexponential 'blinking' kinetics of single cdse quantum dots: A universal power law behavior. *J. Chem. Phys.*, **112**:3117, 2000.

[74] H. W. van Kesteren, E. C. Cosman, W. A. J. A. van der Poel, and C. T. Foxon. Fine structure of excitons in type-II GaAs/AlAs quantum wells. *Phys. Rev. B*, **41**:5283, 1990.

[75] S. Farfad, R. Leon, D. Leonard, J. L. Merz, and P. M. Petroff. Phonons and radiative recombination in self-assembled quantum dots. *Phys. Rev. B*, **52**:5752, 1995.

[76] R. Heitz et al. Multiphonon-relaxation processes in self-organized InAs/GaAs quantum dots. *Appl. Phys. Lett.*, **68**:361, 1996.

[77] P. Meystre and M. Sarget III. *Elements of Quantum Optics.* Springer, Berlin, 1998.

[78] S. Bar-Ad and I. Bar-Joseph. Exciton spin dynamics in GaAs heterostructures. *Phys. Rev. Lett.*, **68**:349, 1992.

[79] K. Bluhm. *Density Matrix Theory and Application.* Plenum, New York, 1981.

[80] X.-Q. Li, H. Nakayama, and Y. Arakawa. Phonon bottelneck in quantum dots: Role of lifetime of the confined optical phonons. *Phys. Rev. B*, **59**:5069, 1999.

[81] M.U. Wehner, M.H. Ulm, D.S. Chemla, and M. Wegener. Coherent control of electron-LO-phonon scattering in bulk GaAs. *Phys. Rev. Lett.*, **80**:1992, 1998.

[82] R.I. Dzhioev, B.P. Zakharchenya, V.L. Korenev, P.E. Pak, D.A. Vinokurov, O.V. Kovalenko, and I.S. Tarasov. Optical orientation of donor-bound excitons in nanosized InP/InGaP islands. *Phys. Solid State*, **40**:1587, 1998.

[83] I.V. Ignatiev, I.Ya. Gerlovin, S.Yu. Verbin, I.A. Yigova, and Y. Masumoto. Long-lived spin polarisation in the charged InP quantum dots. *Physica E (Amsterdam)*, **17**:361, 2003.

[84] Ph. Roussignol, P. Rolland, R. Ferreira, C. Delalande, G. Bastard, A. Vinattieri, J. Martinez-Pastor, L. Carraresi, M. Colocci, J. F. Palmier, and B. Etienne. Hole polarization and slow hole-spin relaxation in an n-doped quantum-well structure. *Phys. Rev. B*, **46**:7292, 1992.

[85] L. M. Woods, T. L. Reinecke, and R. Kotlyar. hole spin relaxation in quantum dots. *Phys. Rev. B*, **69**:125330, 2004.

[86] A. Khaetskii, D. Loss, and L. Glazman. Electron spin evolution induced by interaction with nuclei in a quantum dot. *Phys. Rev. B*, **67**:195329, 2003.

[87] E. I. Gryncharova and V. I. Perel'. Relaxation of nuclear spins interacting with holes in semiconductors. *Fiz. Tekhn. Poluprovodn.*, **11**:1697, 1977.

[88] V. Blanchet, C. Nicole, B. Mohamed-Aziz, and B. Girard. Temporal coherent control in two-photon transitions: From optical interferences to quantum interferences. *Phys. Rev. Lett.*, **78**:2716, 1997.

[89] K. Brunner, G. Abstreiter, G. Böhm, G. Tränkle, and G. Weimann. Sharp-line photoluminescence and two-photon absorption of zero-dimensional biexcitons in a GaAs/AlGaAs structure. *Phys. Rev. Lett.*, **73**:1138, 1994.

[90] B. Cagnac, G. Grynberg, and F. Biraben. Multiphoton absorption spectroscopy without doppler broadening. *Journal de Physique (Paris)*, **34**:845, 1973.

[91] G. W. Wen, J. Y. Lin, H. X. Jiang, and Z. Chen. Quantum-confined stark effects in semiconductor quantum dots. *Phys. Rev. B*, **52**:5913, 1995.

[92] J. Seuffert, R. Weigand, G. Bacher, T. Kümmell, A. Forchel, K. Leonardi, and D. Hommel. Spectral diffusion of the exciton transition in a single self-organized quantum dot. *Appl. Phys. Lett.*, **76**:1872, 2000.

[93] V. Türck, S. Rodt, O. Stier, R. Heitz, R. Engelhardt, U. W. Pohl, D Bimberg, and R. Steingrüber. Effect of random field fluctuations on excitonic transitions of individual CdSe quantum dots. *Phys. Rev. B*, **61**:9944, 2000.

[94] L. Marsal, L. Besombes, F. Tinjod, K. Kheng, A. Wasiela, B. Gilles, J.-L. Rouviére, and H. Mariette. Zero-dimensional excitons in CdTe/ZnTe nanostructures. *J. Appl. Phys.*, **91**:4936, 2002.

[95] B. Patton, W. Langbein, and U. Woggon. Trion, biexciton, and exciton dynamics in single self-assembled CdSe quantum dots. *Phys. Rev. B*, **68**:125316, 2003.

[96] L. Besombes, K. Kheng, L. Marsal, and H. Mariette. Few-particle effects in single CdTe quantum dots. *Phys. Rev. B*, **65**:121314, 2002.

[97] W. Langbein, J. M. Hvam, M. Umlauff, H. Kalt, B. Jobst, and D. Hommel. Binding-energy distribution and dephasing of localized biexcitons. *Phys. Rev. B*, **55**:R7383, 1997.

[98] H. Nickolaus and F. Henneberger. Biexciton four-wave-mixing signal in quantum wells: Photon-echo versus free-induction decay. *Phys. Rev. B*, **57**:8774, 1998.

[99] G. Bacher, R. Weigand, J. Seufert, V. D. Kulakovskii, N. A. Gippius, and A. Forchel. Biexciton versus exciton lifetime in a single semiconductor quantum dot. *Phys. Rev. Lett.*, **83**:4417, 1999.

[100] P. Borri, W. Langbein, S. Schneider, U. Woggon, R. L. Sellin, D. Ouyang, and D. Bimberg. Relaxation and dephasing of multiexcitons in semiconductor quantum dots. *Phys. Rev. Lett.*, **89**:187401, 2002.

Acknowledgement

The research work described in this thesis was carried out at the institute of physics at the Humboldt university of Berlin in the group 'Grundlagen der Photonik'. I wish to thank Prof. Henneberger who allowed me to work in his group and give me this very interesting and promising task. Without his help the interpretation of the results and the models used in this work will not exist as written in this thesis.

I am deeply indebted to Dr. Ilya A. Akimov for his excellent supervising, the innumerable fruitful discussions where several ideas and solutions are worked out, the friendly working atmosphere, and the careful reading of the manuscript. Many thanks also to Andreas Hundt for the introduction and help concerning magnetic field dependent measurements and for placing several PLE spectra and magnetic field data disposal, making the selection of suitable QDs for the various experiments possible.

I am grateful to Dr. M. Lowisch who introduced me in the world of single dot spectroscopy and helped me to achieve a good starting point for time domain measurements on single quantum dots.

I am indebted to Dr. J Puls for stimulating and critical discussions concerning physical and technical questions. Many thanks to Dr. I. Dudeck for support in at electronic problems.

I am enjoy if I think on the long measuring nights, in which I measured with Alexander Betke most of the coherent control data. Thanks a lot for this.

Many thanks also to Dr. P. Kratzert and Dr. M. Rabe for the fabrication of the high quality QD samples and its characterization in the AFM.

I am grateful to Dr. S. Rogaschewski for structuring the used samples and its characterization in the SEM.

I want to express my gratitude to the current and former group members especially S. Blumstengel, G. Chusainow, G. Rohde, Dr. B. Rau and S. Schwertfeger for the nice working atmosphere.

Publications

Most of this work is already published in the following articles:

- *Photon Beats from a Single Semiconductor Quantum Dot*,
  T. Flissikowski, A. Hundt, M. Lowisch, M. Rabe, and F. Henneberger,
  Phys. Rev. Lett. **86**, 3172 (2001).

- *Single hole spin relaxation in a quantum dot*,
  T. Flissikowski, I. A. Akimov, A. Hundt, and F. Henneberger,
  Phys. Rev. B **68**, 161309(R) (2003).

- *Two-Photon Coherent Control of a Single Quantum Dot*,
  T. Flissikowski, A. Betke, I. A. Akimov, and F. Henneberger,
  Phys. Rev. Lett. **92**, 227401 (2004).

- *Excitation Spectrum, Relaxation and Coherence of Single self-Assembled CdSe Quantum Dots*,
  A. Hundt, T. Flissikowski, M. Lowisch, M. Rabe, and F. Henneberger,
  Phys. Stat. Sol. (b) **224**, 159-163 (2001).

- *Fine structure of the trion triplet state in a single self-assembled semiconductor quantum dot*,
  I. A. Akimov, A. Hundt, T. Flissikowski, and F. Henneberger,
  Appl. Phys. Lett. **81**, 4730 (2002).

- *Energy spectrum of negatively charged single quantum dot: trion and charged biexciton states*,
  I. A. Akimov, A. Hundt, T. Flissikowski, P. Kratzert, and F. Henneberger,
  Physica E **17**, 31-34 (2003).

- *Spin processes related to trions in quantum dots*,
  I. A. Akimov, T. Flissikowski, A. Hundt, and F. Henneberger,
  Phys. Stat. Sol. (a) **201**, 412-420 (2003).

Lebenslauf

Name:	Timur	Flissikowski
Geburtsdatum:	13.08.1972	
Geburtsort:	Berlin	
Familienstand:	ledig, kinderlos	
Schulbildung:	1989	Abschluß der 10-klassigen polytechnischen Oberschule mit ’ausgezeichnet’
	1992	Abschluß einer Berufsausbildung mit Abitur (allg. Hochschulreife), Elektromonteur
Studium:	1992	Beginn eines Physikstudiums an der Humboldt-Universität zu Berlin
	1995	Vordiplom in Physik mit ’gut’
		Studienabschluß mit der Gesamtnote ’gut’
Praktika/ Diplomarbeit:	1993	’Untersuchungen zur Entwicklung einer ortsauflösenden Detektoranordnung’ bei Herrn Dr. H. Kerkow im Elektronenbeschleuniger Labor der HU-Berlin
	1996	Aufbau und Medienuntersuchungen für ein Weißlichterzeugungsmodul in einem fs-Laser bei Herrn Dr. H. Redlin an der HU-Berlin.
	1997	Beginn der Diplomarbeit zum Thema: ’Exzitonendynamik in Halbleiter-Quantenstrukturen nach optischer Anregung.’
	1999	Abschluß der Diplomarbeit, Note: 1.3
Berufspraxis:	2/1999-12/2003	Wissenschaftlicher Mitarbeiter im Institut für Physik der Humboldt-Universität zu Berlin, Arbeitsgruppe Prof. Henneberger

Selbstständigkeitserklärung

Hiermit erkläre ich, die vorliegende Arbeit selbstständig ohne fremde Hilfe verfasst zu haben und nur die angegebene Literatur und Hilfsmittel verwendet zu haben.

Ich habe mich anderwärts nicht um einen Doktorgrad beworben und besitze einen entsprechenden Doktorgrad nicht.

Ich erkläre die Kenntnisnahme der dem Verfahren zugrunde liegenden Promotionsordnung der Mathematisch-Naturwissenschaftlichen Fakultät I der Humboldt-Universität zu Berlin.

14. Mai 2004 Timur Flissikowski

Gutachtervorschlag:

1. Herr Professor Dr. Fritz Henneberger, Humboldt-Universität zu Berlin
2. Herr Professor Dr. Oliver Benson, Humboldt-Universität zu Berlin
3. Herr Priv.-Doz. Dr. A. Hoffmann,
   Institut für Festkörperphysik
   Technische Universität Berlin
   Hardenbergstrasse 36
   10623 Berlin